Title

Rational Design of Transition Metal-Nitrogen-Carbon Electrocatalysts for Oxygen Reduction Reaction

Author

Liu, Zhuang

Publication Date

2018

UNIVERSITY OF CALIFORNIA

Los Angeles

Rational Design of Transition Metal-Nitrogen-Carbon Electrocatalysts for Oxygen Reduction Reaction

A dissertation submitted in partial satisfaction of the
requirements for the degree Doctor of Philosophy
in Chemical Engineering

by

Zhuang Liu

2018

ABSTRACT OF THE DISSERTATION

Rational Design of Transition Metal-Nitrogen-Carbon Electrocatalysts for Oxygen Reduction Reaction

by

Zhuang Liu

Doctor of Philosophy in Chemical Engineering

University of California, Los Angeles, 2018

Professor Yunfeng Lu, Chair

The harvest and conversion of energy is of crucial importance for human civilization. Today, the fast growth in energy consumption, together with the environmental problems caused by fossil fuel usage, calls for renewable and clean energy supply, such as solar, wind, geothermal, and tidal energy. However, such energies are not consistent in both time and location, bringing energy storage on request. Intensive research has been focused on the development of electrochemical energy storage (EES) devices.

Among these EES devices, hydrogen fuel cells and metal-air batteries have attracted the special attention because of their high theoretical energy densities. Yet, one major issue lies in the sluggish oxygen reduction reaction (ORR) that takes place at the cathodes. For example, the theoretical voltage of a hydrogen-oxygen fuel cell is 1.23 V (standard condition). However, the voltage output obtained under a meaningful current density is only about 0.7 V, where the voltage loss is primarily caused by the overpotential in the cathodes. Developing efficient electro-catalysts, which can lower the overpotential of ORR, is indispensable for achieving high performance devices.

The state-of-the-art ORR electro-catalysts are generally based on platinum, which is limited by cost and scarcity. Developing electro-catalysts based on earth abundant metal elements is critical for large-scale application of fuel cells and metal-air batteries. Among the non-precious-metal catalysts (NPMCs) explored in recent decades, pyrolyzed iron-nitrogen-carbon (Fe-N-C) catalysts is widely regarded as the most promising candidate for replacing platinum due to their high activity. However, the traditional method for preparing Fe-N-C catalysts involves high-temperature pyrolysis of the precursors, which is a highly complex and unpredictable process. As-prepared Fe-N-C catalysts usually contain mixed chemical phases (e.g., Fe-based nanoparticles, Fe-N coordination site and various nitrogen species), as well as carbon scaffolds with random morphology. Such complexity makes it difficult to identify the active site and control the porous structure. Though progress has been made in improving their performance through delicate selection of precursors, such process is largely based on test-and-trial method, shedding little light

on the understanding of the material.

In this dissertation, we designed a novel "post iron decoration" synthetic strategy towards efficient Fe-N-C catalysts, which de-convolutes the growth of iron and nitrogen species, enables the rational design of the catalyst structure, and provides a series of effective model materials for active site probing. Specifically, liquid iron penta-carbonyl was used to wet the surface of mesoporous N-doped carbon spheres (NMC), whose porous structure is determined by the template used for preparation. The obtained $Fe(CO)_5$/NMC complex was then pyrolyzed to generate the Fe/NMC catalysts. Through comparative study and thorough material characterization, we demonstrated that the pyridinic-N of NMC anchors the Fe atoms to form Fe-N_x active sites during pyrolysis, while the graphitic-N remains ORR active. The excessive Fe atoms were aggregated forming fine nanoparticles, which were subsequently oxidized forming amorphous-iron oxide/iron crystal core-shell structure. All the composing elements of Fe/NMC catalysts are uniformly distributed on the NMC scaffold, whose porous structure is shown to be not affected by Fe decoration, guaranteeing the effective exposure of active sites. The best performing Fe/NMC catalysts exhibited a high half-wave potential of 0.862 V, which is close to that of the benchmark 40% Pt/C catalyst. Such high activity is primarily attributed to the Fe-N_x active sites in the catalysts. While the surface oxidized Fe crystallites though not being the major active site, is revealed to catalyze the reduction of HO_2^-, the 2e ORR product, facilitating the 4e reduction of oxygen. Finally, such synthetic strategy is successfully extended to prepare other Me-N-C materials.

Based on the established understanding of the active sites, we then complexed the active $Fe(CO)_5$ molecules with a N-rich metal-organic framework (ZIF-8) to form a precursor, which was subsequently pyrolyzed to form Fe-NC catalysts. During the pyrolysis, $Fe(CO)_5$ reacts homogeneously with the ZIF-8 scaffold, leading to the formation of uniform distribution of Fe-related active sites on the N-rich porous carbon derived from ZIF-8. The zinc atoms in the crystalline structure of ZIF-8 serves as thermo-sacrificial template, resulting in the formation of hierarchical pores that provide abundant easily accessible ORR active sites. In virtue of these advantageous features, the best performing Fe-NC catalyst exhibited a high half-wave potential of 0.91 V in rotating disk electrode experiment in 0.1 M NaOH. Furthermore, zinc-air battery constructed with Fe-NC-900-M as the cathode catalyst exhibited high open-circuit voltage (1.5 V) and a peak power density of 271 mW cm^{-2}, which outperforms those made with 40% Pt/C catalyst (1.48 V, 1.19 V and 242 mW cm^{-2}), and most noble-metal free ORR catalysts reported so far. Finally, such a synthetic method is economic and easily-scalable, offering possibility for further activity and durability improvement.

The dissertation of Zhuang Liu is approved.

Dante A Simonetti,

Samanvaya Srivastava,

Qibing Pei,

Yunfeng Lu, Committee Chair

University of California, Los Angeles

2018

To the future of myself

Table of Contents

LIST OF FIGURES

LIST OF TABLES

ACKNOWLEDGEMENTS

I have always enjoyed natural science subjects, and I have always wanted to pursue a PhD and become a scientist since elementary school. My journey at UCLA really transformed me from a student in the classroom to a researcher, and I am indebted to many people for their support throughout my PhD study.

Firstly, I would like to express my deepest appreciation to my principle advisor, Professor Yunfeng Lu. This Ph.D dissertation would not have been possible without his guidance. Of the many lessons I learned from Dr. Lu, two are the most important ones. The first one is realizing the difference and correlation between studying and research. Books and papers are written by others years ago, yet research is about doing something new, that no one has tried before. Nonetheless, you'll first need to be a good student in studying others' ideas to be able to come up with creative and meaningful new proposals. Though this may sound trivial, it is indeed the first important realization for a beginner in graduate study. The second one is realizing how interest, is of fundamental importance for one's research and academic career. I watched how Dr. Lu's strong interest in battery technology motivated his enthusiastic studying of related knowledges and relentless trying of new ideas for decades, and how his belief in doing research that is close to application kept him active in both academia and industry efforts even though it makes him work extra hard years after years. To sum up, I think two things are needed for doing great research, which are critical thinking and passion for the subject. I am indebted to Dr. Lu for all those great opportunities learning from him both at school, and the dinner table in his house.

I would also thank my doctoral committee members, Dr. Robert F. Hicks, Dr. Selim Senkan, Dr. Qibing Pei, Dr. Dante Simonetti and Dr. Samanvaya Srivastava for their support of my doctoral candidacy. Their enlightening suggestions helped me realize the benefit of thinking about one subject from different perspectives, their insightful questions helped shaping the frame of my PhD research, and their instructions in speech helped improving my presenting skills.

I would also like to express my sincerest appreciation and gratefulness for Professor Stuart Brown and Professor Yiqin Gao (Peking University), who are the two most charming instructors with high characters I've ever had, and helped me patiently and selflessly when I'm in need. They inspired me with their enlightening lectures, light up my world with their care and gave me a lot of good time thinking and discussing. They make me want to become a scientist even more. I'm also grateful to Professor Lin Gu (Institute of Physics, Chinese Academy of Sciences), who helped me with the experiments for my first publication at UCLA, and who has been advising me like a loving big brother.

I would like to thank my undergraduate advisor, Professor Jinghong Li, and Dr. Yongmin Wu, who instructed me in my first research project. My undergraduate research experience was very helpful as a training of experimental skills and critical thinking, which also influenced my PhD journey. I also greatly appreciate the help from Jing Fang, Youzhen Dong, Mengjia Liu and all the other members of Professor Li's group for their help with my experiments. Wish you all the best.

To my dear Lu group members and other friends at UCLA, who I have spent the longest time with, during my four years of graduate study. You are like a family, and I would run out of words to thank you all. I would like to thank Dr. Zaiyuan Le, who has dedicated lots of time teaching and helping me in all aspects of life here. Your character and decency really made my time at UCLA much more enjoyable than it would have been without you, and I wish you would find your ideal job soon. I would also thank Dr. Haobin Wu, who helped me a lot with my research, especially when I first started my own project. More importantly, Dr. Wu made the group much better with his helping nature, and I wish him all the success in his future career as a professor. I also thank Dr. Jing Liu and Dr. Gen Chen, for all your good discussion and instructions, wish you all the best in your future career. To Dr. Zipeng Zhao, to whom I owe half my experimental skills to. You are probably the kindest person I have ever met, and my appreciation for you cannot be expressed by mere words. Wish you accomplish your dreams young. To Xianyang Li, Xinru Li, Ximin Chen, Xiaoqiong Bai, Wendi Li, Ziyi Li. Though some of you were only together with me at UCLA for 1.5 years, I had the most fun together with you. Thank you for all those priceless memories, wish you all the best in the future. I also want to thank Dr. Huihui Zhou, Dr. Xiaoyan Liu, Dr. Xu Wu, Dr. Fei Sun, Dr. Jie Li, Dr. Yang Liu, Dr. Ruguang Ma, Gurong Shen, Xing Lu, Li Shen, Jie Ren, Dejia Kong, Kang Peng, Di Wu, Ming Zhao, Luke Minardi, John Billingsley, Xiang Xu, Mufan Li and etc. Thank you for all the good time in lab, office, classrooms and sports fields.

Besides, people, I also enjoyed the beautiful campus of UCLA, where I strolled for hundreds of times. Thank you, UCLA campus.

I am indebted to my parents, who has always tried providing me with the best they can offer.

I am lucky and proud being the son of two intelligent, diligent, and virtuous scholars, my parents, who made it possible for me to live up to my dreams. I will pass on the standards and honor, and I will not let you down. I am also indebted to my family. To my late beloved grandparents watching me from above, I will also carry your love with me, and I will make you proud.

This is an ending and beginning at the same time, I’ll learn from the past, and best wishes for the future!

VITA

2010 - 2014	B.S., College of Chemistry and Molecular Engineering Peking University, China
2014 – 2018	Teaching Assistant, Graduate Researcher Department of Chemical and Biomolecular Engineering University of California, Los Angeles, USA
2016 – 2017	Graduate Division Award Department of Chemical and Biomolecular Engineering University of California, Los Angeles, USA
2016 – 2017	Member Materials Research Society

Publications

1. **Z. Liu**, F. Sun, L. Gu, G. Chen, T. Shang, J. Liu, Z. Le, X. Li, H. B. Wu, Y. Lu, Post Iron-Decoration of Mesoporous Nitrogen-Doped Carbon Spheres for Efficient Electrochemical Oxygen Reduction. ***Advanced Energy Materials,*** 2017, 7, 1701154. https://doi.org/10.1002/aenm.201701154
2. **Z. Liu**, Y. Wu, J. Li, One-Step Synthesis of MnO_2 Flower/Carbon Nanotube with Improved Lithium Storage Properties. ***Journal of Nanoscience and Nanotechnology***, Volume 15, Number 4, April 2015, pp. 2896-2901
3. Z. Wen, W. Wu, **Z. Liu**, H. Zhang, J Li, J. Chen, Ultrahigh-Efficiency Photocatalysts Based on Mesoporous Pt–WO_3 Nano-Hybrids. ***Phys. Chem. Chem. Phys.***, 2013, 15, 6773-6778
4. W. Wei, Z. Wang, **Z. Liu**, Y. Liu, L. He, D. Chen, A. Umar, L. Guo, J. Li, Metal Oxide Hollow Nanostructures: Fabrication and Li Storage Performance. ***Journal of Power Sources***, 2013, 238, 376-387

Chapter 1. Introduction

1.1 Background & Physics and Chemistry of Oxygen Reduction Reaction (ORR)

The harvest and conversion of energy constitutes a very important part of human civilization. However, the huge and fast growing world energy demand faces us with the depletion of fossil fuels in the near future, which is the major (80%) energy source of today's society. Such energy crisis, together with the many urgent environmental problems caused by fossil fuel use, has forced the seeking of renewable and clean energy supply. Solar and wind energy appears to be promising alternatives available, as they are both sustainable and environment-friendly. However these renewable energies (also geothermal, wave and tidal, and biomass energies) are not consistent in both time and location, requesting energy storage and subsequent conversion.[1-5] Therefore, as electricity is the main form of energy consumption in modern society, intensive research has been focused on the development of electrochemical energy storage (EES) devices worldwide.[6] Of the many EES devices, lithium-ion battery (LIB) is probably the most important one and has served effectively as the primary power source for many portable electronic products that is seen everywhere in our daily life. However, the ever growing demand for EES technologies for emerging electronic devices and especially electric vehicles requires continuously the improvement of the energy and power density of the energy source. Whereas the performance of LIB is already approaching its limit and consequently no dramatic improvement of its performance is expected in the future. Thus, new EES devices based on new chemistry is being actively investigated with a target energy density of 500 Wh/kg at a price < $100/kWh.[7]

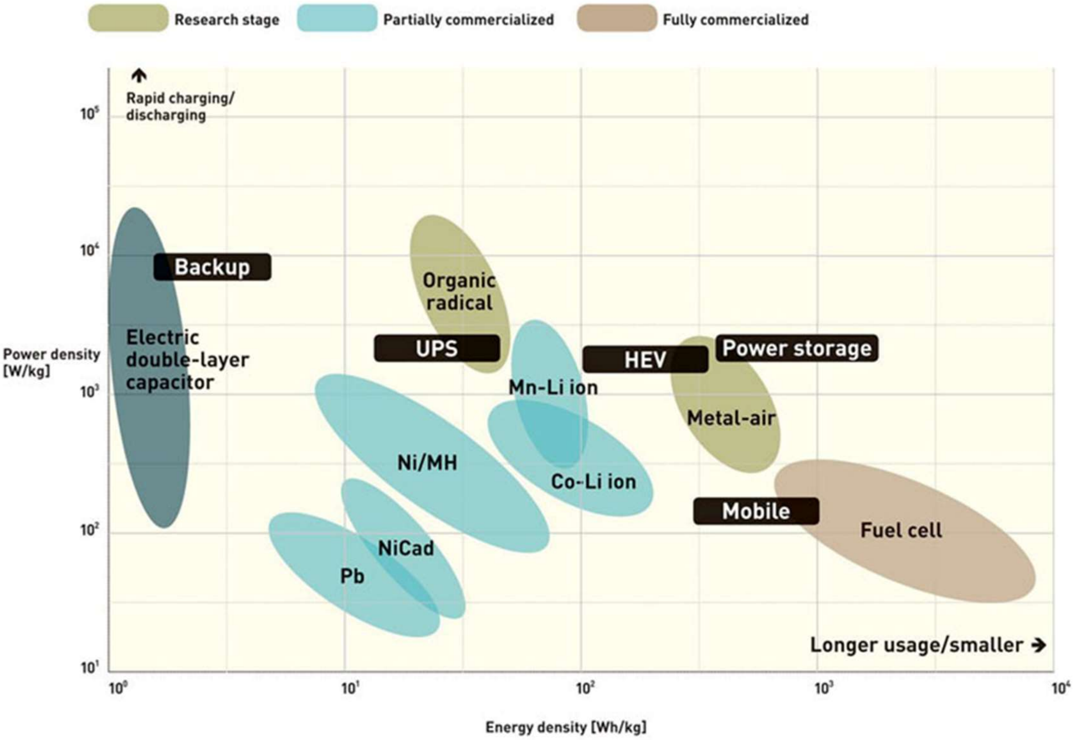

Figure 1.1 Ragone plot comparing the performance of various EES devices (energy density vs. power density).[8]

Power density and energy density are the most important metric for evaluating the performance of EES devices. The characteristic power and energy densities of various EES devices are summarized and compared in the Ragone plot (**Figure 1.1**). Consequently, fuel cells and metal-air batteries have attracted the special interest of researchers among the potential candidate EES devices, because of their high theoretical power and energy densities. Besides the electrochemical performance, hydrogen fuel cells and metal-air batteries also have the advantage of being environment-friendly as their only byproduct are heat and water. Which makes them the most promising and attractive technologies for future energy supply.[9]

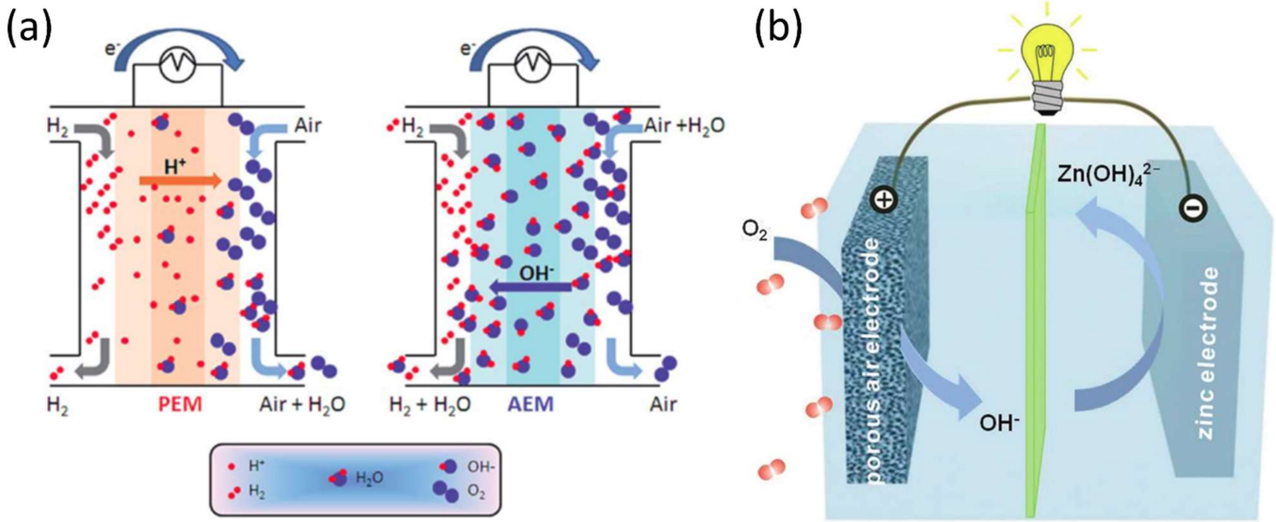

Figure 1.2 (a) Schematic illustration of acid hydrogen fuel cell (left) and alkaline hydrogen fuel cell (right). (b) Schematic illustration of zinc-air battery.[10, 11]

The schematic illustration of hydrogen fuel cell and zinc-air battery operation are shown in **Figure 1.2**. The chemical reactions that happen at the cathode and anode of these EES devices are listed from **equation (1) to (9)**, where their corresponding potentials are included. As demonstrated in **Figure 1.2**, hydrogen fuel cells can be divided into two types depending on the electrolyte it uses (acidic or alkaline). Though electrode reactions can be different under the two conditions, the overall reaction of the cells are the same (**equation 5**), generating an open circuit voltage of 1.23 V under standard conditions according to thermodynamic calculations. The zinc air battery, which runs only with alkaline electrolyte on the other hand, has a higher open circuit voltage of 1.65 V under standard conditions according to thermodynamic calculations (**equation 9**). The higher theoretical voltage of zinc-air battery endows it with higher power density than hydrogen fuel cells, yet less energy density, because zinc is much heavier than hydrogen per electron transferred.

$$2H_2 \longrightarrow 4H^+ + 4e \qquad E = 0.00\ \text{V vs. SHE} \tag{1}$$

$$O_2 + 4H^+ + 4e \longrightarrow 2H_2O \qquad E = 1.23\ \text{V vs. SHE} \tag{2}$$

$$2H_2 + 4OH^- \longrightarrow 4H_2O + 4e \qquad E = -\ 0.828\ \text{V vs. SHE} \tag{3}$$

$$O_2 + 2H_2O + 4e^- \longrightarrow 4OH^- \qquad E = 0.401\ \text{V vs. SHE} \tag{4}$$

$$2H_2 + O_2 \longrightarrow 2H_2O \qquad E\ \text{cell} = 1.23\ \text{V (both acid and alkali)} \tag{5}$$

$$Zn + 4OH^- \longrightarrow Zn(OH)_4^{2-} + 2e \qquad E = -1.25\ \text{V vs. SHE} \tag{6}$$

$$Zn(OH)_4^{2-} \longrightarrow ZnO + H_2O + 2OH^- \tag{7}$$

$$\tfrac{1}{2}\, O_2 + H_2O + 2e \longrightarrow 2OH^- \qquad E = 0.4\ \text{V vs. SHE} \tag{8}$$

$$Zn + \tfrac{1}{2}O_2 \longrightarrow ZnO \qquad E\ \text{cell} = 1.65\ \text{V} \tag{9}$$

However, the theoretically calculated output voltage of these devices are compromised during practical application. In practice, the typical working voltage of zinc-air battery is lower than 1.2 V, and that of hydrogen fuel cell is under than 0.7 V at meaningful discharge current densities. Such voltage loss includes contribution from kinetic losses, ohmic losses and mass transfer losses at the same time. Yet, the dominant part of it comes from the over-potential of the air cathode, owing to the sluggish kinetics of the oxygen reduction reaction (ORR) that happens there.[9, 11] Thus, ORR catalyst at the air cathode are indispensable in both hydrogen fuel cells and zinc-air batteries, in order to have them operate at meaningful voltage and current densities.

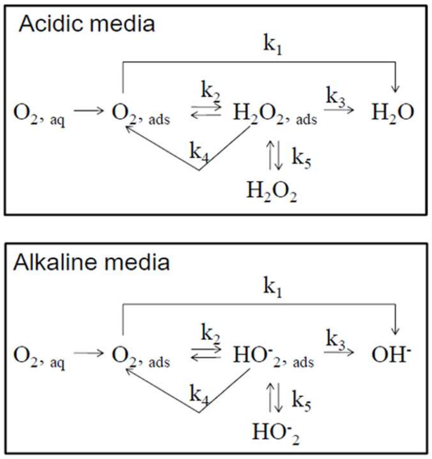

Electrolyte	Reaction pathway	Reaction potential [V] vs. NHE
alkaline	*4e pathway:*	
	$O_2 + 2H_2O + 4e^- \rightarrow 4OH^-$	+0.401
	[2+2] e⁻ pathway:	
	$O_2 + H_2O + 2e^- \rightarrow HO_2^- + OH^-$	−0.065
	$HO_2^- + H_2O + 2e^- \rightarrow 3OH^-$	+0.867
acidic	*4e pathway:*	
	$O_2 + 4H^+ + 4e^- \rightarrow 2H_2O$	+1.229
	[2+2]e pathway:	
	$O_2 + 2H^+ + 2e^- \rightarrow H_2O_2$	+0.70
	$H_2O_2 + 2H^+ + 2e^- \rightarrow 2H_2O$	+1.76

Figure 1.3 Summary of possible ORR reaction routes in acidic and alkaline media (left), and the standard reaction potential of the corresponding reactions involved in different reaction pathways (right).[12]

Basically, the oxygen reduction reaction we are focusing on, is an electrochemical process, in which four or two electrons are passed from the electrode to a dioxygen molecule. The oxygen molecule is reduced it into various products, depending on the electrolyte used, and the specific reaction route it follows.

Figure 1.3 shows a summary of the possible reaction routes of ORR, and the specific reaction formula involved in both acidic and alkaline media. As can be seen, there are mainly two types of reaction pathways, which are the 2 e pathway and the 4 e pathway, differentiated by the number of electrons transferred per oxygen molecule and the final products. Specifically, after the adsorption of oxygen molecule onto the surface of the electrode (the first step of the catalytic process), there are four routes the reaction can follow. 1. Four electrons are inserted into an oxygen molecule, forming two water molecules in acidic media or four hydroxide ions in alkaline media directly (k_1) without any intermediate products. Which is called a direct 4e pathway. 2. The adsorbed oxygen molecule takes only two electrons at first, turning into adsorbed peroxide species, and then the peroxide species accept another two electrons (k_2, k_3), forming the same final products as in the former pathway. Which is called a serial 2+2 e pathway. 3. The adsorbed peroxide species, either decompose, forming a new oxygen molecule that goes back into the reduction cycle (k_4), or desorb from the electrode surface and go into the bulk electrolyte (k_5). Both of which can be considered a 2e pathway. Thus, to achieve a fuel cell or zinc-air battery with high power and energy density, the direct 4e pathway which has the fastest kinetics, is obviously the most favorable route for ORR.[12]

In spite that the oxygen reduction reaction follows similar reaction routes in alkaline and acid electrolyte, it’s long been noticed that it is much easier for an electro-catalyst to achieve high performance in alkaline media than in acidic media. And besides the fact that it’s generally harder for catalysts to be stable in acid electrolyte, previous work also tried to articulate this phenomenon (the so called pH effect) from the perspective of fundamental reaction mechanism. It is typically assumed that, the first step, also the rate determining step in the oxygen reduction reaction is the insertion of one electron into the oxygen molecule, forming superoxide radical anion ($O_2^{\bullet -}$), either via inner-sphere electron transfer mechanism or outer-sphere electron transfer mechanism. And since only O_2 and electron are involved in the process, the standard potential of this redox couple ($O_2/O_2^{\bullet -}$) is pH independent, being E° = -0.3 + 0.03 V vs. SHE. However, as shown in equation (2) and (4), the standard reduction potential of oxygen drops from 1.23 V to 0.401 V, when the pH of the electrolyte changes from zero to fourteen. And consequently, the over potential of the first step of electron transfer decreases from 1.53 V at a pH value of zero, to 0.7 V when pH is equal to fourteen. Which indicates that it is much easier for this rate determining step of first electron transfer to happen in alkaline media than in acidic media, regardless of the other factors affecting the ORR, making an outer sphere model for ORR possible.[13-15] While, the above argument primarily offers a thermodynamic reason for the pH effect, on the other hand, kinetic reasons could also play an important role in causing the observed pH effect. Since the ORR performance varies a lot on different catalysts' surfaces, it's obvious that the inner-sphere electron transfer mechanism is dominant in this heterogeneous catalytic oxygen reduction reaction. And the adsorption of oxygen molecule onto the catalyst's surface, being the first step of the heterogeneous inner-sphere reaction (which is often termed electro-catalytic reaction), is of great importance for the overall performance of the catalysts. As there is a competition for the catalysts' surface sites between O_2 and the anions in the electrolyte, and the adsorption energy of the inions on the electrode surface is decreased when pH increases, owing to the accompanying negative shift of the reduction potential of oxygen, it is kinetically easier for ORR to proceed in alkaline electrolyte. Moreover, the simple fact that the stable intermediate hydrogen peroxide doesn't adsorb on active site is actually one fundamental problem for all kinds of catalysts in acidic media. For hydrogen peroxide has a closed shell electronic structure, and unlike its counterpart hydrogen peroxide anion in alkaline media, it possesses no net charges, which means that there is no motive force for it to adsorb on the active site. Also considering that it's a stable molecule itself, it will just desorb into the bulk electrolyte, terminating the ORR after only transferring 2 electrons. Rendering the catalyst ineffective.

1.2 State of Art ORR Electrocatalysts and Challenges

Although the specific reaction routes that the oxygen reduction reaction follows varies depending on the catalysts and electrolyte used, there are some general understanding and principle regarding the catalytic mechanism of ORR.

As mentioned previously, the reaction route of ORR is strongly dependent on the properties of the catalyst used, demonstrating that it is primarily an inner-sphere reaction. Thus, it is important to study both the electron transfer process and the interaction between the chemical species involved and the catalysts' surface, when trying to understand the reaction mechanism.

According to the molecular orbital theory, the first electron inserted into the antibonding orbital of O_2 molecule, activates the reactant by weakening the O-O bond, after the initial adsorption of O_2 onto the catalyst. Therefore, it requires a strong interaction between the reactant species and the catalyst's surface, to enable fast heterogeneous electro-catalytic ORR. For that the migration distance of electrons from the electrode to the O_2 molecule is shortened when they become spatially closer. Because a dominant fraction of the best performing precious metal free ORR catalysts found so far are all transition metal containing materials, it's necessary to study the interaction between O_2 molecule and the metal atom/cation. Three kinds of adsorption models have been proposed by literature as shown in **Figure 1.4**.[16, 17]

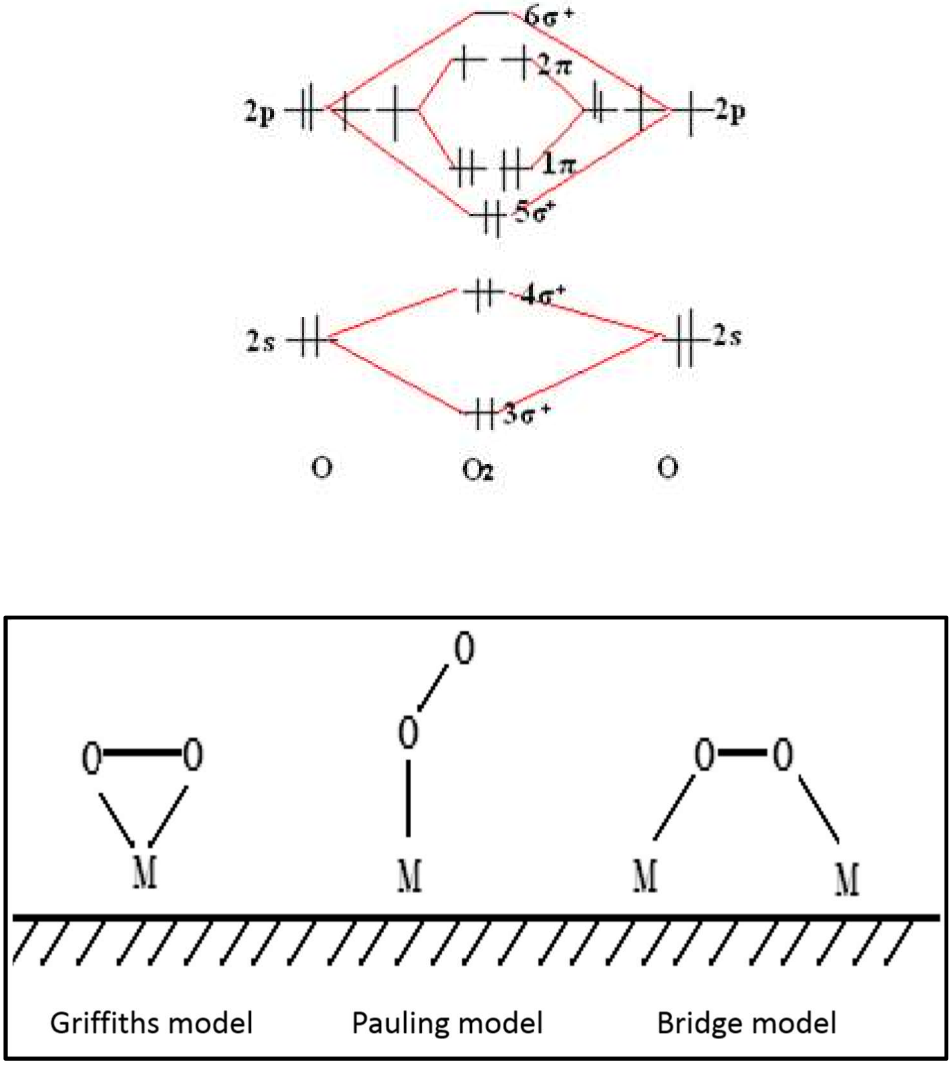

Figure 1.4 Molecular orbital structure of oxygen molecule (above) and three types of proposed adsorption models of oxygen molecule adsorbing on catalyst's surface (down).

In the Griffith model, the two oxygen atoms of an O_2 molecule interact with the same metal atom/cation simultaneously. Electrons of the π-orbital of O_2 molecule interact with the empty d-z^2

orbitals of a transition metal atom/cation, building up a coordination bond, while the electrons from the d-xz and d-yz orbitals of the metal center will partially occupy the π* orbitals of O_2, forming a back bonding. In such process, a strong interaction between the oxygen atom and metal atom/cation is established, while the O-O bond is attenuated and the distance between the two oxygen atoms is increased. This will facilitate the breaking of the O-O bond, and consequently leading to a dissociative adsorption of the oxygen molecule, which is favorable for a direct (4e) pathway of ORR.

However, the most probable form of O_2 adsorption on the surface of a majority of transition metal containing catalysts is the Pauling model, owing to the steric hindrance effect. In this case, O_2 molecule adsorb onto the metal atom/cation adopting an end-on position. The un-bonded electron pair of one oxygen atom approaches the metal center and forms a coordination bond, while stimulating the back flow of electrons from the d-xz and d-yz orbitals of transition metal atom to the anti-bonding orbital of the oxygen molecule. The anti-bonding mechanism facilitates the breaking of the O-O π bond as expected, whereas the resulting hydrogen peroxide intermediate is quite stable. Also, as only the adjacent O atom is sufficiently activated, the breaking of the second O-O bond (σ bond) becomes much harder, rendering the process less favorable for a direct 4e pathway compared to the Griffiths model.

The last proposed adsorption model is the bridge model. The two oxygen atoms interact with two different metal atoms/cations at the same time, building a bridge consisting of two M-O bonds and one O-O bond between the two metal centers. This process promotes the direct (4e) pathway of ORR by activating both of the oxygen atoms, and is more efficient than the Griffiths model. Whereas, such mechanism requires proper surface spacing of the transition metal atoms/cations of the catalysts, and the two metal centers have to possess partially filled d orbitals with proper configuration to bond with the π* orbitals of the oxygen molecule. Which is hard to achieve because most synthetic methods cannot manipulate the structure of the product at atomic level.

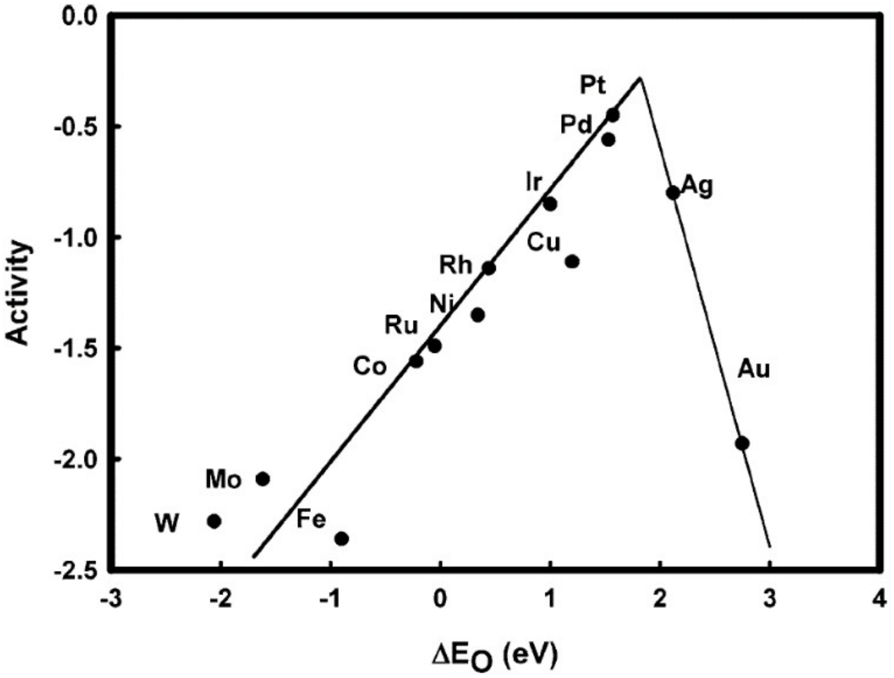

Figure 1.5 Trends in oxygen reduction activity plotted as a function of the oxygen binding energy.[18]

While, although a substantial interaction between the reactant and the electrode surface is needed in promoting a fast inner-sphere reaction mechanism of ORR, it turns out that a too strong bonding between them will play an opposite effect from what is desired.

Norskov et al. studied the relationship between the M-O and M-OH bond energies and the catalytic activity of metal catalysts, through electronic structure calculations combined with detailed density functional calculations.[18]

As shown in **Figure 1.5**, a nice volcano shape appears when plotting the catalytic activity of various transition metals towards ORR, against the oxygen binding energies. On the one hand, for metals left to the vertex of the volcano in the plot, their high oxygen binding energies make it easy for them to form metal oxides. Which indicates that the removal of the adsorbed O and OH species formed after the catalytic reaction is difficult and become the rate limiting step. On the other hand, the metals on the right side of the volcano vertex, because of their full d orbitals, interacts only weakly with the oxygen molecule, which prevents the formation of back bonding between the metal atom and the oxygen atom. As a result, these metal surfaces cannot amply activate O-O bond, leading to poor catalytic activity. While the platinum-group metals, being the closest to the volcano vertex, have moderate oxygen binding energies. Where the M-O interactions are strong enough to promote the cleavage of the O-O bond, yet not too strong to turn the product desorption into trouble.

Although platinum has already got a high catalytic activity for the oxygen reduction reaction, the volcano plot indicates that there is still room for improvement. The binding of oxygen molecule on the platinum surface (Pt (111)) at high potential is still too strong, leading to an over-potential of 300 mV for the oxygen reduction reaction. And it has been proposed that, the most advantageous M-O bond energy for ORR, on the catalyst's surface would be 0.2 eV smaller than that of the Pt-O bond.[19]

According to the d-band center (the average energy of d-band) theory, which is used to interpret the interaction between transition metal surfaces and the adsorbates. The Metal-O bond strength depends on how well the 2p orbitals of oxygen and the d orbitals of transition metal match with each other, as well as the filling condition of the antibonding orbitals formed correspondingly. The more the antibonding states are occupied, the weaker the M-O bond is, and the filling condition is largely decided by the relative position of d-band center to the Fermi level. Shifting the d-band center upwards from the Fermi level will result in an upward shift of the antibonding states, resulting in less occupancy and thus a stronger M-O bond. And vice versa.[20] Therefore, researchers has devoted intensive efforts to adjust the electronic properties of platinum to improve its catalytic activity for ORR according to the above principles. Usually, the method of adjusting the electronic structure of platinum is to alloy it with other transition metals, utilizing strain effect and ligand effect. One example of such alloys is Pt_3Ni, in which the Pt-O bond strength is decreased and the ORR activity of the material increased compared to primitive Pt. The improved acticity of Pt_3Ni and many other platinum alloys proves the validity of using the Metal-O bond strength as an indicator of the catalysts' ORR activity, which also serves as the basis of the designing principle of other types of ORR catalysts.[21-24]

The effects of the size and morphology of catalysts on the activity for oxygen reduction reactions have also been studied in literature. Different opinions exist regarding various specific material systems. Whereas, the explanations proposed all falls within the range of the designing principles discussed previously.[25, 26]

The above studies discussed why platinum catalysts has the highest intrinsic activities towards

ORR among transition metals, the activity descriptor of ORR catalysts, and how the activity of Pt catalysts can be further improved. However, the more fundamental problem about platinum-based catalyst, which is the most efficient and widely used ORR catalysts today, is its high cost and scarcity. Currently, the cost of platinum electrocatalysts accounts for more than half of the whole fuel cell stack cost. Although the anode requires platinum to catalyze the hydrogen oxidation reaction (HOR) as well, the account of Pt required at anode is far less than that of cathode, owing to the intrinsic sluggish kinetics of the 4e ORR process. The precious metal catalyst is the only component in fuel cell that won't benefit from economies of scale, and the increasing demand for fuel cell or metal-air battery power systems will inevitably drive up the already high price of Pt (~ 1000 dollars/ounce). Moreover, the scarcity and the uneven local distribution of the element (South Africa and Russia together host about 97% of the world's total platinum reserve) also forms an intrinsic obstacle for the large scale application of the catalyst, as well as the fuel cell and metal-air battery technologies. Therefore, the development of nonprecious metal electro-catalysts (NPMCs) for oxygen reduction reaction that can replace platinum, is pivotal for the commercialization of both fuel cells and metal-air batteries.

1.3 Goal of the Dissertation

As discussed in the previous sections, one key factor determining the feasibility of the commercialization of fuel cells and metal-air batteries is to replace platinum-based catalysts with non-precious metal catalysts (NPMCs). Therefore, the goal of this dissertation is to study and design highly active and durable NPMCs towards ORR, that deliver promising device performance when employed as the cathode catalyst (as indicated in **Figure 1.6**). High-performance NPMCs reported so far includes transition metal oxides, heteroatom-doped nano-carbon materials and pyrolyzed transition Metal-Nitrogen-Carbon catalyst (Me-N-C).[27] Among which the Me-N-C catalysts is generally accepted as the most promising candidate, because of their high intrinsic activity and stability for ORR. Hence, the current dissertation will focus on the development of Me-N-C catalysts.

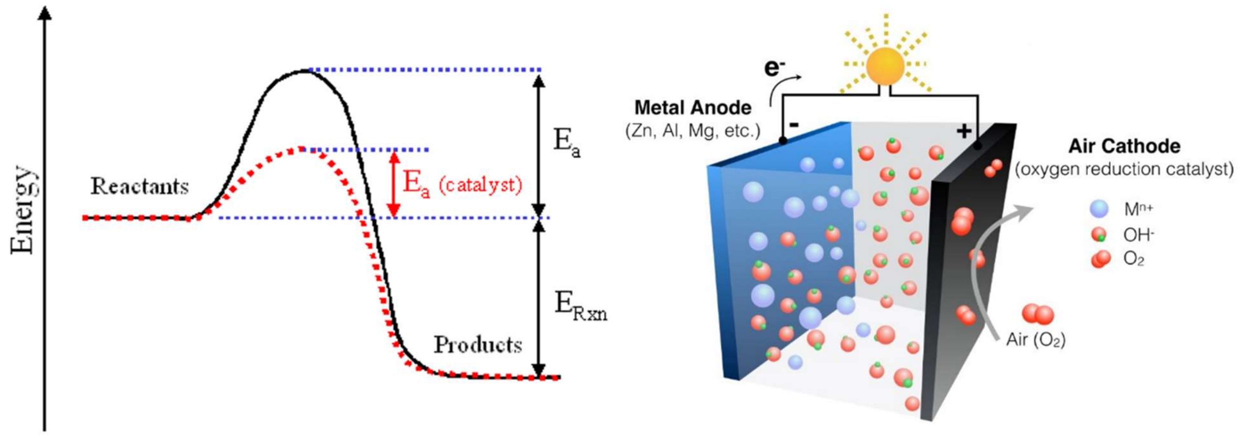

Figure 1.1 Energy diagram of catalytic reaction (left) and the schematic illustration of metal-air batteries.[28]

Chapter 2. Literature Review of Metal-Nitrogen-Carbon (Me-N-C) Catalysts

2.1 History of Me-N-C Catalysts

As oxygen is the most abundant element in the Earth's crust, the oxygen reduction reaction is also one of the most important and common bio-catalytic reaction in living bodies.

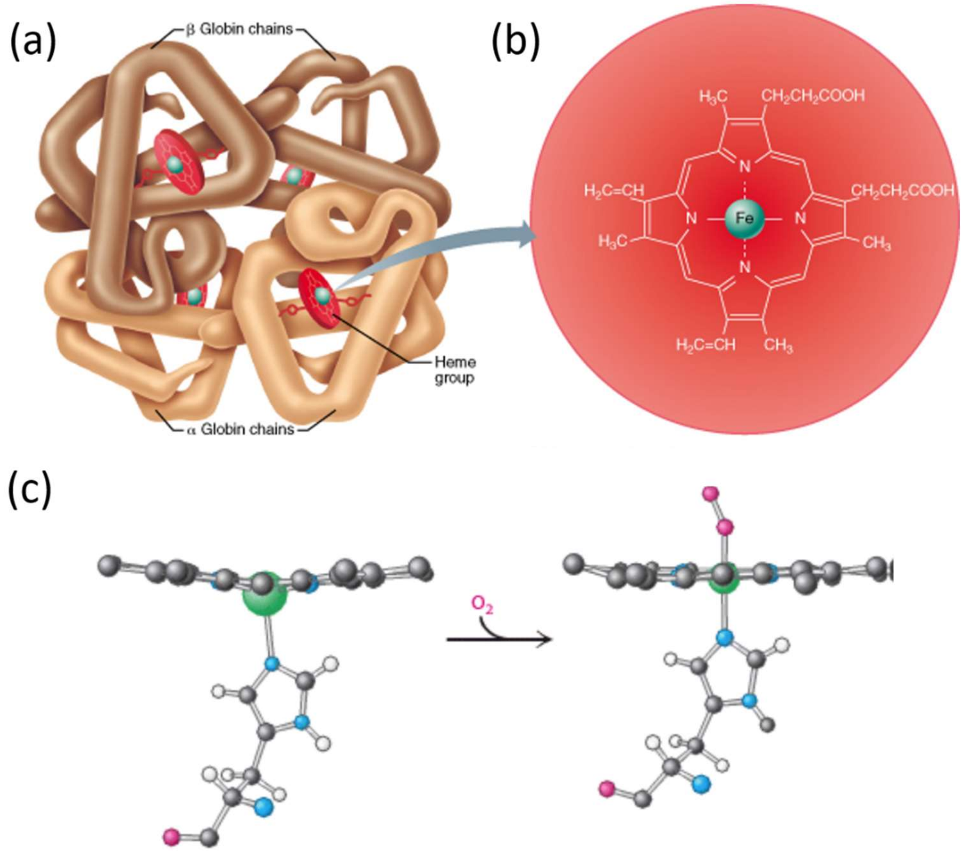

Figure 2.1 (a) Hemoglobin consists of globin (two alpha and two beta polypeptide chains) and four heme groups. (b) Iron-containing heme pigment. (c) 3D structure of heme before and after loaded with O_2.[29]

The bio-catalysts in mammal's body ensures that ORR proceeds at sufficient speeds during respiration, so the cells can gain energy fast enough for carrying out their activities. Therefore, it can be very inspiring for researchers to study the mechanism and structure of the bio-catalysts when designing ORR catalysts for fuel cells and metal-air batteries.[30]

Before ORR takes place, the protein hemoglobin in red blood cells first carries the oxygen molecules breathed in to the cells in need. As shown in **Figure 2.1**, one hemoglobin contains four heme groups, which has a strong affinity towards oxygen molecules. The iron associated with the heme has the flexibility to move in and out of the plane of the porphyrin structure, which enables it to adopt energy-favorable configurations when binding oxygen. It is the iron in hemoglobin that gives blood its red color. Interestingly, though hemoglobin provides only transportation for oxygen, the heme structure is actually very similar to that of the ORR active sites in cytochrome c oxidase (CcO). During the final stage of respiration, cytochrome c oxidase, a membrane–bound enzyme, catalyzes the four-electron reduction of oxygen to water, where cytochrome c serves as the electron donor. As shown in **Figure 2.2**, the active site for oxygen reduction consists of a myoglobin-like Fe-porphyrin (haem-a3) that is adjacent to a semi-haemocyanin-like Cu (known as CuB) coordinated by three histidine ligands. Such smart and subtle bimetallic active site structure enables the oxygen molecule to adopt a bridge-like configuration when adsorbing on the metal centers. Which is advantageous for breaking the O-O bond and is favorable for the 4 electron pathway of ORR. The success of biocatalysts in accelerating ORR in mammal's body is very inspiring for researchers. Since the active sites of both hemoglobin and cytochrome c oxidase have the transition metal-nitrogen coordination structure, research efforts were first focused on exploring molecules that contain similar structures (transition metal porphyrin and transition metal phthalocyanine complexes) as ORR catalysts.

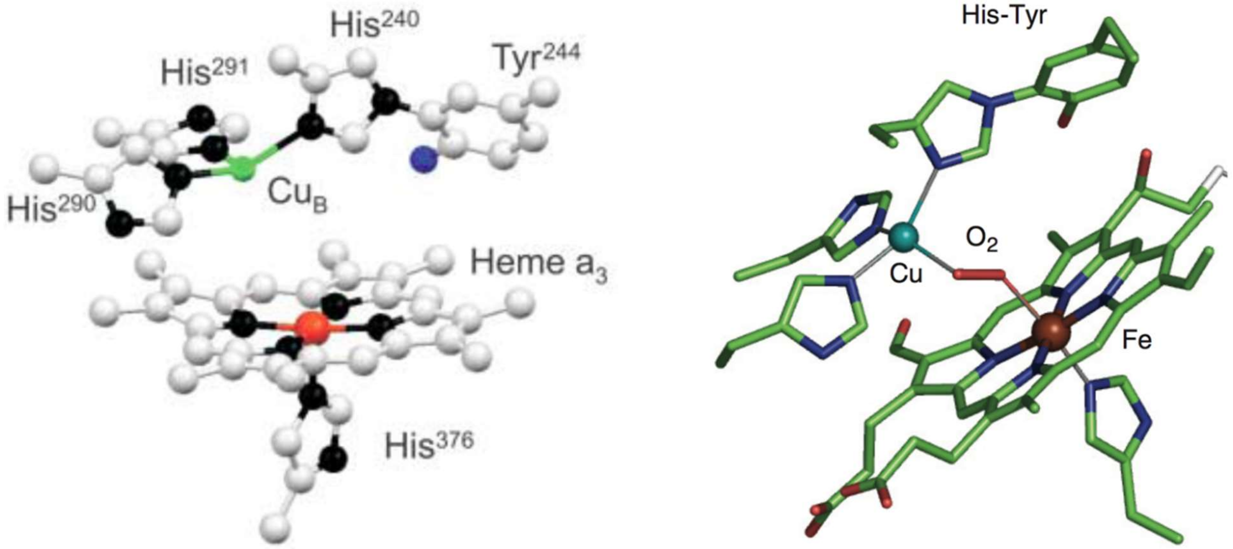

Figure 2.2 Crystal structure of the active site of CcO from the bovine heart (left)[31] and 3D structure of CcO when loaded with oxygen.[32]

In 1964, Jasinski et al. summarized the field and discovered that cobalt phthalocyanine is effective in catalyzing the ORR.[33] Since then, research of the field were directed to exploring the ORR activity of Fe-N_4 and Co-N_4 macrocycles integrated with a carbon support, and several catalysts of improved catalytic activity for ORR had been reported. However, these transition metal-N_4 macrocycle materials are not stable enough in acidic media and dies quickly. Later on in 1970, research found that pyrolyzing the pristine metal centered macrocycle compound can result in better catalytic activity and stability.[34] However, thus synthesized materials still suffer from complicated synthesis process and high price, owing to the indispensability of the expensive macrocycle molecules. One work worth noticing was reported by J. P. Collman et. al. in 1980. In which they fabricated a series of dicobalt face-to-face porphyrin molecules, intelligently mimicking that of the active center of CcO.[35] Whereas, though these bi-active center catalysts effectively promote the 4 electron pathway of ORR, they still lack in activity and stability for applications, just as all the other catalysts fabricated from macrocycle molecules. On the other hand, though the subtle bi-metallic active center is advantageous for the breaking of O-O bond, such structure is too hard to achieve in materials synthesized through pyrolysis. Which is due to the random nature of pyrolytic reactions. A major breakthrough came in 1989, when Yeager et al. synthesized catalysts with high activity by the high temperature pyrolysis of a mixture of individual nitrogen and cobalt precursors and carbon support under inert atmosphere.[36] Which revealed that the high-performing Me-N-C catalysts could be synthesized with cheap individual carbon, nitrogen and metal precursors without the often expensive macrocycle molecules. Ever since, numerous works following similar synthetic routes have been reported, and great progress have been achieved. Which has established Me-N-C catalysts as the most promising non-precious metal electro-catalysts for the oxygen reduction reaction.[37-39] However, many challenges still remain with the development of Me-N-C catalysts. This includes understanding the catalytic functions of different chemical phases of the catalysts, rational design of the catalysts' structure, and the fabrication of air cathode with Me-N-C catalysts that demonstrate superior device performance.

2.2 Active Sites and Catalytic Mechanism of Me-N-C Catalysts

As mentioned in the previous section, ever since the remarkable discovery of Yeager et. al. reported in 1989, high temperature pyrolysis of the mixture of transition metal salts, nitrogen containing molecules and carbon scaffolds has become the “standard” synthetic route for fabricating Me-N-C catalysts. Though great progress of the catalysts’ activity and stability have been made through the careful selection of different precursors and the manipulation of synthetic conditions, it is very challenging to reveal the catalytic mechanism and the identity of active sites of the materials. A variety of iron salts, nitrogen and carbon precursors, and synthetic techniques used for Me-N-C catalytsts synthesis result in highly heterogeneous and complex structures with inconsistent active centers in numerous studies. The active sites structure of Me-N-C catalysts is largely decided by the electronic and geometric configurations of the metal atoms, where even small changes of their chemical environment can lead to different catalytic mechanism and ORR pathways. Moreover, the chaos of the structures and the chemical phases in the reported catalysts has greatly hampered the further development of the catalysts because of the difficulty of structural characterization and active site identification. Various microscopic and spectroscopic techniques, including scanning transmission electron microscopy (STEM), X-ray photoelectron spectroscopy (XPS), electron energy loss spectroscopy (EELS) mapping, Mossbauer spectroscopy and X-ray absorption spectroscopy (XAS) have been applied to characterize the Me-N-C catalysts and study the active site structure. In parallel, electrochemical methods are also used to investigate the nature of the active sites using the ion poisoning effect.[40-42]

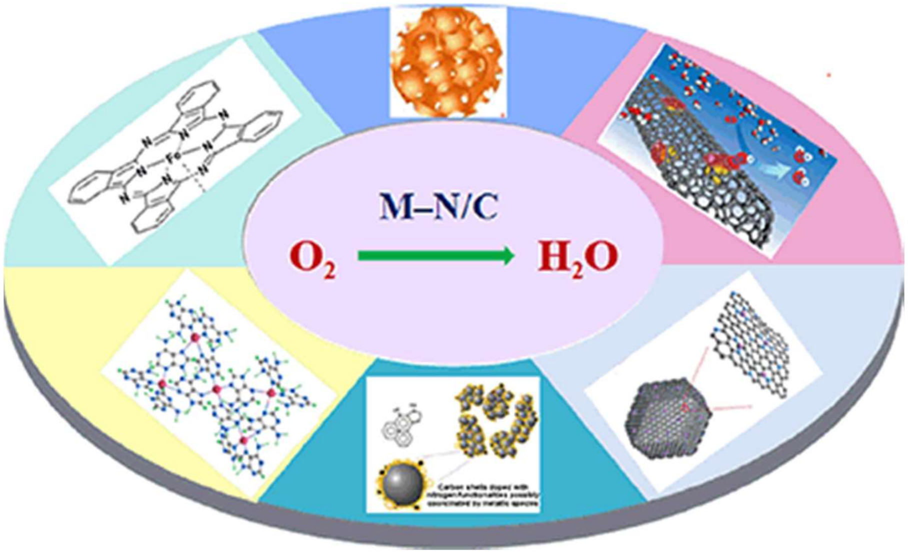

Figure 2.3 Schematic illustration of Me-N-C catalysts with various carbon structure and metal-related chamical phases, synthesized from different precursors.[42]

To date, the Fe-N-C catalysts have been demonstrated to be the most active catalysts for ORR among all the Me-N-C catalysts studied. Three types of active sites have been suggested to account for their high activity,[43, 44] including the iron-nitrogen coordination structure (denoted as Fe-N_x moieties) embedded in carbon matrix, nitrogen-doped carbon coated Fe/Fe_3C nanoparticles, and nitrogen-carbon moieties (C-N_x). The major distinction between the three types of active sites lies in the role of transition metal in active site formation. For the Fe-N_x moieties, the Fe cation is the direct center for binding oxygen, as is the case for non-pyrolyzed macrocycles and CcO.[36, 45, 46] Others state that the Fe/Fe_3C particles entrapped in N-doped carbon layers, though is not in direct contact with oxygen molecule, can modify the electronic structure of the surface carbon layer and turn the latter into ORR active sites.[47-51] Additionally, many researchers argue that the transition metals only catalyze the formation of C-N_x active sites during pyrolysis, but do not participate in catalyzing ORR itself.[52-54] It should also be noted that N-doped carbon is ORR active even without the presence of transition metal in precursor.

2.2.1 The Me-N_x Moieties

Gu et. al. used aberration-corrected STEM and EELS mapping techniques are used to investigate the distribution of different elements in pyrolyzed Fe-N-C catalysts. STEM images confirms the existence of Fe as single atom in many cases besides forming nanocrystals. And the signals of Fe and N are found to be adjacent to each other in EELS mapping spectrum of sub-angstrom level resolution, providing visual evidence for the existence of the Fe-N_x structure.[55-57] The chemical environment of surface Fe in Fe-N-C catalysts is extensively studied with XPS analysis. Which confirms the presence of Fe bound to pyridinic nitrogen at the edge of carbon scaffold.[58-60] Besides showing the existence of Fe-N_x site, various comparison studies are also performed to demonstrate its role as the key ORR active site. Acid treatment are employed in many studies to selectively remove Fe-based nanoparticles without affecting the Fe-N_x centers. Many works report the enhancement of ORR activities of the catalysts after nanoparticle removal, which indicates the necessity of exposing Fe-N_x sites, and that Fe-based nano-crystallites are ORR inactive. [33-35SiO,yadong] Besides, the poisoning effect of many anions with high affinity for Fe cation points out that the catalysts lose their high activity when Fe is blocked, confirming their participation in the ORR process.[61]

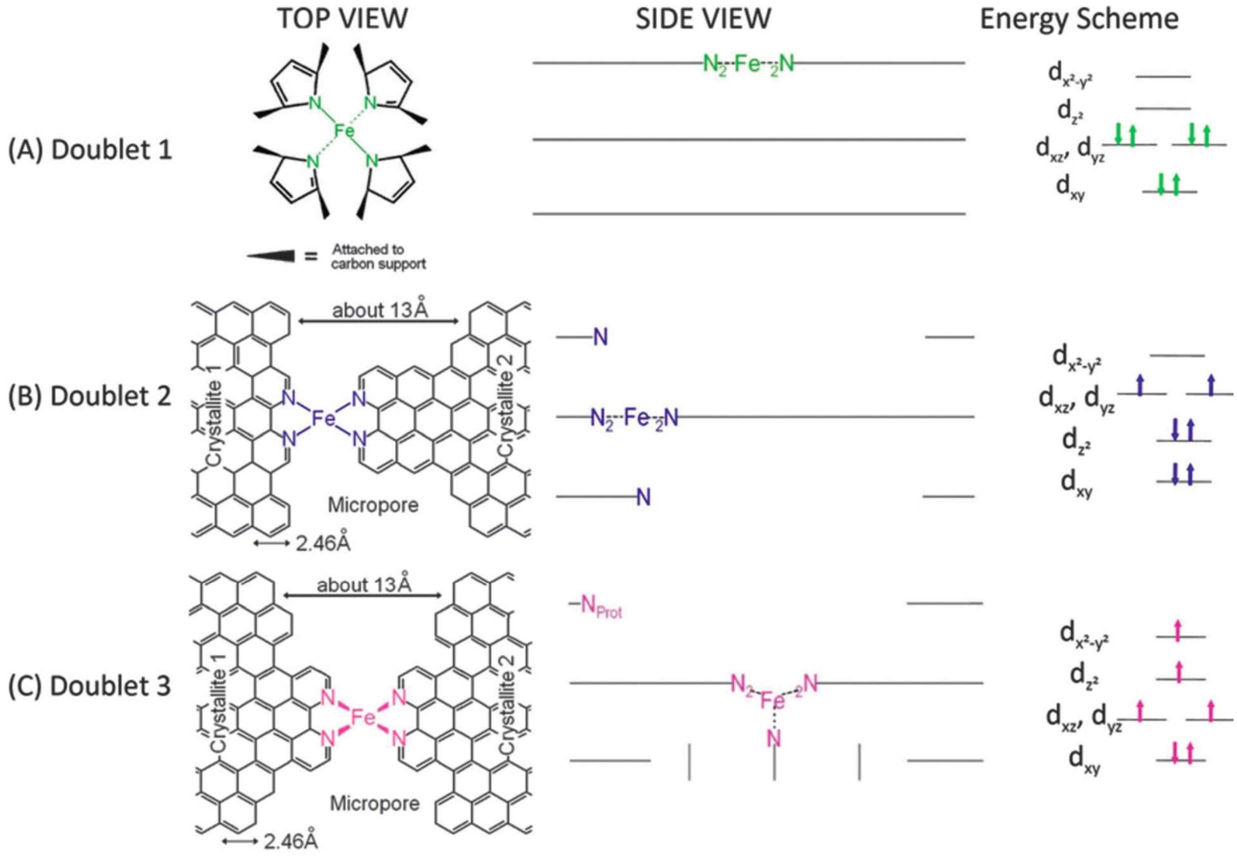

Figure 2.4 Side views and top views of the proposed structures of (a) the FeN_4/C catalytic site in heat-treated, macrocycle-based catalysts assigned to Mössbauer doublet D1, (b) the FeN_{2+2}-like micropore-hosted site found in the catalyst prepared with iron acetate and heat-treated in ammonia assigned to doublet D2, and (c) the N–FeN_{2+2}-like composite site, where N–FeN_{2+2} is assigned to doublet D3. In all side views, the graphene planes are drawn as lines.[62]

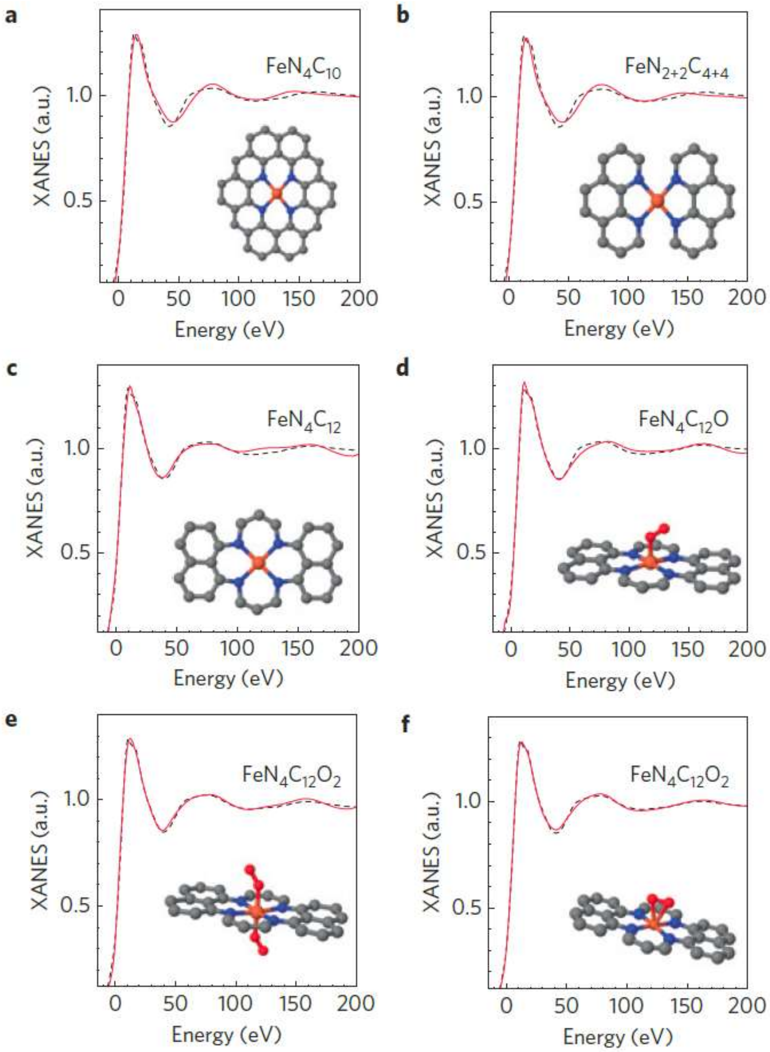

Figure 2.5 Comparison between the K-edge XANES experimental spectrum of $Fe_{0.5}$ (black dashed lines) and the theoretical spectrum calculated with the depicted structures (solid red lines). a. FeN_4C_{10} moiety. b. $FeN_2C_2C_4C_4$ moiety. c. FeN_4C_{12} moiety. d. FeN_4C_{12} moiety with one O_2 molecule adsorbed in end-on mode. e. FeN_4C_{12} moiety with two O_2 molecules adsorbed in end-on mode. f. FeN_4C_{12} moiety with one O_2 molecule adsorbed in side-on mode. The brown sphere represents an iron atom, whereas blue, grey and red spheres identify nitrogen, carbon and oxygen atoms, respectively.[63]

The more accurate identification of the Fe-N_x structure are obtained by X-ray absorption near-edge spectroscopy (XANES) analysis and Mossbauer spectroscopy analysis, which are highly precise to the chemical environment and bonding condition of heavy elements. Plenty of experimental evidence using such techniques has confirmed the existence of several types of Fe-N_4C_{12} coordination structures in the pyrolytically synthesized Fe-N-C catalysts (**Figure 2.4 and 2.5**). While the orbital energy of the central Fe atom is found to be affected by the properties of the carbon support hosting the Fe-N_4C_{12} structure, which is critical for the high ORR activity of the catalyst.[62-67]

According to Sabatier's principle, the high ORR activity of the Fe-N_4 active site is probably attributed to the moderate adsorption strength between the ORR intermediates and the center Fe atom.[45, 68] Mukerjee et al. confirmed the chemical environment of Fe-N_4 structure in macrocycle and polymer derived Fe-N-C materials under ORR operation using in-situ XAS investigation. **Figure 2.6** shows the proposed catalytic mechanism of ORR on Fe-N_x sites in alkaline media. The central Fe resided out-of-plane the reducing of oxygen and moved back to the plane of the four coordinating nitrogen at higher potential. Fe undergoes Fe^{2+}/Fe^{3+} redox transition during the catalytic reaction. The disordered graphitic carbon basal planes serve as electron-withdrawing group surrounding the Fe-N_x structure. Such π-electron delocalization effect cause a downshift of the dz^2 orbital of Fe, weakening its binding strength with reaction intermediates to a favorable level. Moreover, the downshift of the eg orbitals also anodically shifts the Fe^{2+}/Fe^{3+} redox potential and stabilizes the Fe-N_x coordination structure at higher potentials.[45, 69] The above effects together boosts the ability of Fe-N_x active site to reduce oxygen at higher potentials, and offers explanations for the different observed activity of the coordination structure on various carbon matrices.

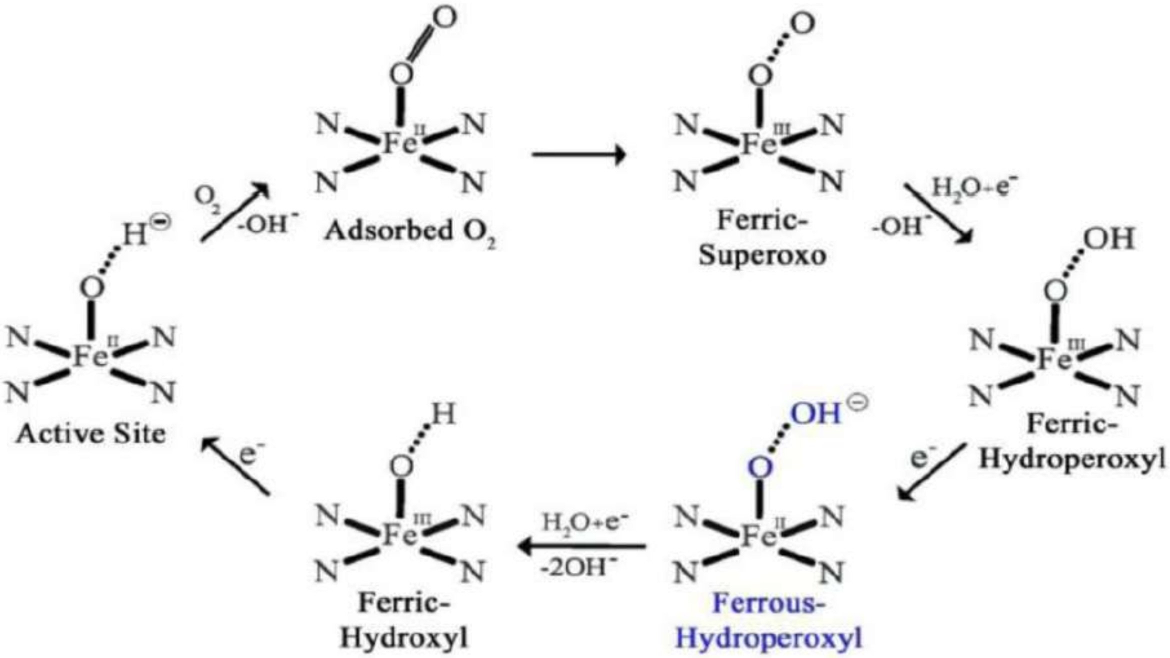

Figure 2.6 Catalyst cycle showing the redox mechanism involved in the ORR on pyrolyzed Fe−N_x/C active sites in dilute alkaline media.[69]

2.2.2 The Fe-based Nanoparticles

Fe-based nano-crystallites (Fe, Fe_3C, FeN, Fe_2O_3 etc.) are commonly formed in Fe-N-C catalysts due to the great tendency of Fe atoms to aggregated under high temperatures. These nanoparticles may not be the targeted chemical phases during synthesis in many studies, and some research allege that they are catalytically inert towards ORR and even impede the Fe-N_x active sites from functioning.[70, 71] Whereas, recent research demonstrate that the nano-crystallites may have very profound and positive affect on the activity and stability of the Fe-N-C catalysts.[48, 51, 64, 66, 72-76]

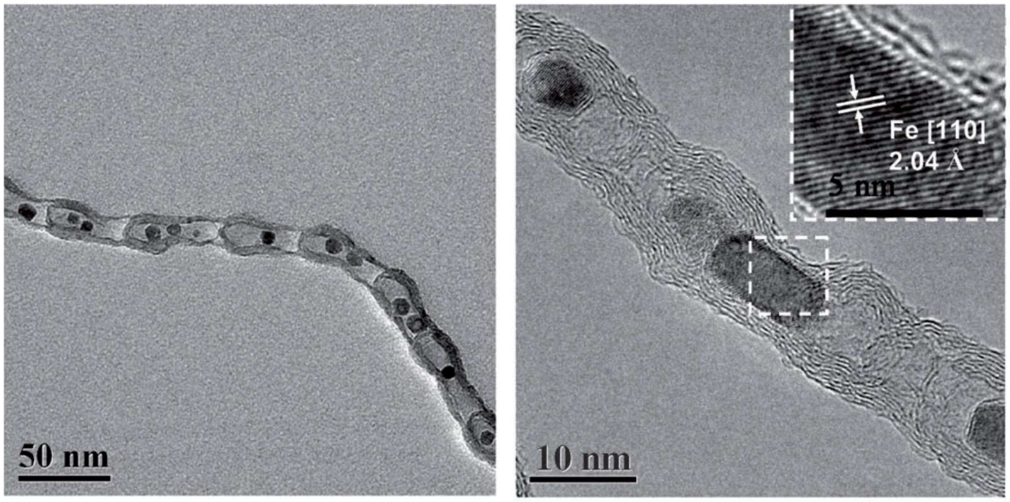

Figure 2.7 TEM image of Pod-Fe (left) and HRTEM image of Pod-Fe with the inset showing the [110] crystal plaine of the Fe particle.[50]

Iron-based nano-particles in Fe-N-C catalysts are usually coated with graphitic carbon layers, because of their ability to catalyze carbon formation during pyrolysis.[77] Bao et al. thoroughly studied these type of encapsulation structure and proposed that the confined metal nanoparticles (NPs) can activate the surface carbon layer for ORR, through a unique host-guest electronic interaction. Specifically, they constructed pod-like CNTs encapsulating Fe and Co NPs (**Figure 2.7**). The coating of carbon layers prevent the Fe NPs from direct interaction with the oxygen molecule, as well as the harsh electrolyte environments, improving the structures' stability, especially in acidic media. Density functional theory (DFT) calculations suggest that the catalytic activity arises from the decreased local work function of the CNT surface, which is due to the electron transfer from metal NPs to CNT. The doping of nitrogen of the carbon layers in addition, makes it more favorable for oxygen adsorption and activation. These effects together result in the high ORR activity and stability of the N-doped carbon layers encapsulating metal NPs.[50] Bao et al. further explored the influence of the thickness of the carbon layers on the ORR activity of Pod-Fe catalyst.[78] Where they found that the ideal number of the coating carbon layers should be 1-3, and the ORR activity decrease drastically with increasing carbon thickness. These results confirmed their host-guest electronic interaction theory and opened a new route for designing ORR catalysts based on the encapsulation structure.

Similarly, Li et al. prepared catalyst of hollow spherical morphology consisting of uniform iron carbide (Fe_3C) nanoparticles encased by graphitic layers.[48] The catalyst is demonstrated to be highly active in alkaline media and very stable in acidic media. The authors claimed that such catalysts contains negligible surface nitrogen and iron according to XPS analysis and thus attributed the ORR activity the carbon layers activated by the Fe_3C particles encased (**Figure 2.8**). The catalyst lost its high activity after the ball-milling and acid leaching, after which the Fe_3C particles were removed.

Further, Mukerjee et al. employed the more precise ex-situ Fe Mossbauer spectroscopy and in-situ synchrotron XAS analysis to study a type of highly active FePhen@MOF-ArNH_3 catalysts. They claimed that the catalyst is predominantly composed of N-doped carbon embedded Fe/Fe_xC

NPs without the presence of any N-Fe bond, proving the activation effect of Fe/Fe_xC particles on the surface carbon atoms.[49] More recently, Lu et al. also observed the activation of carbon shells for ORR by the encapsulated iron and cobalt sulfides.[64] The catalyst possesses prominent activity and durability in alkaline media, and the covalent interaction between metal sulfide particles and carbon shells are elucidated by XAS and XPS analysis.

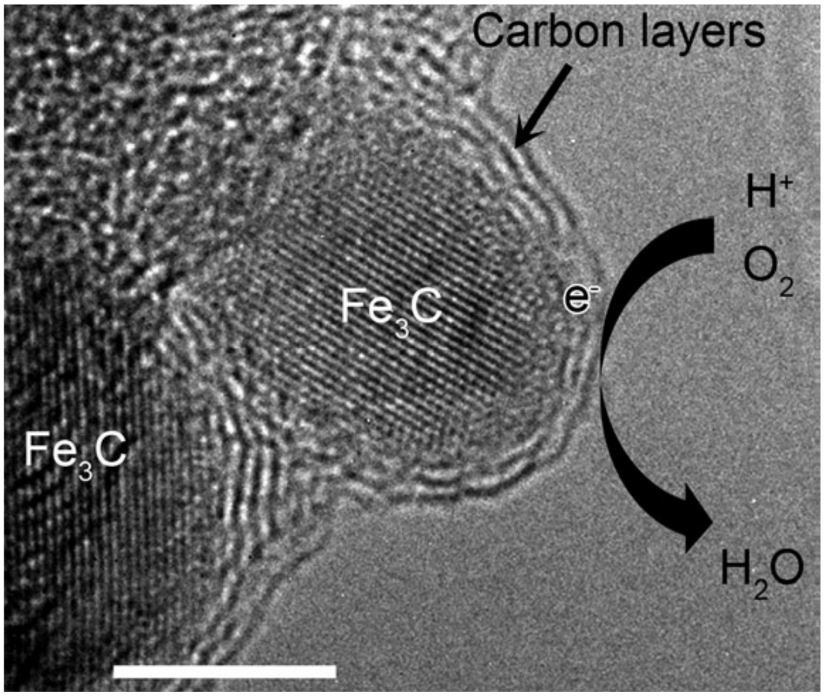

Figure 2.8 Oxygen reduction process on carbon encapsulated Fe_3C nano-crystallites (scale bar = 5 nm).[48]

As the encapsulated metal-based particles can affect the electronic structure surface carbon atoms, it is expected that they can adjust the electron density of other chemical phases in the surface carbon planes as well. Jiang et al. conducted a series of comparison studies of various Fe-N-C catalysts and concluded that the presence of both Fe-N_x and Fe/Fe_3C particles are necessary for achieving high catalytic activity for ORR.[56] The authors found that the presence of encapsulated Fe/Fe_3C nano-crystallites can modify the charge density of Fe atoms in the adjacent Fe-N_x sites, thus boosting its activity. Yet, the activity of the catalyst is greatly compromised with SCN^- in the electrolyte, demonstrating the role of Fe-N_x as the direct ORR active center. Besides the encapsulated metal particles, the presence of iron oxides is also reported to improve the ORR activity of Fe-N-C catalysts through synergistic effect.[79] In summary, metal-based nano-particles are found to have positive effects on the ORR activity of Fe-N-C catalysts. The host-guest electronic effect of confined nano-particles opens new avenues for designing Fe-N-C catalysts with improved activity. However, there is still ongoing debate about the functions of the nanoparticles caused by the complexity of the pyrolytic reaction and the different precursors used in various studies. Therefore, novel synthetic routes of more precise chemistry would be helpful for analyzing the functions of various components in Fe-N-C catalyst towards ORR.

2.2.3 The C-N_x Active Sites

It has been argued by many researchers that metal atoms, instead of catalyzing ORR directly as active sites, only catalyze the formation of the nitrogen sites in the carbon plane (pyridinic N, graphitic N and pyrrolic N), which are the actual active centers (the C-N_x sites).[80-83] The presence of exposed edge-plane defects and nitrogen species are important for the effective adsorption of ORR intermediates.[84, 85] For example, Ozkan and co-workers observed that a high level of pyridinic N doping and large proportion of exposed edge planes of N-doped graphite could dramatically improve the activity of metal (Fe, Co, Ni) based catalysts.[86]

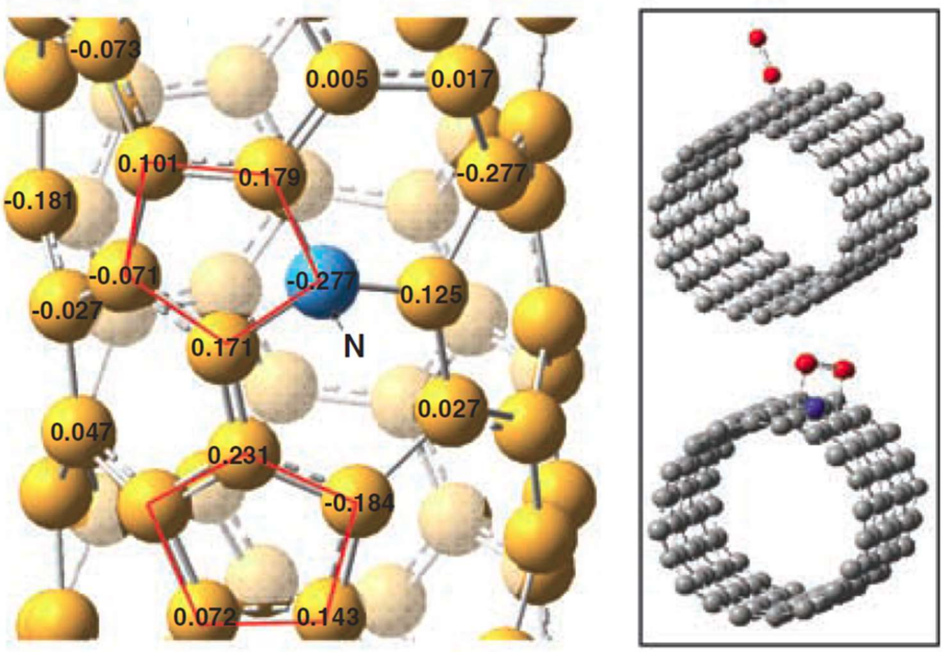

Figure 2.9 Calculated charge density distribution for the NCNTs (left). And schematic representations of possible adsorption modes of an oxygen molecule at the CCNTs (top) and NCNTs (bottom). The C atoms around the pyrrolic-like nitrogen could possess much higher positive charges than do the C atoms around the pyridinic-like nitrogen.[87]

Dai et al. prepared highly active vertically aligned N-doped CNT arrays by the pyrolysis of iron phthalocyanine followed by residual Fe removal.[87] The researchers claimed that the incorporation of the more electron negative nitrogen atoms results in the electronic dipole formation between N(-) and adjacent C(+) atoms. The uneven distribution of charges expedites the chemisorption of oxygen, facilitating the subsequent reduction. Different N species possess varied ORR catalytic functions. First-principle calculations reveals that pyridinic-N and graphitic-N are the dominant C-N_x active sites in nitrogen doped nano-carbon materials.[88] Generally, the doping level of graphitic nitrogen determines the limiting current density of the catalyst, while high level pyridinic-N doping results in high onset potential.[89-91] On the other hand, Guo et al. proposed recently that the carbon atom adjacent to pyridinic-N are the active site for N-doped carbon materials in acidic electrolyte. Which is based on their studies of highly oriented graphite model and N-doped graphene.[52]

However, it has remained highly controversial to attribute the ORR activity of N-doped carbon materials to the nitrogen species, because of the presence of transition metal in the synthetic process. It has been pointed out that even trace amount of metal impurities can greatly influence the catalytic activity of heteroatom-doped graphene.[92] With the observed phenomena in the previous literature, recent studies has established the theory that multiple active sites may work synergistically in Fe-M-C catalysts. In several cases, researchers probed the active site by adding cyanide into the electrolyte, which forms highly stable coordination bond with Fe cation and inhibits the Fe-O interactions. According to the poisoning treatment result, Xu et al. and Chen et al. speculated separately that the ORR active sites are primarily C-N_x species, with a small contribution from trace Fe cations.

2.3 Synthetic Strategies for High-Performing Fe-N-C Catalysts

As the complexity of chemical phases and catalyst structure of pyrolytically synthesized Fe-N-C catalysts have greatly hampered the understanding of the nature of active sites (section 2,2). The random nature of the traditional “mix & pyrolysis” synthetic method for Fe-N-C catalysts has also impeded the rational design of the material. Although some breakthroughs were obtained by the careful selection of different nitrogen and transition-metal precursors, as well as carbon supports, the rational optimization of the catalysts has remained challenging based on such test-and-trial method.[36, 37, 51, 93]

In general, two crucial factors govern the performance of non-precious metal catalysts. 1. Chemical composition and the interactions between different components of the catalyst, which determine the intrinsic activity of the active sites. 2. Porous structure and specific surface area of the catalyst, which determine the accessibility of active sites and the transport conditions of ORR-relevant species (O_2, OH^-, H^+, e^-). The traditional method for preparing Fe-N-C catalysts is based on the direct pyrolysis of the mixture of nitrogen, carbon precursors and transition metal salts and always fails in controlling the above mentioned two properties of the resulting material. Thus, a novel synthetic strategy that enables the rational design of catalyst with desired properties mentioned above and comparable activity and stability to that of Pt/C catalyst will greatly benefit the progress of the field.[93, 94] Herein, we summarize some recent advances to modulate the performance of Fe-N-C catalyst by adopting novel synthetic routes and rational selection of suitable precursors.

2.3.1 Me-N_x macrocycle molecule precursors

Me-N_x macrocycle molecules (metal phthalocyanines, metal porphyrins) have attracted widespread interest because the chemical environment of their metal atom resembles that of the bio-catalysts. However, though such molecules show good selectivity towards 4e ORR, they lacks intrinsically in activity and stability owing to their poor electron conductivity and tendency to aggregate. Despite great efforts, limited progress has been made in improving their catalytic performance. In several studies, researchers tried improving the performance of macrocycles through integrating it with carbon supports (graphene, CNT).[95, 96] For example, Tang et al. reported the fabrication of rGO supported cobalt porphyrin. The π-π interaction between the macrocycle and graphene improved its activity and stability to a level comparable to Pt/C.[97]

As mentioned in the beginning of the chapter, CcO can catalyze ORR with great selectivity for the 4e pathway. Therefore, utilizing macrocycle molecules to mimic the active site in enzyme might results in catalysts that feature the same selectivity. Specifically, the iron active center in CcO resides in a five-coordinated porphyrin ring, with an additional axial ligand. To mimic such structure, similar Fe macrocycles are covalently grafted onto CNTs in two reports, where the catalysts demonstrated improved activity and stability for ORR.[98, 99] Theoretical calculations attributed the improved performance of such macrocycles to the altered energy of Fe 3d orbitals, which is caused by the change of ligand field.

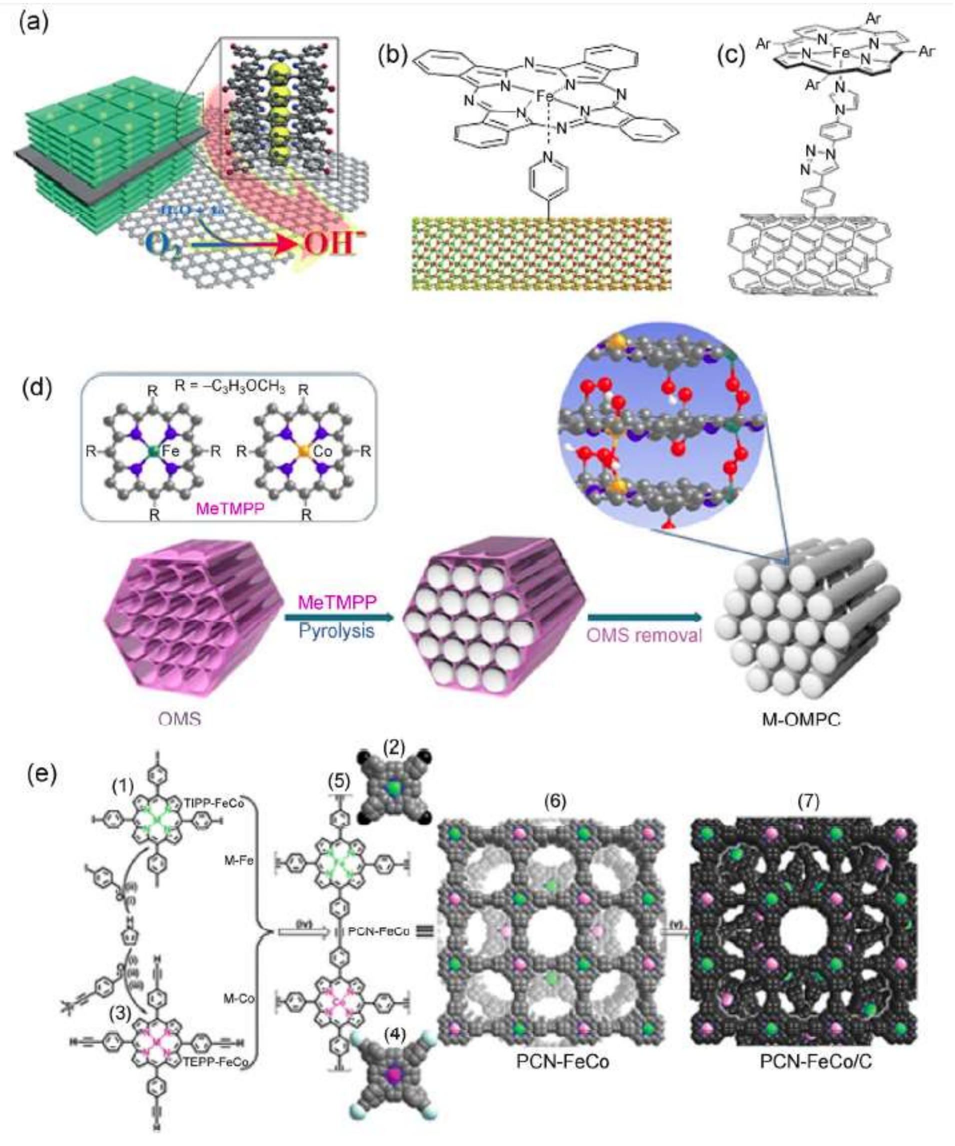

Figure 2.10 (a) The structure of rGO/(Co^{2+}-THPP)n.[97] (b) Schematic diagram of the structure of the FePc–Py–CNT composite.[98] (c) Schematic representation of the bio-inspired ORR catalyst, (2,6-difluorotetraphenylporphyrin (DFTPP))Fe-imidazole (Im)-CNT, covalently anchored to the surface of multi-walled CNTs.[99] (d) Schematic synthetic strategy for FeCo-N-MC.[100] (e) Schematic diagram of the synthesis of PCN-FeCo and PCN-FeCo/C.[101]

Metal macrocycles, unlike pyrolytically synthesized Me-N-C catalysts has well-defined molecular structures, and has recently regained research attention.[102, 103] However, in spite of the progress made, the degradation of the macrocycle structure by ORR intermediates remains a major issue undermining their performance.[104] As pyrolytically prepared Fe-N-C catalysts lacks the above problems, macrocycle molecules have also been explored as the metal and nitrogen source for pyrolysis.[100, 105-107] Interesting progress has been made in the studies, including incorporating Fe porphyrins into carbon organic frameworks for the fabrication of hierarchical porous structure with uniform Fe-N_x center. Whereas, though the macrocycles seem to be advantageous precursor for obtaining Fe-N_x coordination structure during heat treatment, their high price is still a major drawback as mentioned before.

2.3.2 Individual nitrogen precursors

As discussed at the beginning of the chapter, preparing efficient ORR catalysts with individual nitrogen and carbon precursor and metal salts has the advantage of being cost-effective and has thus been the major focus of the field. Particularly, the molecular structure of the starting nitrogen source has significant influence over the chemical environment of N atoms formed in products. Whereas the precise mechanism of nitrogen species growth is too hard to predict for such complex high temperature pyrolysis, leaving alone the rational design of the catalyst. Therefore, the progress of the field has largely relied on the delicate selection of suitable N-containing precursors based on the test-and-trial method. Where typical nitrogen sources include small organic and inorganic molecules (sodium azide, melamine, ethylenediamine, adenine etc.),[36,108-111] and N-containing polymers (polyaniline, polypyrrole, polyacrylonitrile etc.).[37, 112, 113] Thus, a novel synthetic strategy that enables the fine control over the chemical phases and porous structure would be highly desirable for the rational design of Fe-N-C materials.

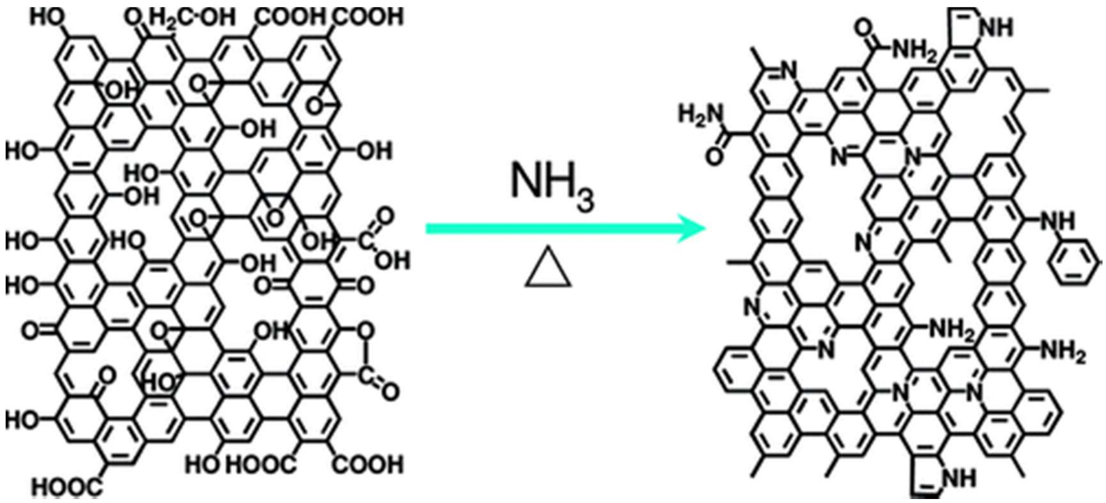

Figure 2.11 Schematic illustration of the etching effect of NH_3 on graphene oxide during heat treatment.[114]

One special nitrogen precursor is ammonia gas. A second pyrolysis in NH_3 atmosphere of the Fe-N-C catalysts prepared by pyrolysis in inert gas is found to significantly increase its catalytic activity. Such NH_3 activation method is based on the etching reactions between ammonia gas and carbon scaffold under high temperature (**Figure 2.11**). The NH_3 etched carbon scaffold show significantly increased micro-porosity and nitrogen doping, as well as increased electronic conductivity. Some studies claim that NH_3 etching can increase Fe-N_x active sites due to increased nitrogen doping level, while others report that it is the increased basicity of carbon support after

NH_3 that boosted the activity of the original Fe-N_x sites.[63, 104, 115] Moreover, the effect of NH_3 may also vary depending on the nature of the carbon support pyrolyzed. For example, Liang et al. reported the thorough study of the NH_3 activation effect on a N-doped mesoporous carbon material prepared by pyrolyzing poly-o-phenylenediamine (PoPD) in argon.[116] They reported in their study that the ORR activity of the NH_3 etched material first grew fast with increasing NH_3 activation duration and reached a plateau after 15 min. Such a trend is almost identical to that of weight-loss percentage and BET surface area with activation duration. Which proves a strong correlation between the ORR activity and the porosity of the catalyst. On the other hand, in contrast to the improved ORR activity, the total nitrogen contents decreased gradually, while the percentage of graphitic-N increased and reached maximum at 15 min. These results suggest that graphitic nitrogen plays important role in determining the activity of PoPD-derived catalsyts, which is supported by theoretical calculations.[117-119] However, despite of the intrinsically high activity, the application NH_3-activated Fe-N-C catalysts is limited by their poorer stability because of the degradation of the C-N_x structures formed.[93, 120, 121]

2.3.3 Metal-organic framework precursors

Metal-organic frameworks (MOFs) have highly porous structure and inherently coordinated metals and rich heteroatoms uniformly distributed in the carbon scaffold, which are advantageous properties for ORR catalysts. Though pristine MOFs suffer from poor electron conductivity, they can be good precursors for fabricating Me-N-C catalysts.[39, 65, 122-126] Heat treatment can transform

MOFs into carbon scaffold with hierarchical porous structure, high surface area and uniform distribution of metal and nitrogen species. Cage containing MOFs can also be used as host for guest metal and nitrogen precursors.

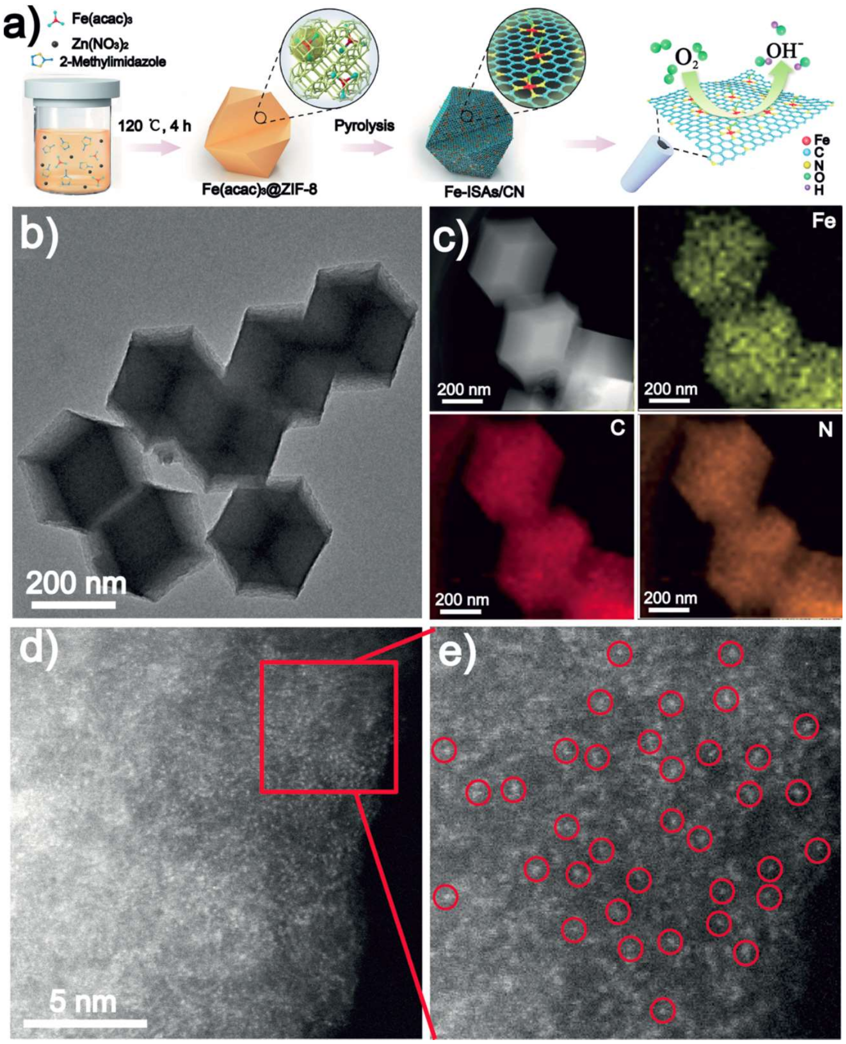

Figure 2.12. a) Schematic illustration of the formation of Fe-ISAs/CN, b) TEM, c) HAADF-STEM image, corresponding element maps showing the distribution of Fe (yellow), C (red), and N (orange), d),e) HAADF-STEM images and enlarged images of the Fe-ISAs/CN. Single Fe atoms highlighted by red circles.[71]

Li et al. recently reported the usage of N-rich MOF as precursor for fabricating catalysts with isolated single metal atoms without metal NPs, which is hard to achieve in high temperature pyrolysis.[71] Specifically, the cages of pristine MOF are used to host metal salt molecule of suitable size to form a complex. By keeping the concentration of metal atoms low enough, no NPs appears in the pyrolyzed complex, because of the binding of rich N atoms and the distance between metal atoms in the crystalline structure of the MOF host.

However, though MOFs have been demonstrated to be advantageous in many aspects for preparing Me-N-C catalysts (ordered porosity, high surface area, abundant metal atoms and heteroatoms), there is still very limited understanding of the transformation mechanisms. Additionally, using MOFs as single precursor provides quite limited adjustability of its structure and composition. Yet reacting the bulk MOF with other metal and nitrogen precursor increase the cost and likely cause inhomogeneity in the product. Therefore, further investigations and novel synthetic strategies are needed for understanding MOF-derived catalysts and achieving better performance.

2.3.4 Templates methods

Besides the intrinsic activity of active sites, the surface area and porous structure, which determines the accessibility of active sites and the transport of reaction-related species are also two key factors governing the performance of ORR catalysts.

The template-directed method is the most straightforward and effective way in fabricating

ORR catalysts with desired porosity.[59, 94, 127, 128]

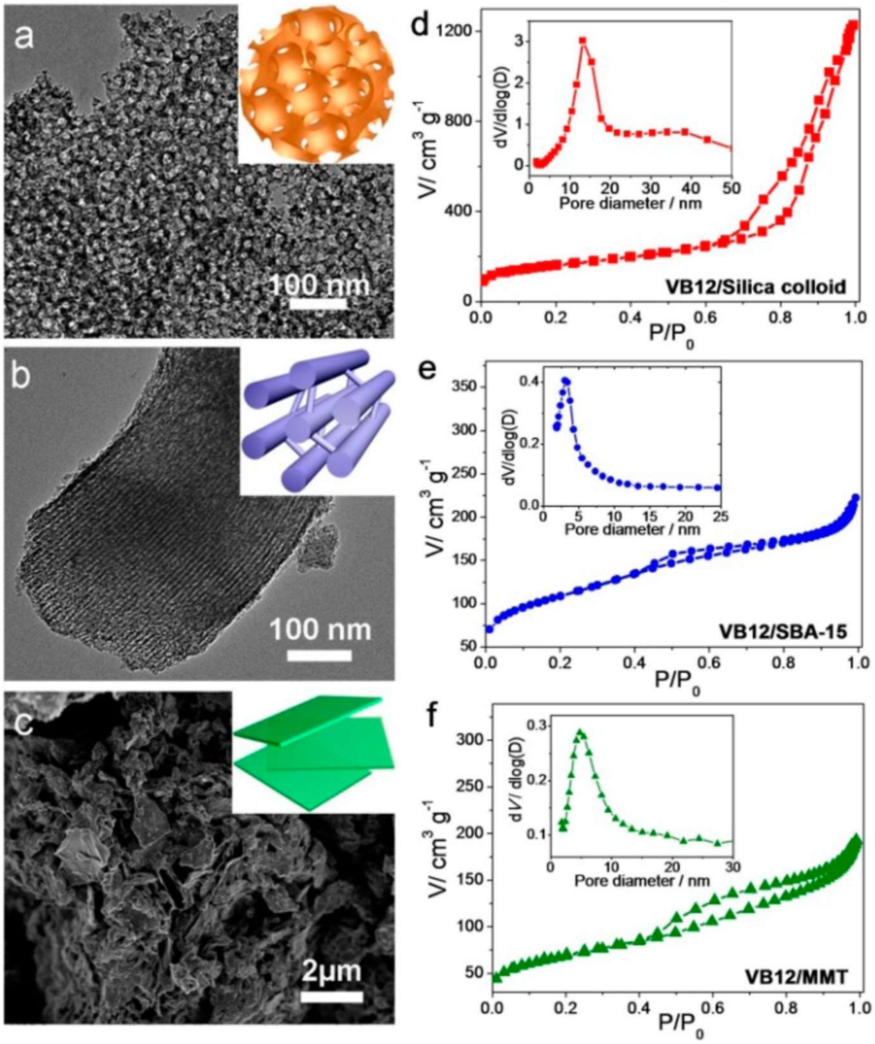

Figure 2.13. (a,b) TEM and (c) SEM images of as-prepared C−N−Co catalysts: (a) VB12/Silica colloid, (b) VB12/SBA-15, and (c) VB12/MMT. Insets in (a−c) are the model illustration of the catalysts with various mesoporous structures. (d−f) N_2 sorption isotherms of these three C−N−Co catalysts. Insets show the pore size distribution from the BJH method of corresponding samples.[94]

Liang et al. successfully prepared a family of Vitamin B12 (VB12) and polyaniline-Fe complex derived mesoporous Me-N-C catalysts.[94] Different pore diameter and surface areas were easily obtained by choosing various templates (silica colloid, SBA-15, MMT) as shown in **Figure 2.13**. The VB12/silica colloid derived sample exhibited the highest BET surface area (572 m^2/g) as well as the highest ORR activity. The good ORR performance of the catalyst is also attributed to its well-defined porous structure as well as a narrow mesopores size distribution. Recently, Sa et al. reported an inventive way of utilizing silica templates to enable the preferential formation of Fe-N_x active sites in pyrolytically synthesized Fe-N-C catalysts without Fe aggregation.[70] Specifically, they adsorbed iron porphyrin onto CNT, followed by silica layer overcoating and high temperature pyrolysis. The silica layer were etched away by HF after pyrolysis. The resulted particle free Fe-N-C catalyst exhibited better ORR activity in terms of half wave potential compared to that synthesized without silica coating, as well as a high device performance (320 A cm^{-3} in acidic PEMFC). Yet, the control samples with Fe-based particles consistently showed higher limiting current density than the catalysts prepared with silica-coating. Which indicates that these NPs could catalyze the reduction of HO_2^-, which is the product of 2e ORR, completing the 4e reduction of oxygen.

Nonetheless, despite the effectiveness of rigid template approach, such method inevitably involves the preparation and removal of template particles, which makes the process tedious and hinders its scalability and economy. In this regard, thermally sacrificial template appears a more efficient way of preparing Fe-N-C catalysts with controlled porosity, such as FeO(OH).[127] Which however, still requires the careful preparation of templates. Preexisting 3D porous carbon architectures as CNT, carbon nano-fiber and 3D graphene could provide a carbon skeleton for the growth of metal and nitrogen species during pyrolysis.[129-132] Yet, such approach lacks in controllability over the porosity of the product compared to the template methods, and the active site formation process is still random in nature, as is that of the traditional “mix & pyrolysis” method.

Chapter 3. Literature Review of Other Non-Precious Metal Catalysts

Besides the pyrolyzed Me-N-C catalysts, transition metal oxides and heteroatom-doped carbon materials have also been extensively investigated as alternative ORR catalysts to the precious metal based catalysts. Though these two types of materials lacks in intrinsic activity compared with Me-N-C catalysts, the study of the nature of their active sites and catalytic mechanism can shed light on the understanding of Me-N-C catalysts. Which helps the designing of Me-N-C catalysts of improved ORR performance. As the current dissertation focus of the development of Me-N-C catalysts, metal oxide catalyst and heteroatom-doped carbon catalysts will not be extensively discussed.

3.1 Metal oxide based materials

Non-precious transition metal oxides are poor electron conductors because of their large bandgaps. So to achieve meaningful electro catalytic activity, they are always combined with carbon supports to form composite materials, or get modified through doping or introducing defects to enhance their electronic conductivity. These non-precious transition metal oxide based materials have the advantage of being earth abundant, cheap and environmental friendly. Particularly, the 3d transition metals of the VIIB group and the VIII group (like manganese, iron, cobalt and nickel) possess various valence states and oxide forms. And it has been found that through adjusting the valence state of the metal atom (electronic structure), the crystallinity of the oxides and the materials' morphology, these non-precious transition metal oxide based materials could have reasonable electro catalytic activity and stability for the oxygen reduction reaction in alkaline media.[133-135]

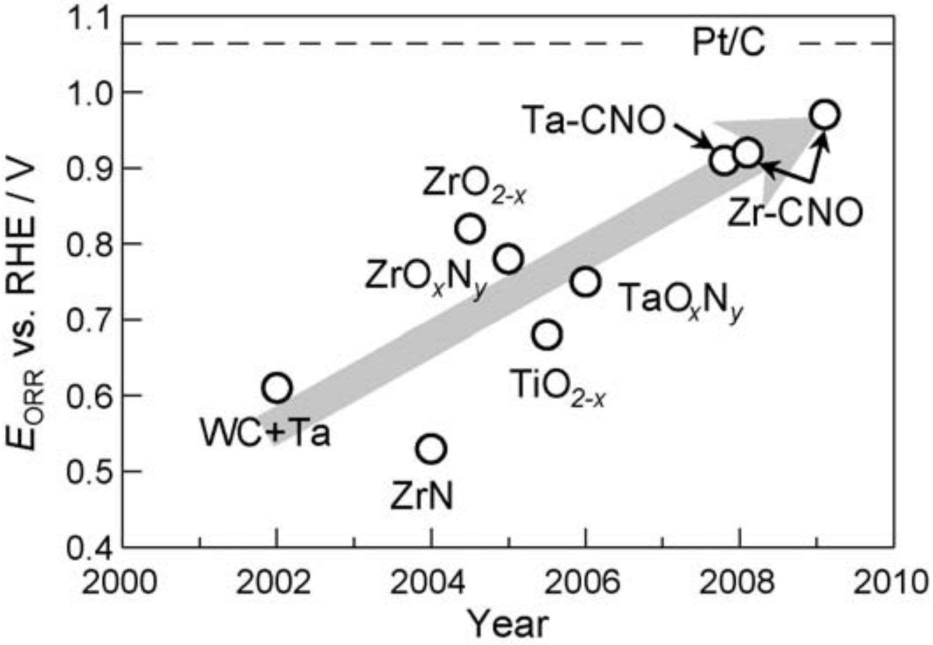

Figure 3.1. Summary of the progress over recent years with respect to transition metal oxide, carbide and nitride based materials as ORR electrocatalysts.[136]

Basically, the unsaturated metal cation on the oxide's surface serve has the active site for this kind of materials for its ability to bind oxygen. And thus, the ORR performance of the catalyst is greatly decided by the electronic structure of the metal cation. For example, it has been found that for perovskite catalysts, the filling condition of the e_g orbital is the key factor influencing the ORR activity. According to geometric considerations, only the $d_z{}^2$ orbital of metal cation can effectively overlap with the π* orbital of oxygen. And the existence of one e_g electron is very important to facilitate the adsorption of oxygen on the active site. For when e_g filling is larger than one, oxygen becomes less advantageous in the competition for active site with hydroxyl anion. However, when the e_g filling is less than one, intermediates like hydroxyl group will bind the active site too strongly, in which case the desorption and final reaction steps of ORR become rate limiting.[135]

However, though catalysts performing well in alkaline electrolyte could be of use for alkaline fuel cell and metal air battery, they are ineligible for proton exchange membrane fuel cell. Which has the most mature technology among fuel cells today, and is the closest to large scale commercialization. Unfortunately few of the non-precious metal transition oxides are stable in acidic and oxidizing conditions. And research regarding this kind of materials has been relatively silent compared with other kinds of catalysts for acidic fuel cell.

Nevertheless, the electro-catalytic performance of the handful of metal oxides that are stable in acidic electrolyte (zirconium oxides, tungsten oxides, titanium oxides and tantalum oxides etc.) have also been studied, as proton exchange membrane fuel cell (PEMFC) cathode catalyst. And so have their carbides, oxy-nitride and carbo-nitride derivatives. As shown in **Figure 3.1**, progress has been made in this field over years. Although in some cases, the metal oxides materials show improved onset potential for ORR and even similar to that of platinum, it still lacks in mass specific current density, owing to poor transport of electrons to the active sites.[104, 136, 137]

In summary, non-precious transition metal oxide based materials showed good performance for ORR in alkaline media. While they are still insufficient for application and is not eligible for PEMFC owing to the low intrinsic activity and poor electron conductivity.

3.2 Heteroatom-doped carbon materials

There has been a fast development of metal-free, heteroatom doped carbon materials as electro catalyst for the oxygen reduction reaction between the year of 2009 and 2015. Catalysts of this class possessing comparable activity to platinum, or even better activity than platinum in alkaline electrolyte have been reported several times. Carbon materials are potential electro catalyst for ORR because of the high mobility of electrons on the graphite plane, and the abundance of delocalized π electrons. But as the graphitic structure is relatively stable, carbon materials alone are not active enough in catalyzing reactions. However this problem could be solved by heteroatom doping of various carbon structures (graphene, CNT etc.). The electronic structure of carbon materials could be easily adjusted by adding dopant atoms that have different electro-negativity and number of valence electrons. In the doping process, a redistribution of atomic charge density (creation of dipole in the non-polar carbon structure) and spin density is introduced, and the HOMO-LUMO gap of the carbon material could also get decreased, leading to low kinetic stability and high chemical reactivity.[87, 138]

In 2009, Dai et al. reported the fabrication of vertically aligned nitrogen-doped carbon nanotubes through the pyrolysis of iron(II) phthalocyanine, and complete removal of the residual Fe by electrochemical purification. Thus prepared material exhibited almost the same half wave potential as that of a 20% Pt/C catalyst, and stayed stable up to 100,000 cycles of potential cycling in 0.1 M sodium hydroxide. The authors attributed the enhanced activity to the relatively high positive charge density on carbon atoms adjacent to nitrogen atom, which could serve as the active sites and promote a side on adsorption of oxygen, facilitating a fast dissociative 4e pathway of ORR.[139] In the same year, Chen et al. reported another case of nitrogen-doped carbon nanotubes, with an even slightly higher half wave potential than that of similar Pt/C catalyst. In this case the authors concluded that the increased nitrogen content and defects led to the enhanced ORR performance of the material.[140]

In 2012, Dai et al. reported the synthesis of two BCN (boron and nitrogen co-doped carbon) materials with improved activity and stability for ORR in 0.1 M potassium hydroxide.[55, 141] In the first study, they synthesized vertically aligned BCN nanotubes by pyrolysis of melamine diborate, and the material demonstrated almost the same half wave potential to that of 20% Pt/C electrode. Which lost 10% of the current density after 50,000 seconds of continuous oxygen reduction at -0.2 V (vs. SCE). In the second case, BCN graphene was synthesized by annealing graphene oxide in the presence of boric acid under ammonia atmosphere. The resultant material showed slightly higher half wave potential than the BCN nanotubes, but worse stability, loosing10% of the current density after 40,000 seconds of continuous oxygen reduction under the same condition. The authors attributed the superb performance of the material to a reduced HOMO-LUMO gap of the material and increased spin and charge density on carbon atoms endowed by a moderate co-doping of boron and nitrogen. However, over doping is found to increase the energy gap, and reduce the conductivity of the material, compromising the catalytic activity.

Afterwards, various materials of similar half wave potential and stability for ORR in 0.1 M potassium hydroxide have been reported. Other dopant elements like phosphor and sulfur have also been explored.[142, 143] However, no major breakthrough has been seen till today. The reported catalysts though show similar activity to that of Pt/C catalyst, lacks in stability compared to the goal set by DOE of 5000-hour durability.

Moreover, the high activity and stability of heteroatom doped carbon materials is only seen in alkaline electrolyte. The catalytic performance of this class of materials still needs further improvement to meet the requirement for acidic fuel cells. [89] While the low density of these carbon based materials is another issue, which tends to increase the thickness of the catalyst layer needed in a real device, increasing the mass transfer resistance. Thus, designing porous 3D carbon structure with increased active site density could be a future direction of development for this class of catalysts.

Chapter 4. Objective of this Dissertation

As discussed in the precious two chapters, there are currently two major issues impeding the development of Fe-N-C catalysts: 1. Difficulty in identifying the nature of the active site and understanding the interaction and synergistic effect between different chemical phases in catalyzing ORR. This is caused by the complexity and the random nature of the traditional “mix & pyrolysis” synthetic strategy, which results in the inconsistency of controlled parameters between comparison studies. 2. Difficulty in designing a synthetic strategy that simultaneously construct dense active sites and advantageous hierarchical porous structure for mass transfer, while retaining being economic and easy scalable.

Therefore, the objective of this dissertation is designing a series of model catalysts that helps the understanding of active site formation in Fe-N-C catalysts and understanding the catalytic functions of different chemical phases towards ORR. Afterwards, on the basis of the established understanding, design an economic and easy-scalable synthetic route for fabricating Fe-N-C catalysts of superior catalytic activity and device performance that promises the replacement of Pt/C catalysts.

Chapter 5. Post Iron-Decoration of Mesoporous Nitrogen-Doped Carbon Spheres for Efficient Electrochemical Oxygen Reduction

5.1 Introduction

Developing non-precious-metal catalysts (NPMCs) for oxygen reduction reaction (ORR) is critical for fuel cells and metal-air batteries.[7, 113, 144] Among a wide range of NPMCs explored in the recent decades,[87, 104, 134, 135, 145, 146] the composites based on pyrolyzed iron-nitrogen-carbon (Fe-N-C) have been regarded as the most promising candidates because of their high activity.[37, 48, 56, 60, 69, 125, 147, 148] Generally, two types of Fe-containing moieties, namely nitrogen-coordinating Fe sites (Fe-N_x) and Fe-containing nanocrystals, have been regarded relevant to their ORR activity.[48, 50, 56, 61, 70, 149, 150, 151] In addition, nitrogen doping within the carbon supports may also play important roles in the ORR activity.[63, 152, 153] As-doped nitrogen participates the formation of the Fe-N_x sites and may enhance catalytic activity through altering the local electronic states of the carbon supports.[63, 69, 153] Furthermore, it has been suggested that doping carbon with nitrogen may generate carbon-nitrogen-based active sites (C-N_x),[52, 87] which also exhibit good ORR catalytic activity.

The synthesis of Fe-N-C catalysts is generally achieved by pyrolysis of precursors containing moieties of nitrogen (e.g., melamine, polypyrrole, cyanamide), carbon (e.g., glucose, carbon black, carbon nanotubes), and iron (e.g., iron nitrate, ferrocene)[48, 56, 125, 148] During the pyrolysis process, reactions occur among these moieties, leading to the formation of nitrogen-doped carbon scaffolds with C-N_x sites, Fe-N_x sites, Fe and Fe_3C nanoparticles. For such a high-temperature pyrolysis process, various reactions occur simultaneously, such as carbonization of carbon precursors to form porous carbon frameworks, and reactions of the iron moieties to form Fe and Fe_3C nanoparticles. These reactions are highly complex and difficult to be deconvoluted, making the rational synthesis of the catalysts difficult.

Herein, we report a synthesis of Fe-N-C catalysts through a growth of active sites on preformed nitrogen-doped mesoporous carbon (NMC) with controlled pore structure and doping of nitrogen. Iron pentacarbonyl $Fe(CO)_5$, a liquid molecule with a boiling point of 103 °C is used as the iron precursor. $Fe(CO)_5$ decomposes at 180 ºC forming metallic Fe and releasing CO, and the carbonyl ligands are easily substituted by Lewis bases. It is expected that $Fe(CO)_5$ could wet the NMC surface and complex with the nitrogen-containing sites, facilitating the formation of active Fe-N_x sites and Fe nanoparticles on NMC upon its decomposition at elevated temperature. Compared with the state-of-art synthesis of Fe-N-C catalysts, this approach provides a pathway to simultaneously control the pore structure, nitrogen doping level, and the chemical environment of the active sites. With the development of nitrogen-doped carbons possessing better controlled pore structure and composition, this method could enable more rational design of Fe-N-C catalysts with better catalytic performance.

5.2 Experimental

Synthesis of Fe/NMC catalysts

In a typical synthesis, NMC (15 mg) was dispersed in ethyl ether (0.4 ml), followed by the addition of iron carbonyl (18.5 µl). The suspension was placed under room temperature for 2.5 h to fully vaporize the solvent, and the resultant precursor was heated to 800 °C at a heating rate of 15 °C min-1 under flowing nitrogen. The Fe/NMC-11 catalyst was obtained after 1 h of pyrolysis. The Fe/NMC-1 and Fe/NMC-30 catalysts were prepared using the exactly same procedure except for adding 1 µl and 50 µl instead of 18.5 µl of iron carbonyl respectively. The number in the notation of samples refers to the molar percentage of Fe with respect to the NMC host (assuming only carbon), based on the feeding amount of $Fe(CO)_5$ and NMC.

Characterizations

Scanning electron microscopy (SEM) and energy dispersive spectra (EDS) were performed on a Nova 230 Nano SEM. Transmission electron microscopy (TEM) images were acquired on a FEI T12 transmission electron microscope operated at 120 kV. HAADF-STEM image, EDS elemental mapping and EDS linear scan were taken on FEI Titan. HRSTEM observation was carried out on a JEOL ARM200F (JEOL, Tokyo, Japan) STEM operated at 200 kV with cold field-emission gun and double hexapole Cs correctors (CEOS GmbH, Heidelberg, Germany). The attainable spatial resolution defined by the probe-forming objective lens is better than 80 picometers. X-ray photoelectron spectroscopy (XPS) tests were performed with Kratos AXIS Ultra DLD spectrometer with a monochromatic Al K α (1486.6 eV) source. XPS is calibrated using the peak position of C 1s spectrum (284.6 eV). Nitrogen sorption isotherms were measured at 77 K with a Micromeritics ASAP 2020 analyzer. X-ray diffraction measurements were taken on Rigaku X-ray powder diffractometer using the copper Kα radiation (λ=1.54 Å).

Electrochemical tests

All electrocatalytic measurements are carried out in a three-electrode cell using a rotating disk electrode (RDE, PINE Research Instrumentation) with a WaveDriver 20 (PINE Research Instrumentation) electrochemical workstations at ambient temperature. A graphite rod and a Ag/AgCl (saturated KCl) were used as the counter and reference electrodes, respectively. A glassy carbon (GC) electrode was used as the substrate for the working electrode. To prepare the working electrode, 5 mg of the catalyst was dispersed in 1 mL of ethanol and 30 ul of 5 wt % Nafion solution by ultrasonication. A certain volume of the suspension was pipetted on the GC surface and dried at ambient temperature. RDE measurements for ORR were perform in O_2 saturated 0.1 M NaOH electrolyte with a scan rate of 10 mV s^{-1}. The polarization curves were corrected with background current and iR loss. Background current was scanned in N_2 saturated 0.1 M NaOH. Solution resistance is determined by the high frequency intercept in the Nyquist plot from electrochemical impedance spectrum and used for iR correction. Potentials in this study refer to reversible hydrogen electrode (RHE). The reference electrode was calibrated by conducting cyclic voltammetry (CV) scan with Pt/C on GC as working electrode in H_2 saturated 0.1 M NaOH. The potential where current crossed zero was the thermodynamic potential for the hydrogen electrode reaction. In 0.1 M NaOH, E(RHE) = E(Ag/AgCl) + 0.942 V. Stability of the catalysts were evaluated by conducting CV scans between 0.6-1 V vs. RHE at 100 mV s-1 in O_2 saturated electrolyte for 5000 cycles.

5.3 Results and Discussion

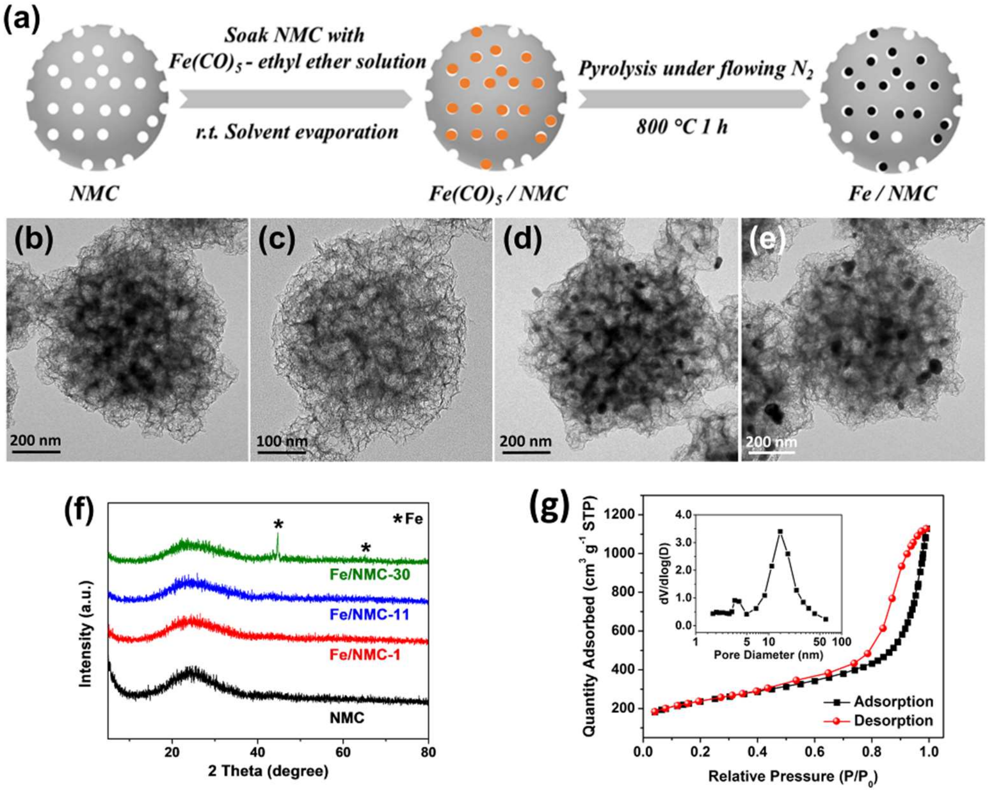

Figure 5.1. (a) Synthesis of Fe/NMC catalysts. TEM images of (b) NMC; (c) Fe/NMC-1; (d) Fe/NMC-11; and (e) Fe/NMC-30. (f) XRD patterns of NMC, Fe/NMC-1, Fe/NMC-11 and Fe/NMC-30. (g) N_2 sorption isotherms and pore size distribution (inset) of Fe/NMC-11.

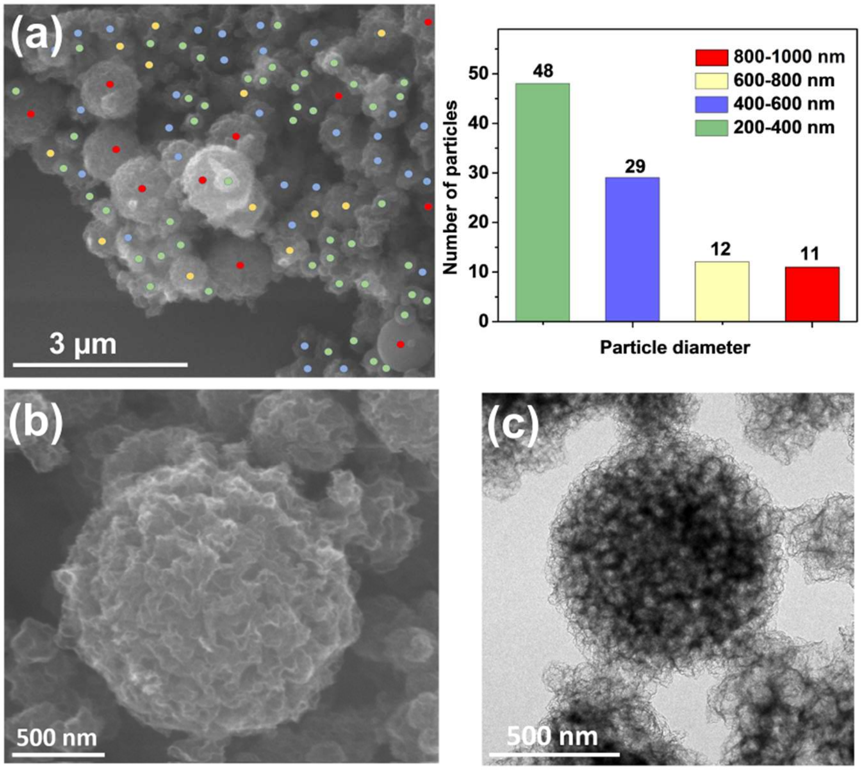

Figure 5.2. (a) SEM image and particle size distribution (based on 100 particles) of NMC, (b) SEM image and (c) TEM image of NMC.

The preformed nitrogen-doped carbon particles, NMC, was first prepared by an aerosol-assisted method[154] (See **Figure 5.1a** and the details of materials synthesis in Experimental Section). Briefly, a precursor solution containing a copolymer of melamine, phenol and formaldehyde (nitrogen and carbon sources) and silica colloidal particles (pore templates) was atomized and passed a heating zone at 450 ºC. The resulted aerosol particles were collected and carbonized at 900 ºC for 3 hr. **Figure 5.1b** and **Figure 5.2** show representative transmission electron microscope (TEM) and scanning electron microscope (SEM) images of the NMC, indicating a porous spherical structure. These particles exhibit a size distribution mostly in the range of 200-600 nm in diameter, which is consistent with the size polydispersity of aerosol-based particles.[155] **Figure 5.3** shows the nitrogen adsorption and desorption isotherms and pore size distribution of the NMC, confirming a mesoporous structure with a pore diameter centered at around 15 nm. Such porous structure gives a high Brunauer-Emmett-Teller (BET) surface area of 843 m^2 g^{-1}. The nitrogen content of NMC is determined by energy dispersive x-ray spectroscopy (EDS) to be 7.01 wt% (**Figure 5.4**).

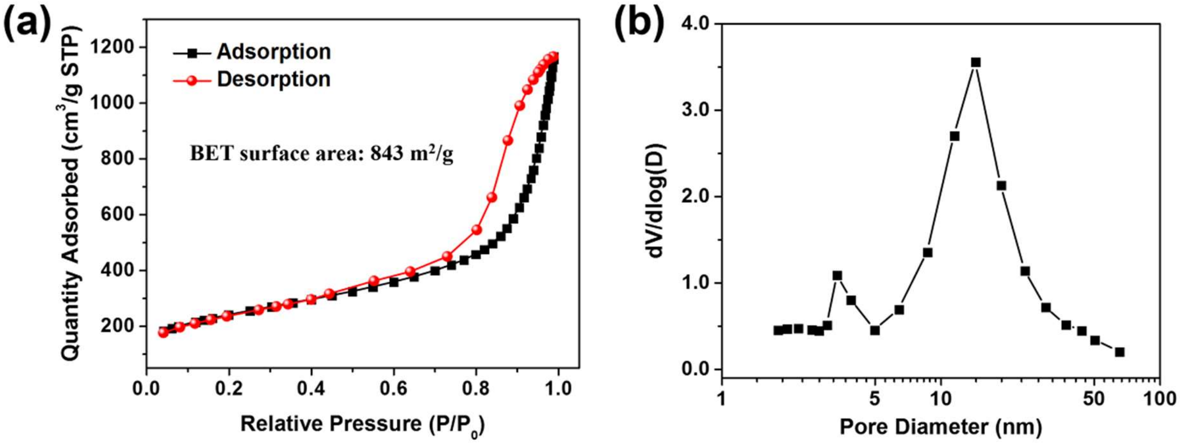

Figure 5.3. N_2 sorption isotherms (a), and pore size distribution (b) of NMC.

To synthesize the Fe/NMC catalysts, NMC was immersed in an ethyl ether solution of $Fe(CO)_5$; subsequent evaporation of the solvent at room temperature impregnates NMC with iron carbonyl. The impregnated NMC was then pyrolyzed at 800 °C for 1 h with a heating rate of 15 °C min^{-1} under N_2 to form the Fe/NMC catalysts. Three samples, namely Fe/NMC-1, Fe/NMC-11 and Fe/NMC-30, where 1, 11 and 30 refer to the atomic percentage of Fe in the ethyl ether solution, were prepared in this work; the Fe loading in the three catalysts determined by EDS is 1.11 wt%, 3.52 wt% and 4.45 wt%, respectively (**Figure 5.4**). All three catalysts were found to possess high nitrogen contents of ~10 wt% as determined by EDS, similar to that of NMC.

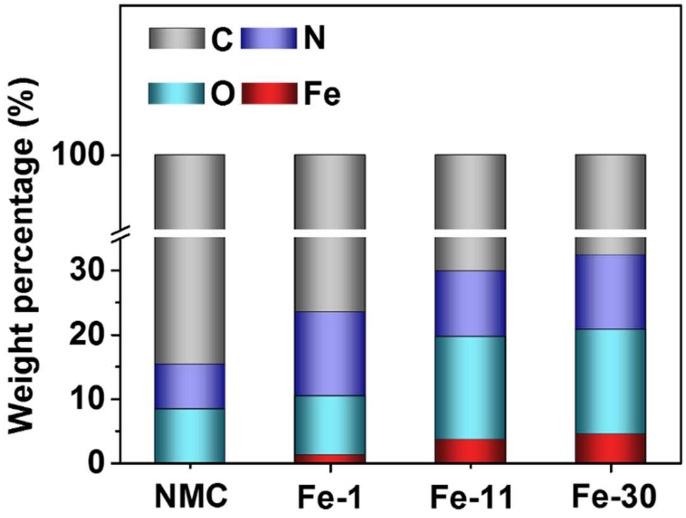

Figure 5.4. EDS elemental contents of NMC and three Fe/NMC catalysts.

Figure 5.1b-e compares the TEM images of the NMC and the resulted catalysts. The catalysts exhibit the spherical morphology with similar porous structure as that of NMC. No Fe particles are observed in Fe/NMC-1. With increasing Fe content, particles with several nanometers in diameter are observed in Fe/NMC-11. Further increasing the Fe content leads to the formation of larger size particles (~40 nm) in Fe/NMC-30. Consistently, Fe/NMC-30 exhibits the characteristic peaks of metallic iron (JCPDS 06-0696), whereas no Fe-related peaks are observed for Fe/NMC-1 and Fe/NMC-11 (**Figure 5.1f**). In addition, iron carbide is commonly observed in pyrolytically synthesized Fe-N-C catalysts,[56, 125, 148] nevertheless, no diffraction peak of iron carbide can be found in these samples. This is expected since the complicated reactions between the iron and carbon moieties in the traditional synthesis is avoided in this synthesis approach.[77, 156]

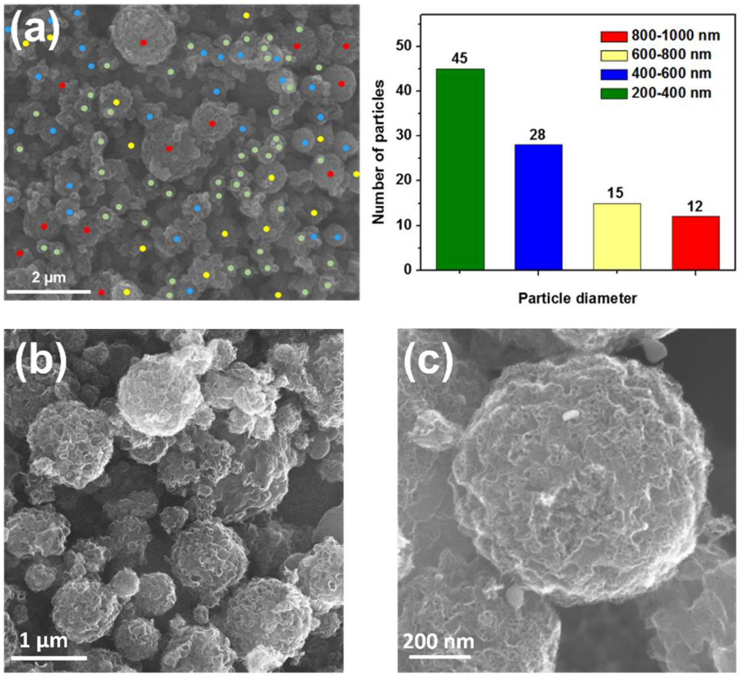

Figure 5.5. SEM image and particle size distribution, (b, c) SEM images at different magnifications of Fe/NMC-11.

Figure 5.5 shows the SEM images and size distribution of Fe/NMC-11, which resembles that of NMC, indicating the unaltered morphology of the catalyst after the second heat treatment. The pore structure of the catalysts was further investigated by N_2 sorption analysis. **Figure 5.1g** shows N_2 sorption isotherms and pore size distribution of Fe/NMC-11. The hysteresis loops indicate a mesoporous structure with a pore size distribution centered at around 15 nm, which is similar as that of NMC. The BET surface area of Fe/NMC-11 was found to be ~ 823 m^2 g^{-1}, which is also similar to that of NMC (843 m^2 g^{-1}). These results confirm the preservation of the porous structure of NMC after Fe doping.

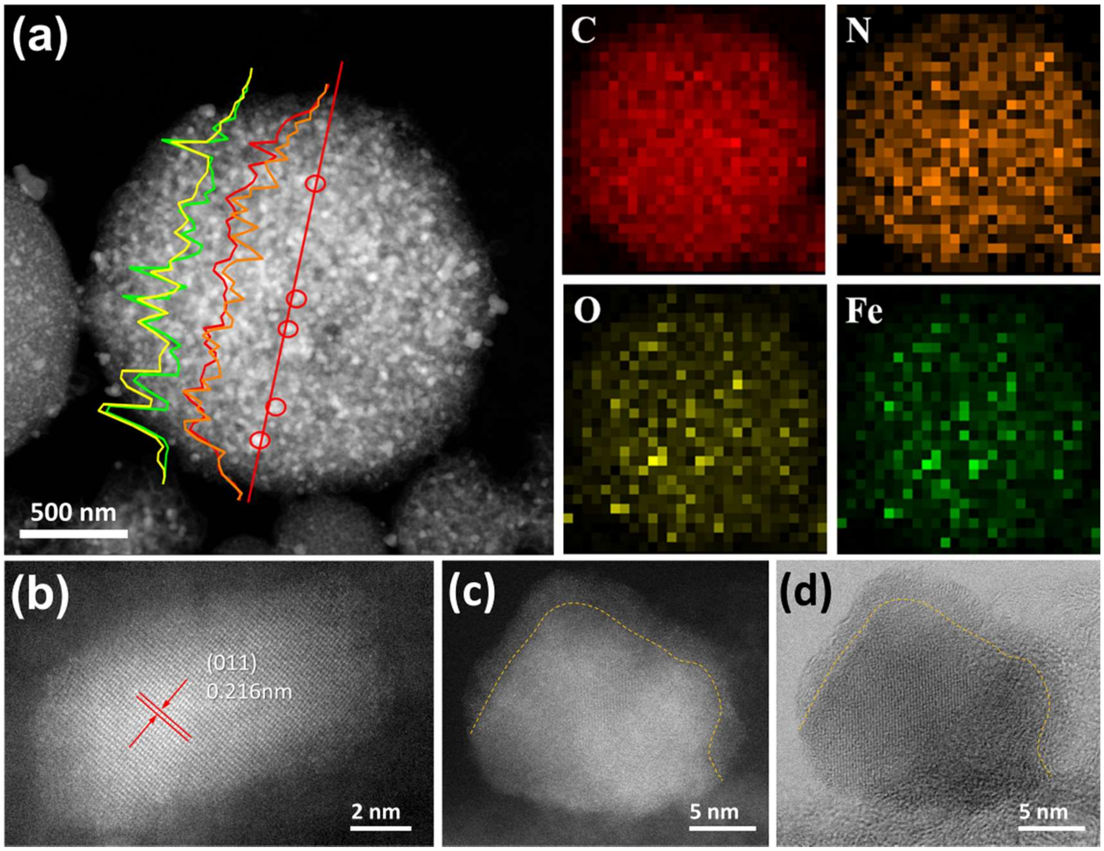

Figure 5.6. (a) HAADF-STEM image, elemental mapping and EDS linear scan spectrum of Fe/NMC-11. (b) HAADF-HRSTEM image of a typical Fe particle in Fe/NMC-11. (c) HAADF-HRSTEM image, and (d) ABF-HRSTEM image of another Fe particle in Fe/NMC-11.

To better study its composition and structure, we then obtained the high-angle annular dark field (HAADF) scanning transmission electron microscopy (STEM) image and the STEM-EDS mapping spectrum of a typical porous sphere of Fe/NMC-11. As illustrated in **Figure 5.6a**, all the four comprising elements are homogeneously distributed in the spherical particle. A number of bright particles in several nanometers evenly spread over the carbon structure, corresponding to the dark particles in the conventional TEM observation (**Figure 5.1d**). Notably, EDS linear scan spectra across the porous sphere of Fe/NMC-11 further show the evenly distributed C and N elements throughout the line, confirming the uniform and high-level doping of nitrogen in the carbon host. Although being generally uniform, the signals of Fe and O show some localized well-defined peaks. More careful examination reveals that their peak positions match with each other, and all correspond with the locations of the highlighted bright particles in the HAADF-STEM image. Such observation clearly indicates the correlation between the nanoparticles in Fe/NMC-11 and Fe, O elements, which was further proved by an aberration-corrected scanning transmission electron microscopy (AC-STEM). The HAADF-HRSTEM image of a typical nanoparticle (**Figure 5.6b**) reveals its well crystallized feature with a lattice distance of 0.216 nm, corresponding to the (011) plane of metallic iron (cubic, Im-3m). The surface of the crystallized nanoparticle, on the other hand, consists of a thin amorphous layer, which can be also seen in the HAADF and annular bright field (ABF) STEM images of another particle (**Figure 5.6c-d**). A closer look at the HAADF images reveals a number of atomic-scale bright dots in the amorphous surface layers of the particles, which should be attributed to heavy atoms of Fe. Therefore, it can be speculated that the nanoparticles in the Fe/NMC catalysts adopt a core-shell structure of surface oxidized crystalline metallic iron.

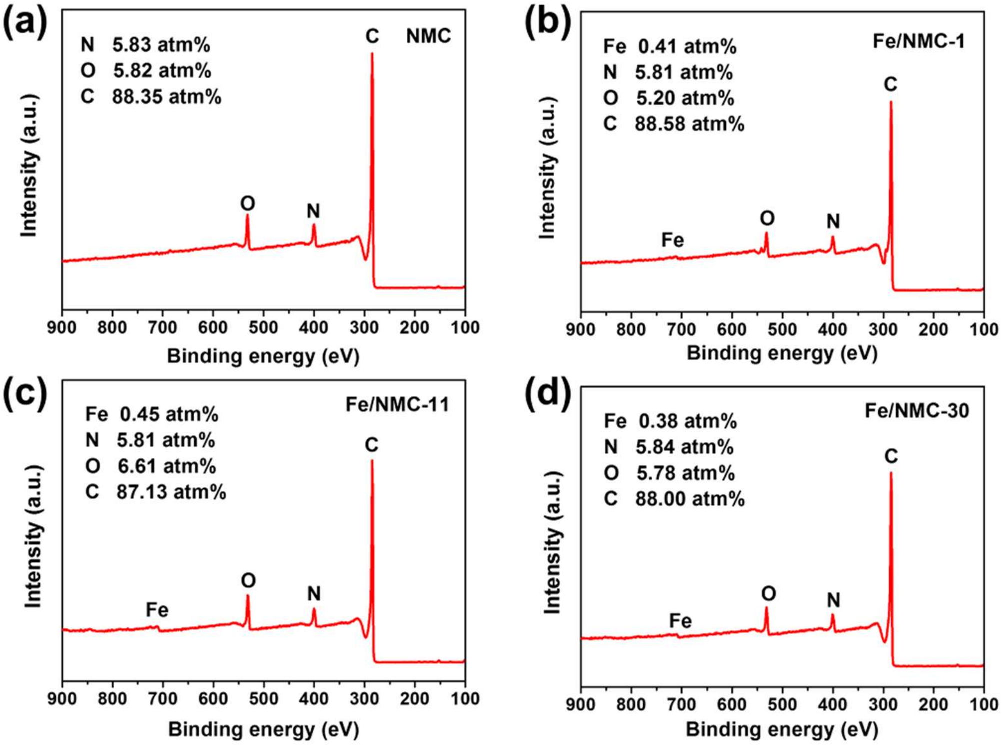

Figure 5.7. XPS survey scans of NMC, Fe/NMC-1, Fe/NMC-11 and Fe/NMC-30.

X-ray photoelectron spectroscopy (XPS) was then applied to study the surface composition of the catalysts, which is of special interest for electrocatalysis. The survey spectra of the three Fe/NMC catalysts confirmed the presence of C, N, O, and Fe elements (**Figure 5.7**). Of particular notice is the similar N contents in NMC and the three Fe/NMC catalysts, ranging from 5.81 at.% to 5.84 at.%, further indicating the preservation of nitrogen sites after the Fe decoration process. The high-resolution N 1s spectra of the samples (**Figure 5.8**) could be deconvoluted into two peaks corresponding to pyridinic N (398.4 eV) and graphitic N (400.8 eV). The former peak might also include a contribution from iron-bound nitrogen (N-Fe) from Fe-Nx moieties because of the small difference between binding energies of pyridinic N and N-Fe.[94, 148, 157] Furthermore, a closer examination of the N 1s spectra reveals that the area ratio of the two peaks are generally unchanged after decoration of Fe (**Figure 5.9**).

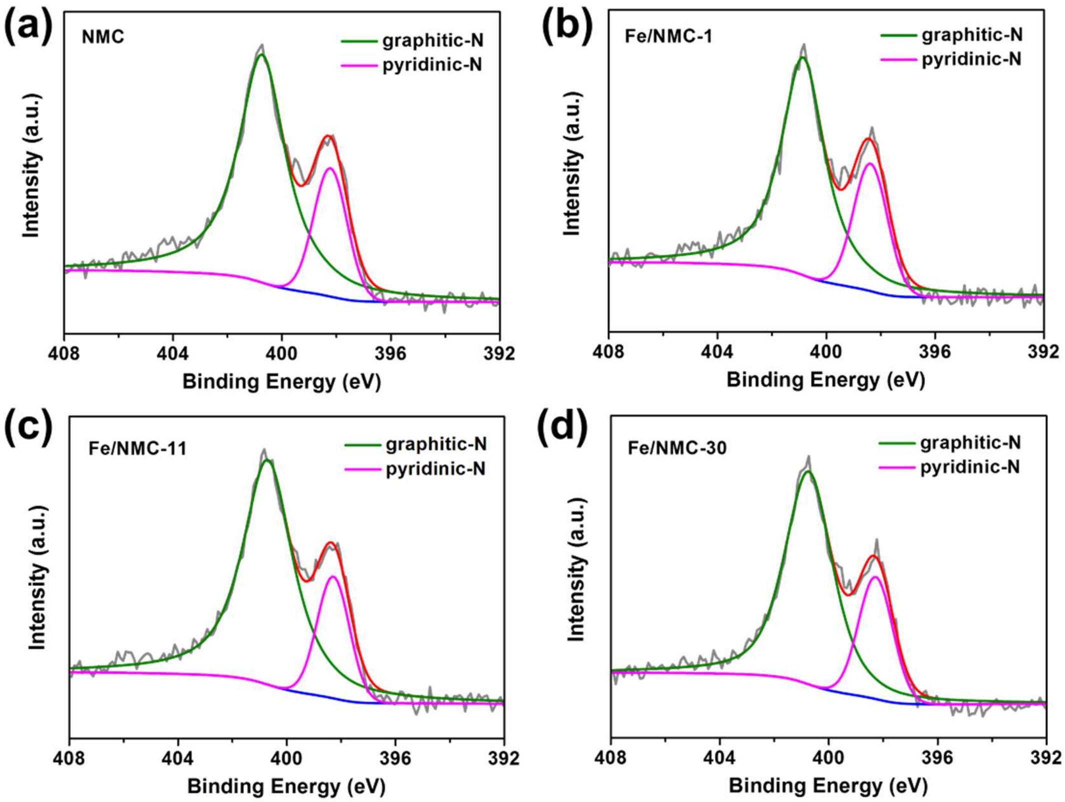

Figure 5.8. High resolution XPS N 1s spectra of NMC and three Fe/NMC catalysts.

The above results show that the nitrogen content is generally unaffected during the Fe decoration process. If noncrystalline Fe-N_x moieties exist in the Fe/NMC catalysts, which is very likely as discussed shortly, they should be constructed from pyridinic N. Meanwhile, the graphitic N of NMC, which is reported to be the most active type of nitrogen for ORR, remain intact after the incorporation of Fe.[90, 91, 116, 158] These results together demonstrate the advantage of our synthetic strategy, which leaves the catalysts with desired nitrogen doping. High-resolution XPS Fe 2p spectra of the samples were also recorded to explore the surface state of the Fe atoms (**Figure 5.10**). No zero-valence Fe was detected for any Fe/NMC catalyst, which confirms the STEM result that the surface of the Fe particles are oxidized. The signals at around 710 eV in the Fe $2p_{3/2}$ spectra of the three Fe/NMC catalysts should include the contribution from both Fe-O_x from the surface of Fe particles, and Fe-N_x.[56, 98, 159]

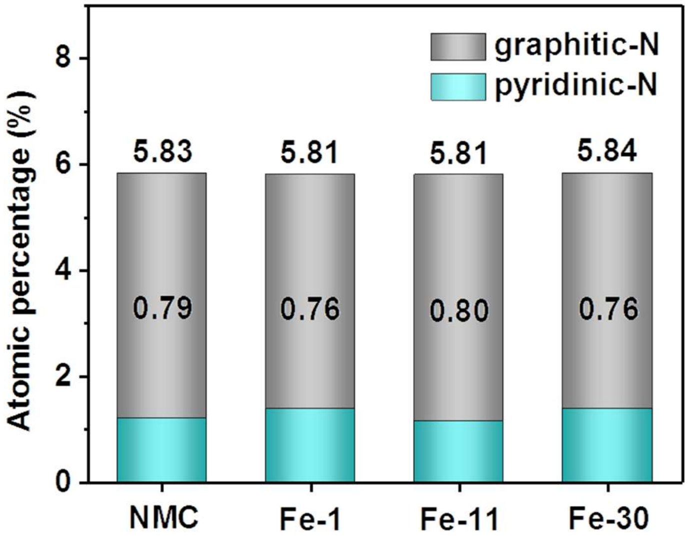

Figure 5.9. XPS nitrogen contents of NMC and three Fe/NMC catalysts (numbers on the grey cylinders denotes the ratio of graphitic-N to total N contents in each catalyst).

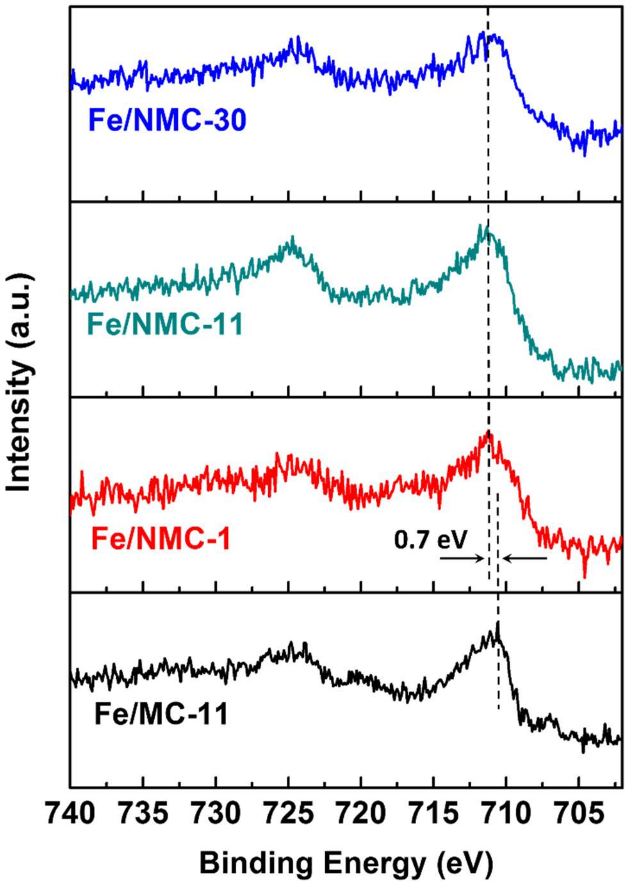

Figure 5.10. High resolution XPS Fe 2p spectra of Fe/MC-11 and three Fe/NMC catalysts.

The ORR activities of the Fe/NMC catalysts were assessed using rotating disk electrode (RDE) technique in O_2-saturated 0.1 M NaOH. The linear sweep voltammetry (LSV) tests were first performed on Fe/NMC-11, NMC, nitrogen-free mesoporous carbon spheres (MC) and a commercial Pt/C catalyst (40% Pt/C, JM). The MC was prepared from a similar precursor but without melamine as nitrogen source. As shown in **Figure 5.11**a, MC exhibits the lowest ORR performance with a half-wave potential ($E_{1/2}$) of 0.777 V (vs. reversible hydrogen electrode (RHE)), owing to the limited catalytic activity of the pristine carbon. After nitrogen doping, the NMC shows an enhanced activity in terms of an $E_{1/2}$ at 0.801 V, due to formation of C-N_x active sites.[91, 116] After incorporation of Fe, the catalytic performance of Fe/NMC-11 dramatically improves with a high $E_{1/2}$ of 0.862 V, which is closely comparable to that of Pt/C catalyst (0.872 V) and is among the best activity for iron based catalysts reported recently (**Table 5.1**). Considering the generally unaltered N-doped carbon structure, the improved ORR performance of the Fe/NMC-11 catalyst can be safely attributed to the incorporation of Fe-containing moieties.

Table 5.1. Comparison of $E_{1/2}$ for Fe-based catalysts in alkaline media.

Catalysts	**Loading (mg cm^{-2})**	**$E_{1/2}$ vs RHE (V)**	**Reference**
Fe/NMC-11	0.51	0.862	This work
Fe-N_x/C	0.1	0.837	*J. AM. Chem. Soc.* **2013**, *135*, 15443
Fe_3C@NG-800-0.2	0.2	0.83	*ACS appl. Mater. Interface* **2015**, *7*, 21511
S,N-Fe/N/C-CNT	0.6	0.85	*Angew. Chem. Int. Ed.* **2016**, *55*, 1
Fe/N/C HNSs-750	0.255	0.8	*Nanoscale* **2015**, *7*, 1501
Fe_3C/C-800	0.6	0.86	*Angew. Chem. Int. Ed.* **2014**, *53*, 3675
Fe/N-gCB	0.2	0.82	*Chem. Commun.* **2015**, *51,* 7516
FePhen@MOF-ArNH$_3$	0.6	0.86	*Nat. Commun.* **2015**, *6*, 7343
BCNFNHs	1.2	0.861	*J. AM. Chem. Soc.* **2015**, *137*, 1436

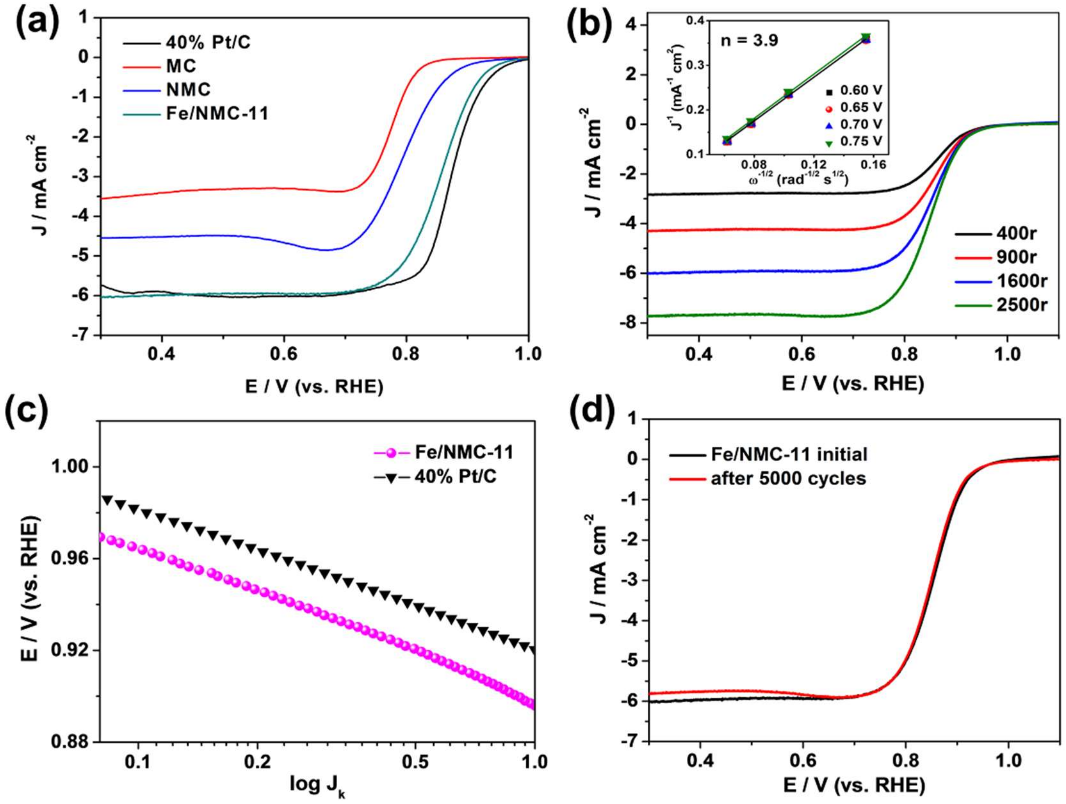

Figure 5.11. (a) LSV curves of all the samples at 1600 rpm; (b) LSV curves of Fe/NMC-11 at various rotation rates. The inset shows the corresponding K-L plots of Fe/NMC-11 at different potentials. (c) Tafel plots of Fe/NMC-11 and 40% Pt/C; (d) LSV curves of Fe/NMC-11 before and after 5000 potential cycles. All the electrochemical tests above are carried out in O_2 saturated 0.1 M NaOH.

RDE measurements were further carried out to reveal the ORR kinetics of Fe/NMC-11. The linear and parallel Koutecky-Levich (K-L) plots suggest a first-order reaction toward the concentration of dissolved oxygen and similar electron transfer numbers for ORR at different potentials (inset of **Figure 5.11b**).[134] The electron transfer number (n) was calculated to be ~ 3.9 from 0.60 to 0.75 V on the basis of the K-L equations, indicating a dominant 4 electron transfer process.[160] Moreover, the kinetic current (j_K) derived from the mass transport correction of the ORR currents shows a Tafel slope of 67 mV dec^{-1}, close to the 62 mV dec^{-1} for Pt/C (**Figure 5.11c**). Therefore, similar to ORR catalyzed by platinum, transfer of the first electron catalyzed by Fe/NMC-11 is probably the rate-limiting step.[161]

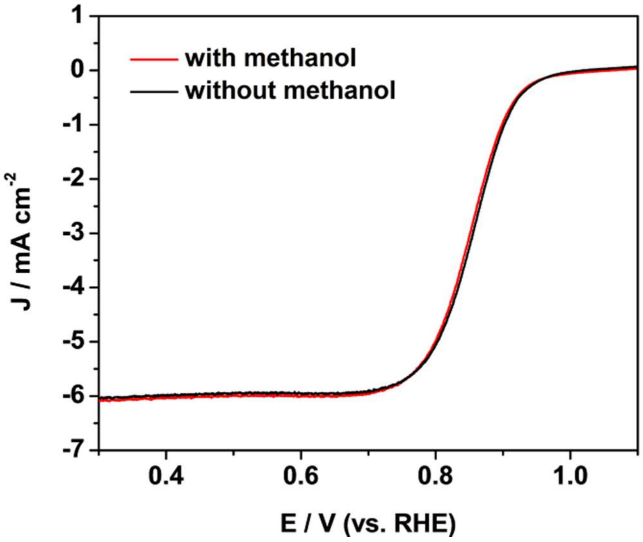

Figure 5.12. LSV curves of Fe/NMC-11 in O_2 saturated 0.1 M NaOH with and without 1.0 M CH3OH.

The durability of Fe/NMC-11 was evaluated using an accelerated durability test protocol.[48] As shown in **Figure 5.11d**, the catalyst exhibits extraordinary stability as the LSV curve was almost unchanged after 5000 potential cycles, which is among the best reported stability of Fe-N-C catalysts.[48, 56, 94] Methanol tolerance of the Fe/NMC-11 catalysts was further evaluated by comparing the LSVs for the catalyst in both oxygen saturated 0.1 M NaOH and 0.1 M NaOH + 1 M methanol solutions. As shown in **Figure 5.12**, no obvious change of the LSV curve is seen after an injection of methanol, demonstrating the excellent methanol tolerance of Fe/NMC-11.

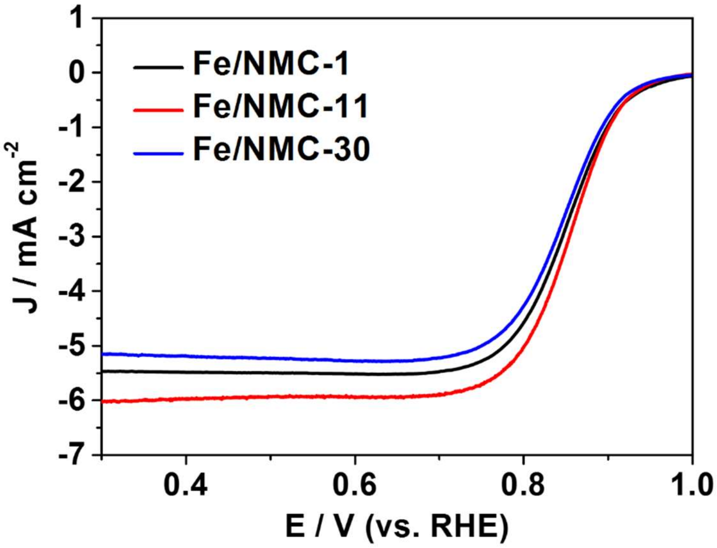

Figure 5.13. LSV curves of three Fe/NMC catalysts.

The above results demonstrate the successful synthesis of highly active Fe-N-C catalysts by reacting preformed NMC with Fe(CO)$_5$. NMC not only serves as a preformed carbon scaffold with controlled structure and high surface area, but also provides abundant N-doping sites to anchor the Fe moieties. The pyridinic N within the NMC may attack the Fe(CO)$_5$ through a Lewis acid-base reaction forming active Fe-N$_x$ sites,[162] while graphitic N, which is relatively weaker binding ability but is regarded as the most active type of nitrogen for ORR, is well preserved during the pyrolysis.[63] With a low Fe(CO)$_5$ loading (e.g., Fe/NMC-1), most the Fe moiety forms the Fe-N$_x$ sites. With increasing Fe(CO)$_5$ loading (e.g., Fe/NMC-11), besides the formation of Fe-N$_x$ sites, noticeably increased amount of crystalline Fe nanoparticles is also formed. Further increasing the amount of Fe(CO)$_5$ used (e.g., Fe/NMC-30) leads to the formation of larger crystalline Fe particles, which might block the active sites in the catalyst, leading to inferior activity. Consistently, the highest ORR activity was achieved by Fe/NMC-11, probably due to the optimized content of Fe-Nx site and ultrasmall Fe nanocrystallites (**Figure 5.13**).

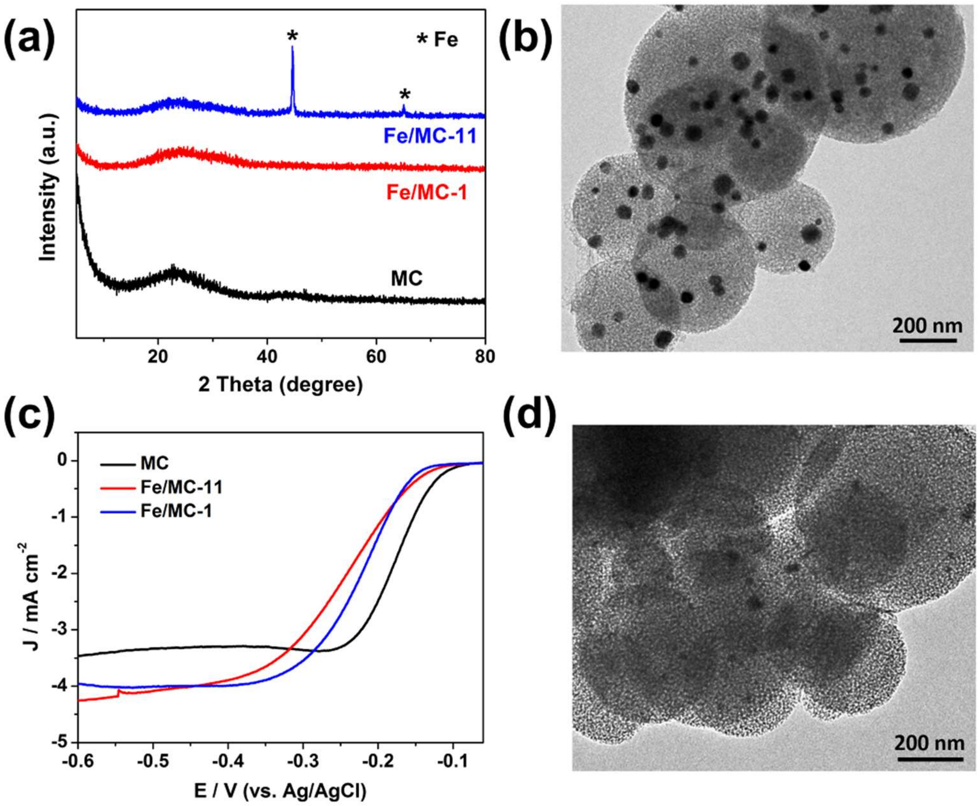

Figure 5.14. (a) XRD patterns of MC, Fe/MC-1 and Fe/MC-11. (b) TEM image of Fe/MC-11. (c) LSV curves of MC, Fe/MC-1 and Fe/MC-11. (d) TEM image Fe/MC-1.

To verify the essential role of the nitrogen-containing sites in preformed carbon scaffolds, Fe/MC-11 catalyst without nitrogen doping was synthesized using a nitrogen-free carbon spheres MC following the same procedure of preparing Fe/NMC-11. Similar to Fe/NMC-11, no zero-valence Fe is detected in Fe/MC-11 in the XPS study (**Figure 5.10**). It is also notable that the Fe $2p_{3/2}$ peak position of Fe/MC-11 is 0.7 eV lower than that of Fe/NMC-11 (711.30 to 710.59 eV).

This shift can be explained by the different charge density of the Fe atoms in Fe-N_x and Fe-O_x structures.[66, 163] A sharp peak of metallic Fe appears in the XRD pattern of Fe/MC-11, in line with Fe nanoparticles of around 50 nm in diameter observed in the TEM image (**Figure 5.14a and b**), which are notably larger than those in Fe/NMC-11. Therefore, the N atoms with high affinity to Fe might also serve as nucleation sites for crystalline Fe nanoparticles and prevent their excessive growth into larger sizes.[56] We further extended this synthetic strategy to other metal carbonyls and successfully prepared Me/NMC (Me=W, Mo, Mn) composites with uniform distribution of metal particles (**Figure 5.15, Figure 5.16**), providing a general approach towards a new family of catalysts.

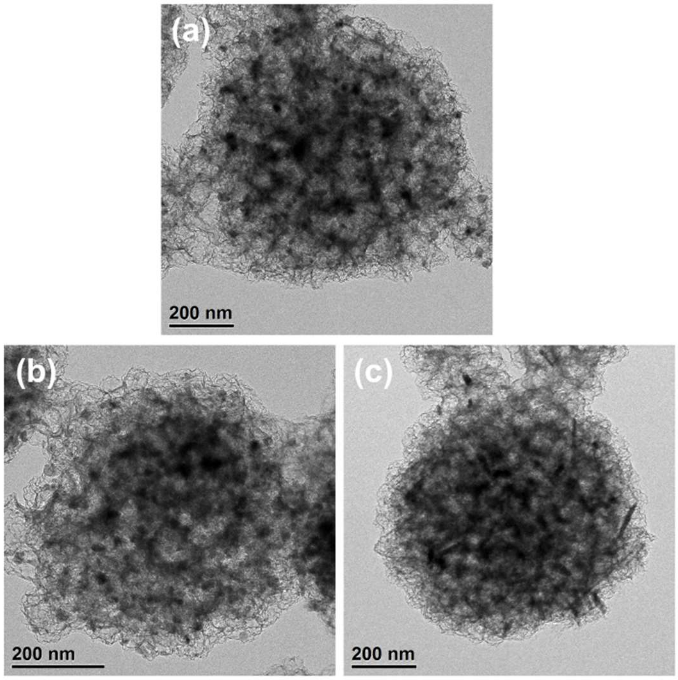

Figure 5.15. TEM images of (a) Mn/NMC, (b) Mo/NMC and (c) W/NMC.

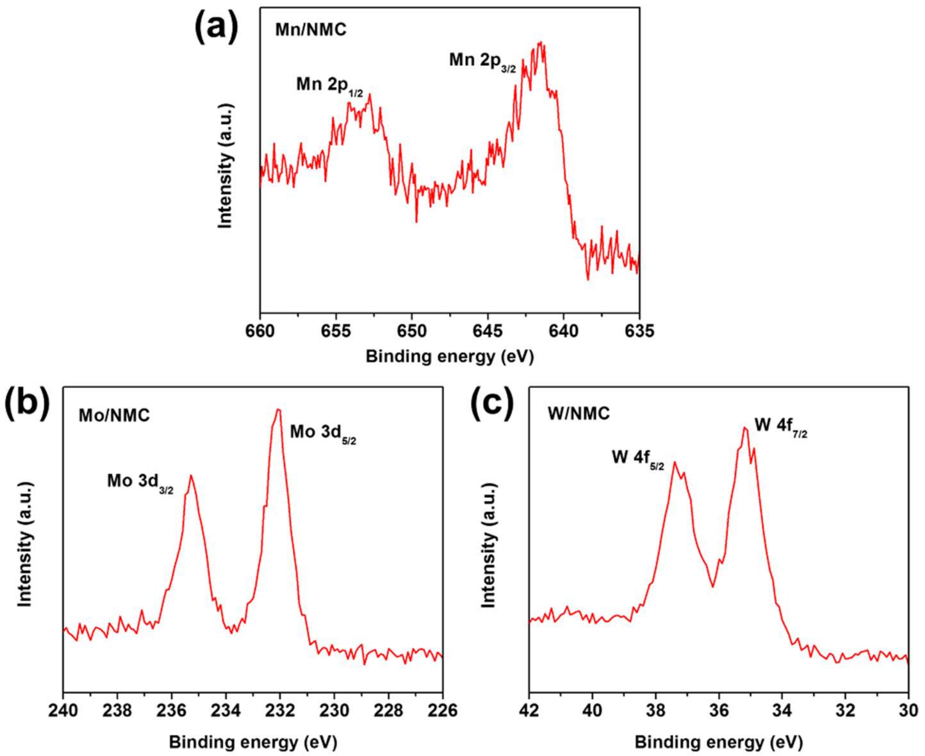

Figure 5.16. (a) XPS Mn 2p spectrum of Mn/NMC, (b) XPS Mo 3d spectrum of Mo/NMC and (c) XPS W 4f spectrum of W/NMC.

In addition, it has been observed that Fe nanoparticles may also exhibit ORR catalytic activity.[164] To differentiate their contribution from that of Fe-N_x moieties, Fe/NMC-11 was washed with 0.5 M H_2SO4 to remove the Fe nanoparticles (**Figure 5.17**). The resultant sample (denoted as Fe/NMC-11w) exhibits a lower $E_{1/2}$ of 0.837 V than that of Fe/NMC-11 (0.862 V), but still notably higher than that of NMC (0.801 V) as shown in **Figure 5.18**. Thus, the Fe-N_x moieties are considered as the major active centers catalyzing the ORR. To verify this observation, we further decorated NMC with Fe nanoparticles without creating Fe-N_x sites (**Figure 5.19a-b**).

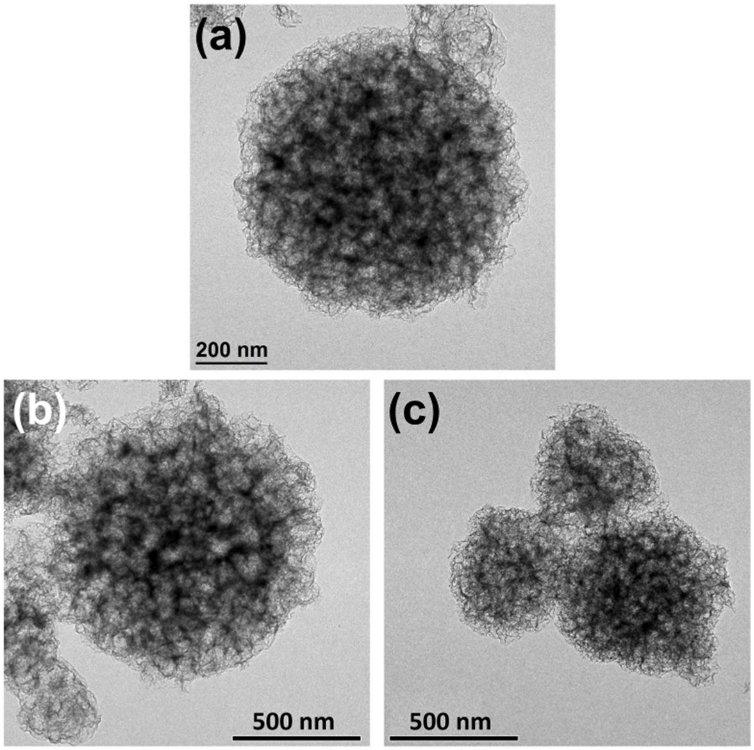

Figure 5.17. TEM images at different magnifications of Fe/NMC-11w.

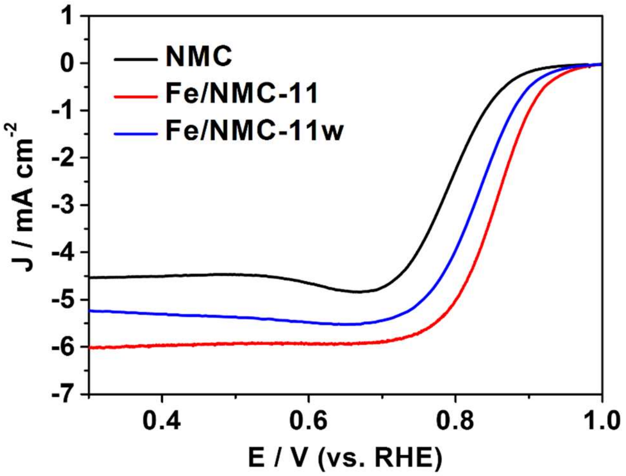

Figure 5.18. LSV curves of NMC, Fe/NMC-11 and Fe/NMC-11w.

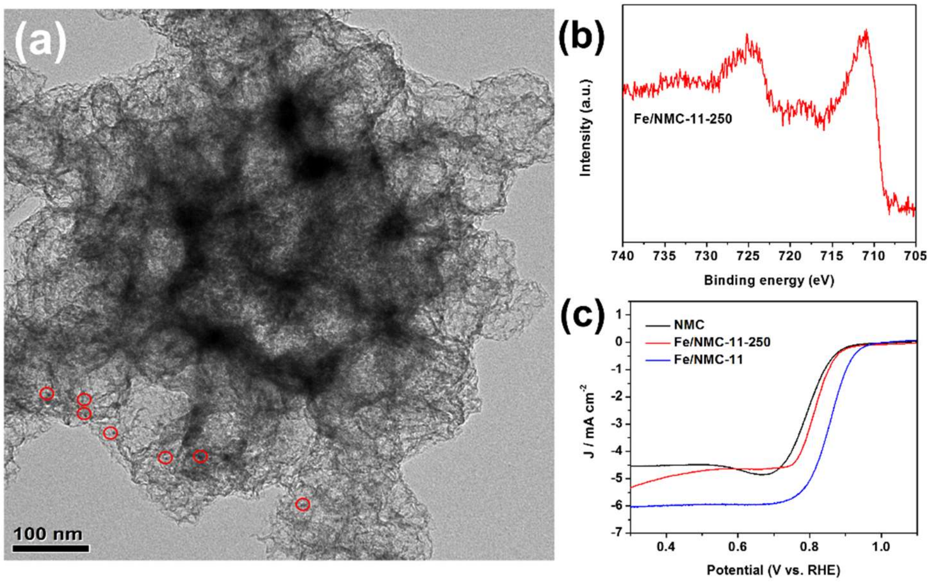

Figure 5.19. (a) TEM image, (b) XPS Fe 2p spectrum of Fe/NMC-11-250, (c) LSV curves of NMC, Fe/NMC-11-250 and Fe/NMC-11. The Fe/NMC-11-250 catalyst was prepared using the same procedure as for Fe/NMC-11 except for a lower pyrolysis temperature of 250 ^{o}C. Such low temperature would allow the decomposition of $Fe(CO)_5$ into Fe nanoparticles with surface oxidation without forming Fe-N_x sites.

However, the ORR activity of the resultant material is only slightly better than that of NMC, verifying the role of Fe-N_x moieties as major active sites in Fe/NMC catalysts (**Figure 5.19c**). While the surface-oxidized Fe nanoparticles do contribute to the high ORR activity, these nanoparticles alone show insufficient catalytic activity as suggested by the inferior performance of Fe/MC-11 (**Figure 5.14c**), though crystalline iron oxide particles have been reported to be ORR active.[165] In addition, Fe/MC-11 shows a more negative half-wave potential, yet an increased current density in the diffusion-limited potential region compared with MC, suggesting an increased electron transfer number. Similar phenomenon is also observed in Fe/MC-1 with smaller size of Fe nanoparticles (**Figure 5.14a, d**). These observations indicate that the Fe nanoparticles, though inactive for ORR at higher potential, could reduce HO_2^- (product of the 2-e^- reduction of oxygen) and thus facilitate the 4-e^- ORR process.[70]

5.4 Conclusion

In summary, we have demonstrated a novel synthesis strategy for high-performance Fe-N-C electrocatalysts by reacting preformed N-doped carbons with iron pentacarbonyl. This simple strategy separates the synthesis of N-doped carbon from the formation of active Fe-N_x sites, providing an effective approach to synthesize better Fe-N-C electrocatalysts with controlled pore structure, surface area, doping condition, and active sites. As formed catalysts exhibit outstanding ORR activity (closely comparable to 40% Pt/C) and stability in alkaline media, as well as good methanol tolerance. The synthetic strategy is also successfully extended to prepare other metal-N-C composites. Considering the versatility of surface chemistry, we believe that our synthetic protocol opens a new avenue for designing metal-N-C catalysts and other surface-functionalized materials for various applications.

Chapter 6. Iron Decorated Hierarchically Porous Nitrogen-Rich Carbon as Efficient Electrocatalysts for Oxygen Reduction Reaction in Zn-Air Battery

6.1 Introduction

Metal-air batteries are promising electrochemical device for energy conversion owing to their high energy density and environmental friendliness. However, their performance has been limited by the sluggish oxygen reduction reaction (ORR) at the air cathodes.[36, 135, 166] Although Pt-based catalysts show high catalytic activity towards ORR, the scarcity and high cost prevent their large-scale applications. Thus, developing non-Pt ORR catalysts appears the ultimate solution to broaden the use of metal-air batteries.[37, 52, 167-169]

During the past decade, a wide variety of materials have been studied as non-Pt ORR catalysts.[48, 51, 73, 87, 93, 116, 134, 148, 170-172] Among them, "iron-nitrogen-carbon (Fe-N-C)" catalysts, which are typically prepared by pyrolyzing Fe, N, C-containing precursors exhibit the most promising activity.[36, 37, 63] However, though Fe-N_x moieties are generally accepted as the major active site, the function of Fe/Fe_3C nanoparticles in Fe-N-C catalysts has been debated. While some works report severe reduction in the catalysts activity upon the presence of Fe/Fe_3C nanoparticles, other studies show that these nanoparticles may increase the activity of Fe-N_x through electronic interaction or act as alternative active sites.[50, 56, 70, 71, 173]

Besides explaining the nature of active sites, the development of a low-cost and scalable method for preparing Fe-N-C catalysts with high device performance still remains a challenge.[11, 174] In order to deliver high device performance, it is essential for the catalysts to possess high active site density, large surface area, and desired porous structure.[93, 94] However, achieving these properties in Fe-N-C catalysts often requires using costly organometallic compounds and solid template, post treatment of the material and careful manipulation of the preparation conditions, compromising the economy and scalability of the synthesis methods.[36, 59, 175, 176]

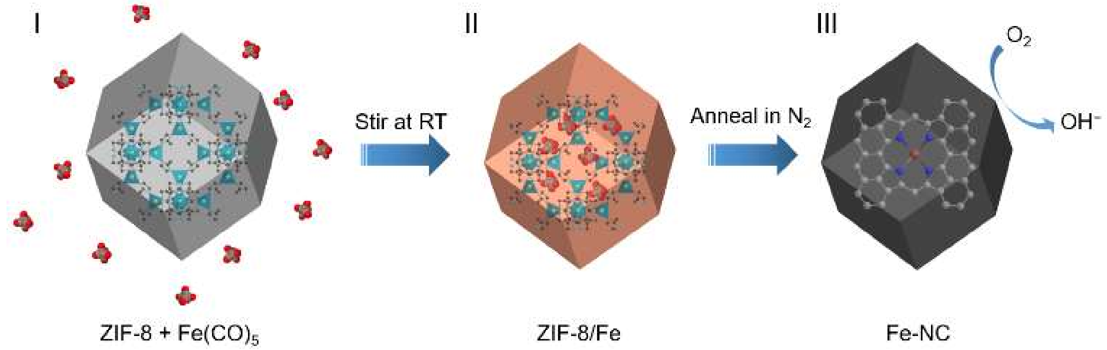

Scheme 6.1. Schematic illustration of the synthesis of Fe-NC catalysts. (I) ZIF-8 nanocrystals (grey polyhedron; the crystal structure of ZIF-8 is superimposed) dispersed in $Fe(CO)_5$ (surrounding molecules). (II) ZIF-8/Fe precursor (orange polyhedron) with $Fe(CO)_5$ confined in the porous framework (shown in the superimposed image). (III) Fe-NC catalyst particles (black polyhedron) with rich micropores (possible structures of Fe-containing moieties are superimposed; brown: iron; grey: carbon; blue: nitrogen).

Herein, we demonstrate a novel and general approach to synthesize Fe-N-C electrocatalysts with abundant active sites and hierarchically porous structure based on the pyrolysis of Metal-Organic Frameworks (MOFs)-iron carbonyl ($Fe(CO)_5$) complex. As shown in **Scheme 6.1**, nanocrystals of a N-rich MOF (ZIF-8) are used as a porous host to adsorb and immobilize iron carbonyl at ambient temperature. Fe-NC catalysts are then obtained by directly pyrolyzing the iron carbonyl decorated ZIF-8 (ZIF-8/Fe). During the pyrolysis, $Fe(CO)_5$ reacts homogeneously with the ZIF-8 scaffold, leading to the uniform distribution of Fe-related active sites on the N-rich porous carbon derived from ZIF-8. While the in-situ generated hierarchically porous structure could host the active sites by micropores and promote charge/mass transport by meso-/macropores, providing a large amount of easily accessible ORR active sites.[94] In virtue of these advantageous features, the optimized Fe-NC catalyst exhibits excellent ORR activity with a half-wave potential of 0.91 V (vs. reversible hydrogen electrode, RHE), exceeding that of the benchmark 40% Pt/C catalyst. Furthermore, the zinc-air battery constructed with our Fe-NC catalyst at cathode, exhibits high open-circuit voltage (1.5 V) and peak power density (271 mW cm^{-2}), which outperforms that of most non-precious metal catalysts (NPMCs) reported so far.

Note that MOFs have been used as precursors for various electrochemically active materials,[177-180] including ORR catalysts. For example, N-doped carbons with Co-based moieties have been prepared by pyrolyzing Co based MOFs (e.g., ZIF-67 and ZIF-9).[124, 172, 181, 182] However, using MOFs as a single precursor for M-N-C catalysts provides quite limited capability to control the composition. Thus, in several studies aiming to synthesize Fe-N-C catalysts using MOFs, additional Fe salts and costly N-containing chelating compounds are indispensable. Such components were generally mixed and reacted with bulky MOF particles, which increase the cost and likely cause inhomogeneity in the catalysts.[39, 63, 183] Alternatively, partially replacing the pristine metal centers in MOFs (e.g., Fe-doped ZIF-8) offers a limited capability to manipulate the composition of MOF precursors.[184, 185] In a sharp contrast, the approach developed in this work is cost-effective and easily scalable. Moreover, tuning the metal centers of the catalyst could be easily achieved by incorporating other metal carbonyls, offering the possibility to further enhance the catalytic activity and durability.

6.2 Experimental

Synthesis of ZIF-8 nanocrystals

ZIF-8 nanocrystals are synthesized by using a simple and scalable co-precipitation method at ambient temperature. In a typical synthesis, 1.47 g of $Zn(NO_3)_2 \cdot 6H_2O$ was dissolved in 100 mL of methanol. Another solution was prepared by dissolving 1.62 g of 2-methylimidazole in 100 mL of methanol. The later solution was poured into the former one under magnetic stirring, and the stirring was stopped after the two solutions were well mixed. After remaining static for one day at ambient temperature, the white precipitates were collected by centrifugation, washed with methanol and then dried at 80 ^{o}C in a vacuum oven over night.

Synthesis of ZIF-8/Fe

To load iron into ZIF-8 nanocrystals, 500 mg of as-prepared ZIF-8 powder was dispersed in 4 mL of iron carbonyl ($Fe(CO)_5$) under magnetic stirring in a seal glass vial at ambient temperature. After stirring for 4 h, the solid product was collected by filtration and rinsed with ethanol to remove the excess iron carbonyl. The product was finally rinsed with acetone and dried at ambient temperature. Controlled experiments were also performed by extending the stirring time to 8 and 12 h.

Synthesis of Fe-NC catalysts

The as-prepared ZIF-8/Fe was annealed in a tube furnace under N_2 at 800, 900, and 1000 ^oC for 4 h with a heating rate of 10 ^oC min^{-1}. The resulting powder was milled using a SPEX 5100 mix mill for 20 min to break down the aggregated particles. NC-900 sample was directly prepared from ZIF-8 nanocrystals at 900 ^oC without Fe source for comparison.

Synthesis of other M-NC catalysts

To synthesize M-NC catalysts containing other transition metals, 100 mg of corresponding solid metal carbonyls ($Mn_2(CO)_{10}$, $Co_2(CO)_8$, $Mo(CO)_6$, $W(CO)_6$) are dissolved in an appropriate amount of diethyl ether. And then 200 mg of ZIF-8 nanocrystals was added into the above solution. After stirring at ambient temperature for 16 h, the product was collected by filtration and rinsed by diethyl ether. The as-obtained precursor was subjected to the same heat treatment at 900 ^oC for 4 h in nitrogen.

Characterizations

Powder X-ray diffraction was operated on a Rigaku MiniFlex II (Rigaku, Japan) using Cu Kα radiation (λ=0.15406 nm). Nitrogen-sorption isotherms were measured at 77 K with a

Micromeritics ASAP 2020 analyzer (Micromeritics Instrument Corporation, Norcross, GA). Specific surface areas were calculated by the Brunauer-Emmett-Teller (BET) method and the micropore surface areas were obtained by the t-plot method. Morphology and structure of the samples were characterized by scanning electron microscope (SEM, FEI Nova NanoSEM) and transmission electron microscope (TEM, FEI T12, 120 kV; FEI Titan). Elemental composition was analyzed by energy-dispersive X-ray spectroscopy (EDS) attached on SEM. X-ray photoelectron spectroscopy (XPS) tests were performed with Kratos AXIS Ultra DLD spectrometer with a monochromatic Al K α (1486.6 eV) source. Thermogravimetric analysis (TGA) and differential scanning calorimetry (DSC) was conducted on a TA Instruments SDT-Q600 under N_2 flow with a heating rate of 10 °C min^{-1}.

Electrochemical measurements

All electrocatalytic measurements are carried out in a three-electrode cell using a rotating ring-disk electrode (RRDE) or rotating disk electrode (RDE) from PINE Research Instrumentation, with a Bio Logic VMP3 (Bio Logic Science Instruments) and a WaveDriver 20 (PINE Research Instrumentation) electrochemical workstations at ambient temperature. A graphite rod and a Ag/AgCl (saturated KCl) were used as the counter and reference electrodes, respectively. A glassy carbon (GC) electrode was used as the substrate for the working electrode. To prepare the working electrode, 5 mg of the catalyst was dispersed in 2 mL of ethanol and 30 uL of 5 wt% Nafion solution by ultrasonication. A certain volume of the suspension was pipetted on the GC surface and dried at ambient temperature. RDE and RRDE measurements for ORR were perform in O_2

saturated 0.1 M NaOH as electrolyte with a scan rate of 10 mV s^{-1}. The polarization curves were recorded using positive scan, and corrected with background current and iR loss. Background current was scanned in N_2 saturated 0.1 M NaOH. Solution resistance determined by the high frequency intercept in the Nyquist plot from electrochemical impedance spectrum and used for iR correction. Onset potential is defined as the potential to reach a current density of 0.1 mA cm^{-2}.

Potentials in this study refer to reversible hydrogen electrode (RHE). The reference electrode was calibrated by conducting cyclic voltammetry (CV) scan with Pt/C on GC as working electrode in H_2 saturated 0.1 M NaOH. The potential where current crossed zero was the thermodynamic potential for the hydrogen electrode reaction. In 0.1 M NaOH, E(RHE) = E(Ag/AgCl) + 0.942 V. Stability of the catalysts were evaluated by conducting CV scans between 0.6-1 V vs. RHE at 100 mV s^{-1} in O_2 saturated electrolyte for 5000 cycles.

In the RRDE measurements, the ring potential was kept constant at 1.5 V vs. RHE. The electron transfer number (n) per oxygen molecule were calculated by the following equation:

$$n = 4 * I_d / (I_d + I_r / N) \tag{1}$$

where I_d, I_r and N are disk current, ring current and current collection efficiency of the Pt ring respectively. N was determined to be 0.4.

Zinc-Air battery tests were performed on home-built electrochemical cells. Specifically, Zn foil and 6 M KOH are employed as anode and electrolyte respectively. Certain amount of the catalysts and Nafion solution (Sigma Aldrich, 5 wt%) were dispersed in ethanol and sonicated for 60 min to form a homogeneous ink. The catalyst ink was then sprayed onto carbon paper, and the catalyst loaded carbon paper (catalyst loading: 1 mg cm^{-2}) were then used as the air cathode in Zn-air battery.

6.3 Results and Discussion

Uniform ZIF-8 nanocrystals with size of around 80 nm (**Figure 6.1**) were first synthesized by a simple and scalable co-precipitation method.[186] After thoroughly removing the solvent, ZIF-8 nanocrystals were directly dispersed in iron carbonyl, a light-orange-colored liquid. After stirring for 4 h, the resulting iron carbonyl decorated ZIF-8 (ZIF-8/Fe) well retains the crystal structure of the pristine ZIF-8 without any visible impurity from the powder X-ray diffraction (XRD) patterns (**Figure 6.2a**). However, an obvious change in color, from white of ZIF-8 to light brown of ZIF-8/Fe was observed (insets of **Figure 6.2a**). The successful incorporation of Fe in ZIF-8/Fe is further verified by energy-dispersive X-ray spectroscopy (EDS) analysis (**Figure 6.3**). Additionally, transmission electron microsope (TEM) images of the ZIF-8/Fe reveals the well preserved polyhedral morphology of ZIF-8 with a rougher surface (**Figure 6.4**). On the basis of the above observation, we conclude that iron carbonyl would be mostly adsorbed by the porous structure of ZIF-8. Due to the strong interaction between these two components, the highly volatile and reactive iron carbonyl could be stabilized and participate in the formation of active sites upon heating.[162]

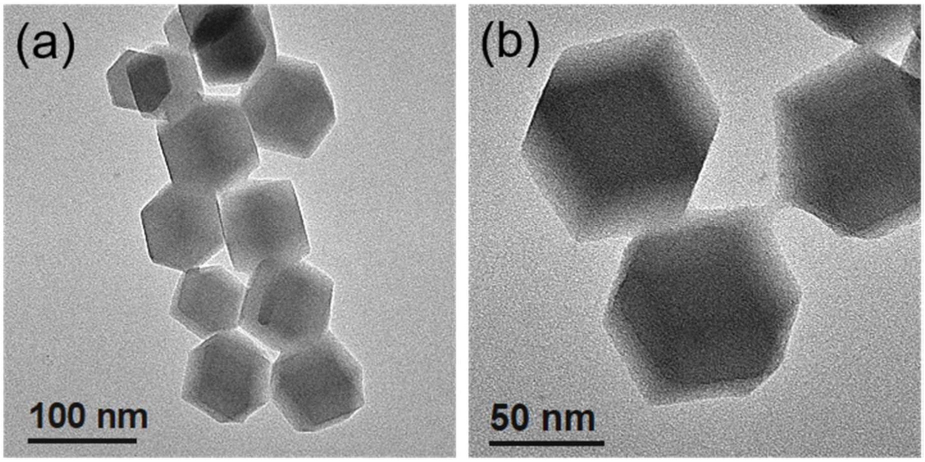

Figure 6.1. TEM images of ZIF-8 nanocrystals.

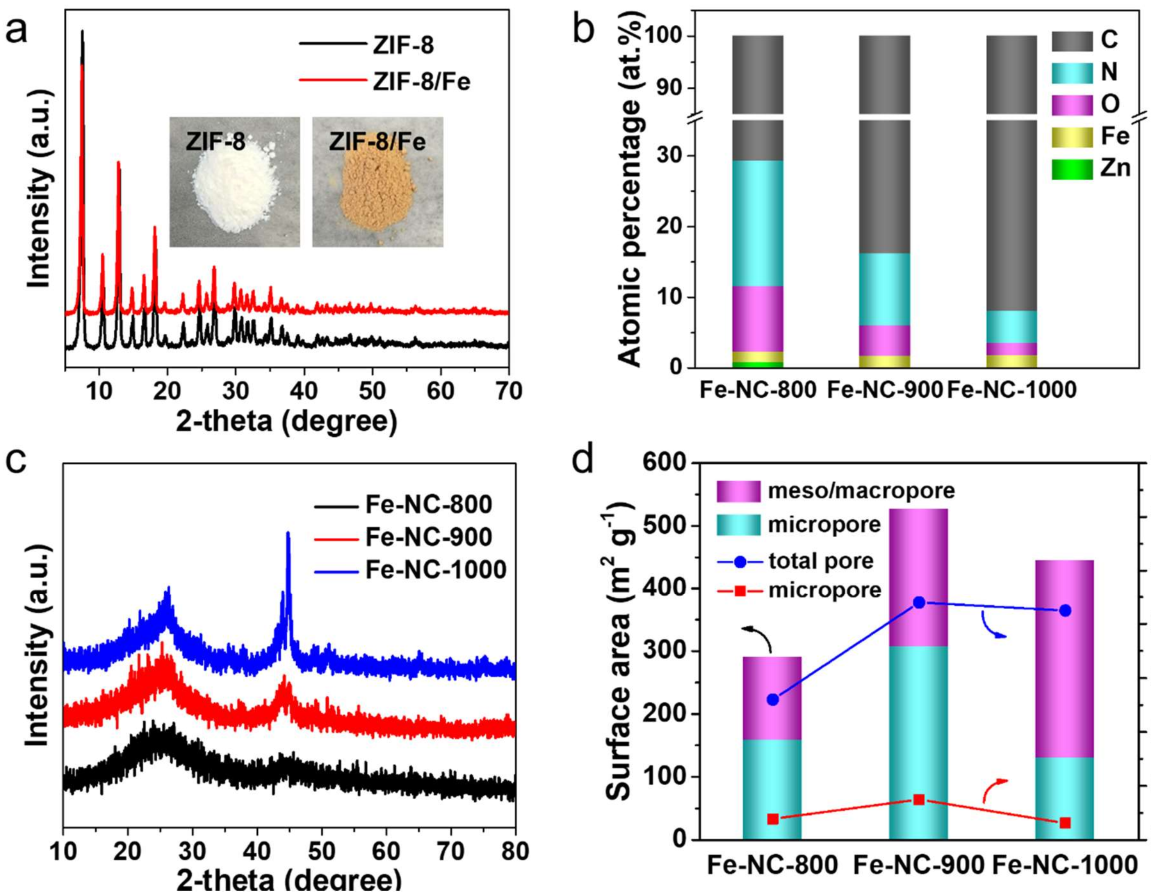

Figure 6.2. (a) XRD patterns of ZIF-8 and ZIF-8/Fe (insets show the digital photos of the samples). (b) Elemental composition of the Fe-NC catalysts determined by EDS. (c) XRD patterns of the Fe-NC catalysts prepared at different temperatures. (d) Comparison of the specific surface area and pore volume contributed from micropores and meso/macropores of the Fe-NC catalysts.

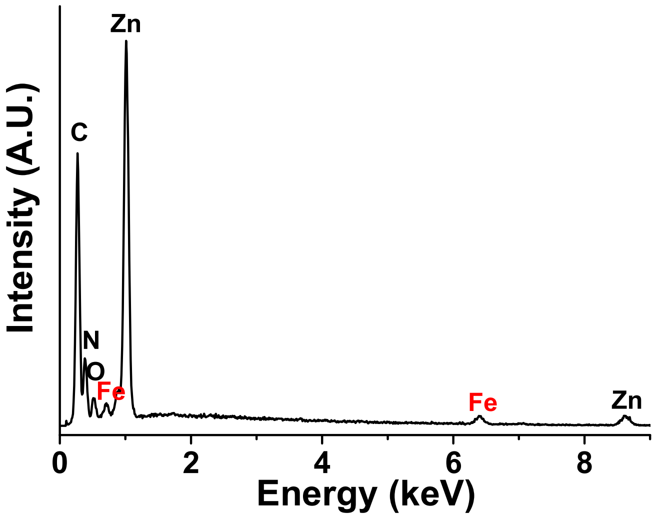

Figure 6.3. EDS spectrum of the ZIF-8/Fe.

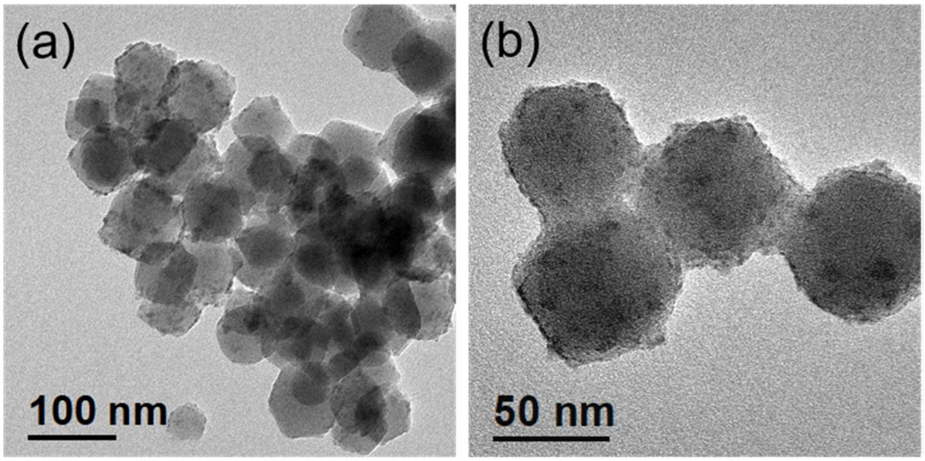

Figure 6.4. TEM images of ZIF-8/Fe.

Thermogravimetric analysis (TGA) shows that ZIF-8 starts to decompose and carbonize at around 620 ºC, followed by continuous weight loss at high temperature due to vaporization of Zn and loss of unstable species (**Figure 6.5a**). For ZIF-8/Fe, the gradual weight loss at low temperature is likely caused by the decomposition of iron carbonyl. The presence of Fe triggers the carbonization at a lower temperature of 570 ºC (**Figure 6.5b**), manifesting the interaction between ZIF-8 and Fe during pyrolysis. Thus, Fe-NC catalysts were obtained by pyrolysis of ZIF-8/Fe in N_2 at 800, 900 and 1000 ºC (generating Fe-NC-800, Fe-NC-900 and Fe-NC-1000 respectively) to optimize its composition and porous structure. As shown in **Figure 6.2b**, energy-dispersive X-ray spectroscopy (EDS) analysis shows that Zn has been completely removed during the heat treatment except for some minimal residual in Fe-NC-800. As the annealing temperature increases, the atomic contents of N and O decrease from 17.8 to 4.5 at.% and from 9.3 to 1.7 at.%, respectively, while the content of Fe remains in the range of 1.6-2.2 at.%. The XRD patterns (**Figure 6.2c**) indicate that the Fe-NC samples consist of amorphous carbon as characterized by the broad humps at around 26º. In Fe-NC-900, minor diffraction peaks due to crystalline moieties are observed at around 44º. The diffraction peaks become much more pronounced in Fe-NC-1000, which are identified as Fe and Fe_3C. Formation of such crystalline phases are common in Fe-N-C catalysts, and they might also contribute to the catalytic activity for ORR.[48, 56] Yet no Fe-related peaks is observed in the XRD pattern of Fe-NC-800, which may be because that Fe atoms in this sample mostly exists in a non-crystalline form.

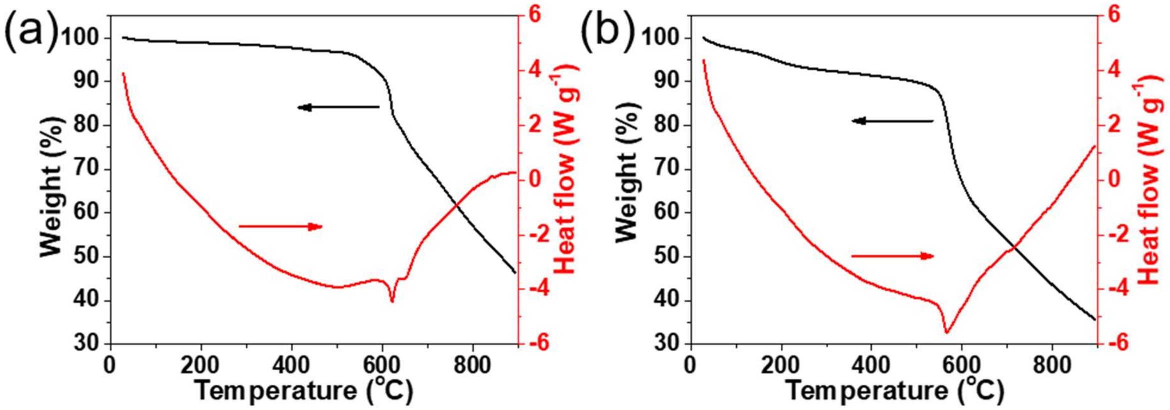

Figure 6.5. TGA and DSC curves of (a) ZIF-8 and (b) ZIF-8/Fe in N_2 flow.

Specific surface area and pore structure of the Fe-NC catalysts are characterized by N_2 adsorption-desorption isotherms (**Figure 6.6**). All three samples exhibit hierarchical pore structure consisting of micro-, meso- and macro- pores. The specific surface area and pore volume contributed from micropores and meso-/macropores are compared for the three catalysts in **Figure 6.2d**. At an annealing temperature of 800 ºC, the porosity of Fe-NC-800 is not fully developed, resulting in a moderate surface area of 290 m^2 g^{-1}. Raising the temperature to 900 ºC increases the surface area of Fe-NC-900 to 526 m^2 g^{-1} with a high microporous surface area of over 300 m^2 g^{-1}, as well as increased pore volume. Such high surface area is quite remarkable considering the absence of extra templates or supports. Further increasing the temperature to 1000 ºC somehow creates more meso-/macropores in Fe-NC-1000 yet substantially decreases the microporosity, resulting in a decreased surface area of 444 m^2 g^{-1}.

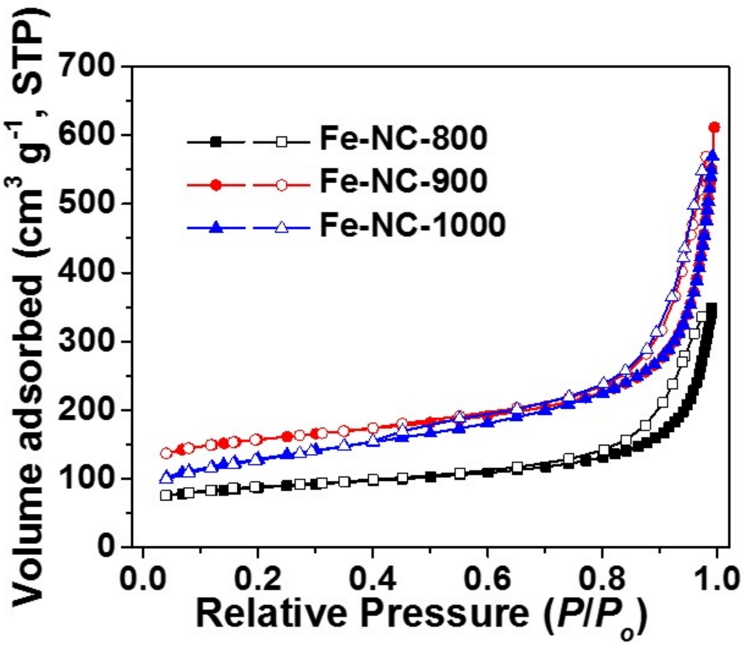

Figure 6.6. N_2 adsorption-desorption isotherms of Fe-NC catalysts.

Scanning electron microscope (SEM) and transmission electron microscope (TEM) were employed to investigate the Fe-NC catalysts. All of the samples show similar morphology under SEM observation with interconnected nanoparticles originated from the ZIF-8 nanocrystals (**Figure 6.7**). However, TEM images in **Figure 6.8** show different nanostructure of these samples. In line with the XRD result, no crystalline species are found in Fe-NC-800 (**Figure 6.8a and b**). The interconnected carbon particles form a disordered meso-/macroporous structure, and each carbon particle exhibits a highly microporous texture. For Fe-NC-900, similar hierarchical porous structure is observed with increased porosity (**Figure 6.8c**), which is expected from the loss of unstable species at high temperature. Moreover, crystalline Fe/Fe_3C nanoparticles with small size below 30 nm could be identified as black spots in the TEM images (arrow in **Figure 6.8d**), which are embedded in the carbon matrix. At a higher temperature of 1000 ºC, the Fe/Fe_3C nanoparticles further migrate, coalesce and grow into larger particles (**Figure 6.8e**), leaving behind many empty graphitic shells (arrow in **Figure 6.8f**). Such catalytic formation of graphitic carbon is common in the presence of Fe,[37, 148] and it is accounted for the increased meso-/macroporosity and elimination of micropores in Fe-NC-1000.

X-ray photoelectron spectroscopy (XPS) was performed to analyze the binding states of N and Fe of the Fe-NC catalysts (**Figure 6.9a and b**). The N 1s spectra show the existence of pyrrolic (400.2 eV) and pyridinic (398.4 eV) nitrogen, while the second peak, whose ratio decreases upon increasing temperature, might also include a contribution from nitrogen of Fe-N_x moieties.[94, 148, 157] The surface Fe content is found to be 4.25, 3.36 and 1.22 at.% for Fe-NC-800, 900, 1000 respectively. No signals of zero-valence Fe was observed in the Fe 2p spectra of the Fe-NC catalysts, and the peak at around 710 eV can be attributed to the Fe in Fe-N_x moieties, which agrees well with the TEM observation that the formed Fe particles in Fe-NC catalysts are coated with carbon.[98] High temperature treatment aggregates Fe atoms to form nanocrystals, removes N, O atoms and recovers defects in the carbon structure. Which might enhance the electronic conductivity but reduce the amount of ORR active sites. Therefore, a compromise should be made to achieve the optimal performance as discussed shortly.

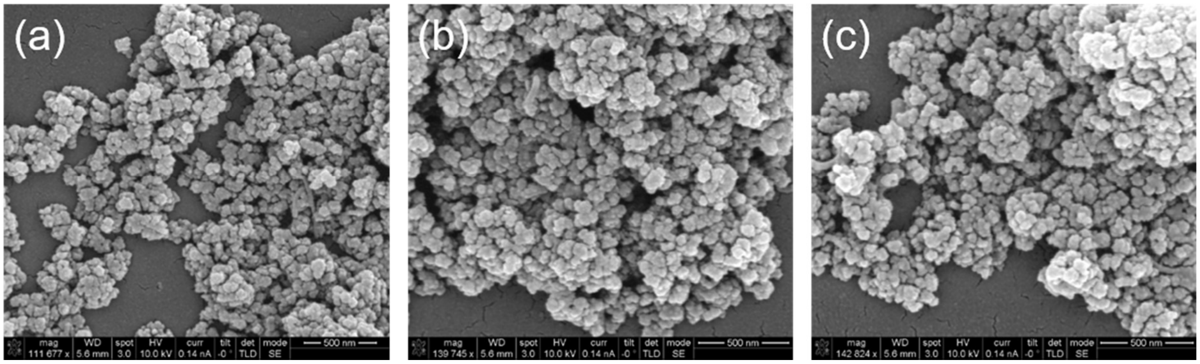

Figure 6.7. SEM images of (a) FE-NC-800, (b) Fe-NC-900 and (c) Fe-NC-1000. Scale bars are 500 nm.

The electrocatalytic performance of Fe-NC catalysts for ORR was evaluated in 0.1 M NaOH solution using a rotating disk electrode (RDE). The polarization curves shown in **Figure 6.9c** indicate that all of the three Fe-NC catalysts are highly active towards ORR. Among them, Fe-NC-900 shows the best electrocatalytic performance, which is approaching that of the benchmark Pt/C catalyst (40 wt%, Johnson Matthey, with a high loading of 50 μg cm^{-2}). A high half-wave potential ($E_{1/2}$) of 0.88V (vs. reversible hydrogen electrode, RHE) is obtained, together with an increased limiting current. In contrast, NC-900, prepared by pyrolyzing ZIF-8 at 900 ºC without iron carbonyl displays much inferior catalytic activity, confirming the critical role of Fe in forming active sites. Tafel plots (**Figure 6.10**) provide additional information regarding the electrocatalytic behaviors of the different catalysts. Fe-NC-900 and Fe-NC-1000 show small Tafel slopes of 62 and 59 mV dec^{-1} respectively, which are comparable to that of Pt/C (56 mV dec^{-1}). Fe-NC-800 however, exhibits a higher Tafel slope of 98 mV dec^{-1}, implying that the rate-determinant step might involve both charge transfer and the transport of reaction intermediates.[37]

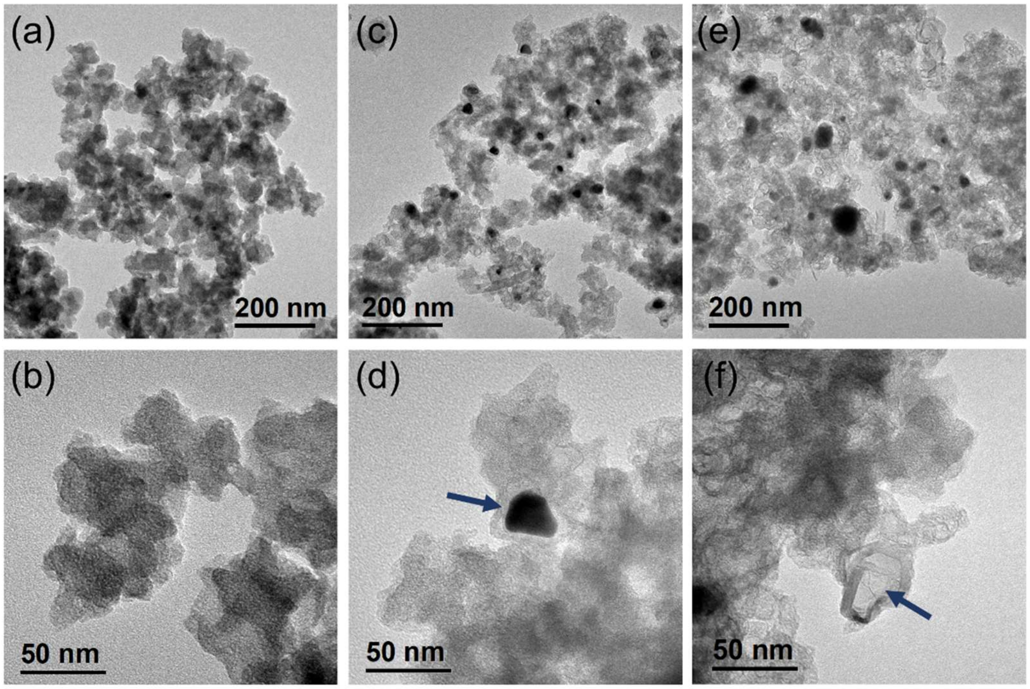

Figure 6.8. TEM images of (a, b) Fe-NC-800, (c, d) Fe-NC-900 (arrow in d indicates the Fe/Fe_3C crystalline nanoparticle), (e, f) Fe-NC-1000 (arrow in f indicates the cage-like structure).

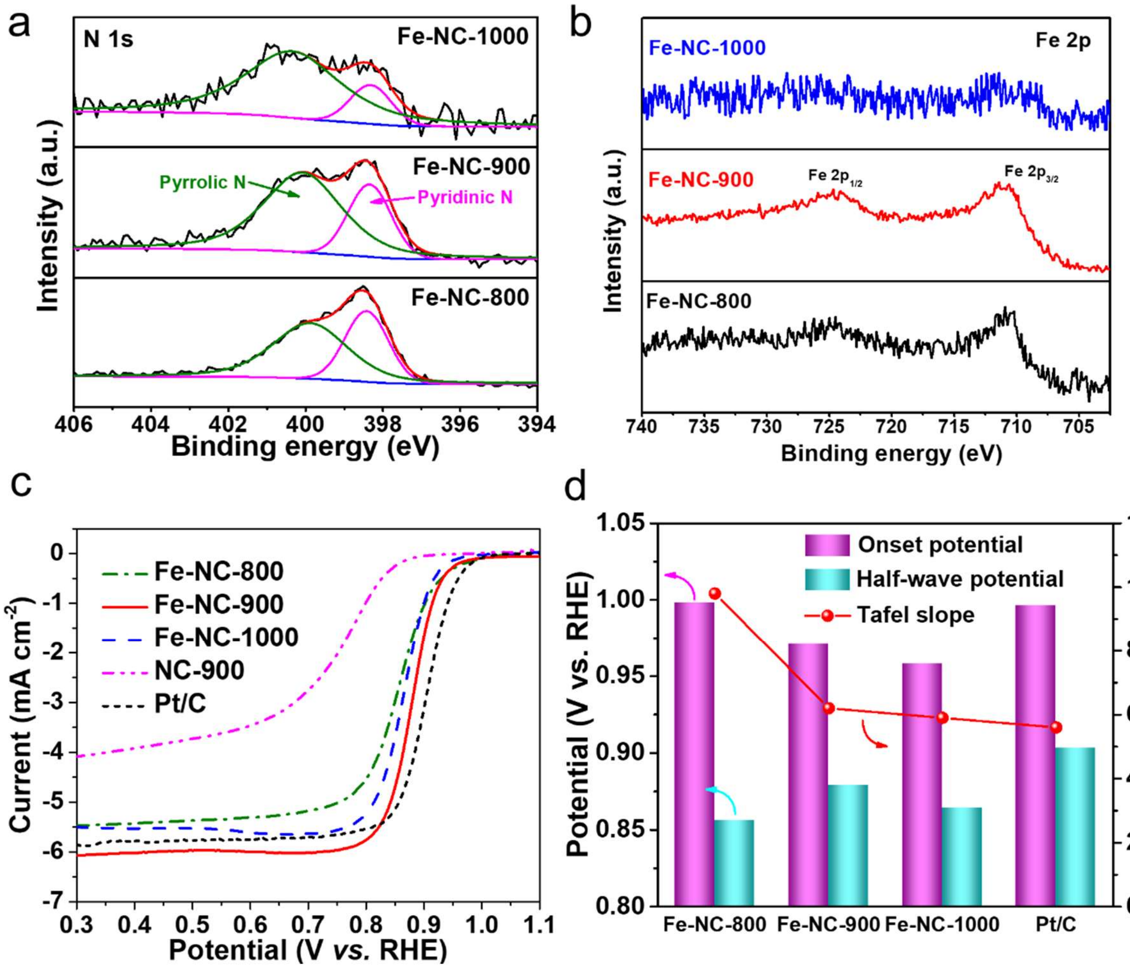

Figure 6.9. (a, b) XPS N 1s and Fe 2p spectra of Fe-NC catalysts prepared at different temperature. (c) Polarization curves of Fe-NC catalysts prepared at different temperature (loading: 0.25 mg cm^{-2}), NC-900 (loading: 0.25 mg cm^{-2}) and commercial 40 wt% Pt/C catalyst (Johnson Matthey, 50 μg Pt cm^{-2}) in 0.1 M NaOH at 1600 rpm. (d) Comparison of onset potential, half-wave potential and Tafel slope of different Fe-NC and Pt/C catalysts.

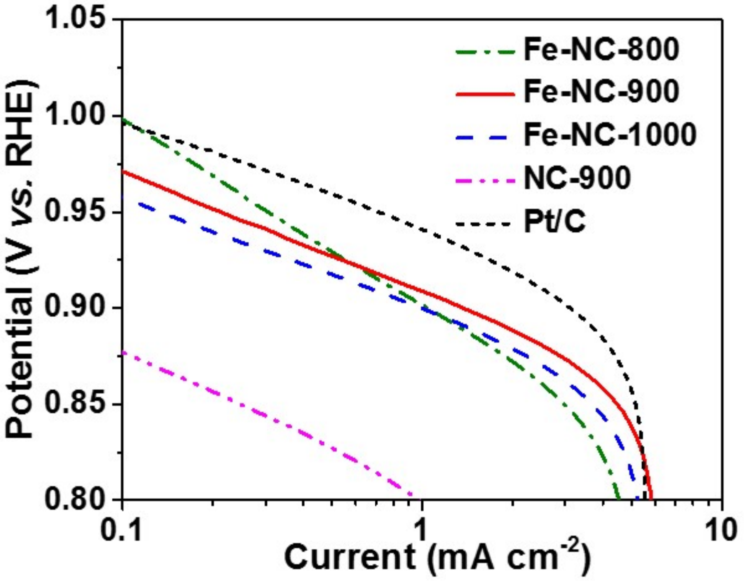

Figure 6.10. Tafel plots of Fe-NC catalyst, NC-900 and Pt/C derived from the polarization curves shown in **Figure 6.9c**.

The onset potentials, half-wave potentials and Tafel slopes of the Fe-NC and Pt/C catalysts are summarized for better comparison in **Figure 6.9d**. Interestingly, a higher temperature of pyrolysis results in a lower onset potential and a lower Tafel slope of the corresponding Fe-NC catalysts, for which several reasons can be assumed. First, the Fe-NC sample prepared at lower temperature exhibits higher N content, especially Fe-NC-800 exhibits the highest N content of 17.8 at.%, which may promote the formation of non-crystalline active sites like Fe-N_x. Such effect is supported by the absence of Fe-based particles and the highest surface Fe content in Fe-NC-800, which gives rise to its highest onset potential.[63] On the other hand, increase of annealing temperature in the case of Fe-NC-900 and Fe-NC-1000 substantially reduces N-doping and promotes the growth of Fe-based nanocrystallites. Which reduces surface Fe-N_x and lowers the onset potential. Nevertheless, higher temperature creates rich meso-/macropores (**Figure 6.2d**) and removes defects in the carbon matrix. As a result, the mass and electron transport are facilitated in Fe-NC-900 and Fe-NC-1000, which attribute to their lower Tafel slopes.

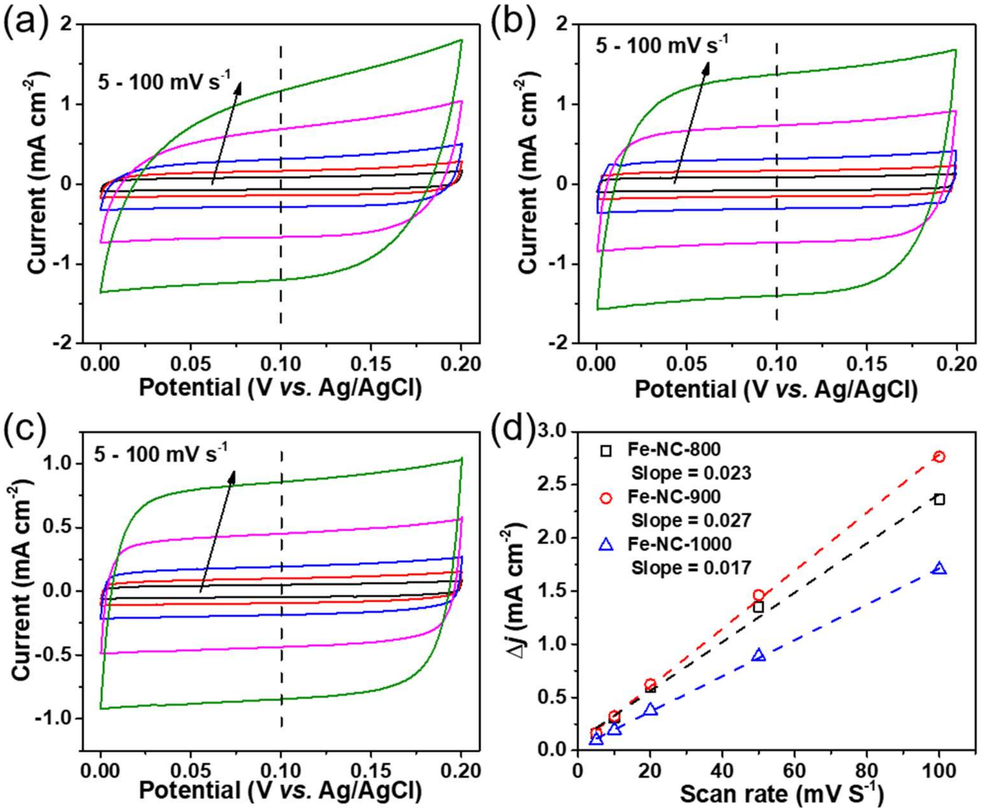

Figure 6.11. CV profiles of (a) Fe-NC-800, (b) Fe-NC-900, and (c) Fe-NC-1000 at scan rates of 5, 10, 20, 50, 100 mV s^{-1} in N_2 saturated 0.1 M NaOH. (d) Current density differences (Δj) plotted against scan rates. Δj is the difference between anodic and cathodic current densities at potential indicated by the black dash lines, where no redox current peaks are observed. The linear slopes in (d) are equivalent to twice of the electrochemical double-layer capacitances (Cdl). Cdl is generally used to represent the electrochemical surface area (ECSA).

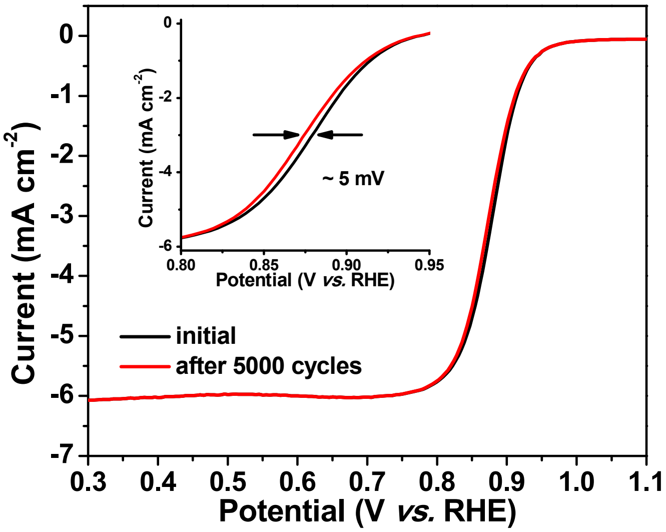

Figure 6.12. Polarization curves of Fe-NC-900 before and after 5000 CV cycles (inset shows the enlarged polarization curve) in 0.1 M NaOH at 1600 rpm.

In principle, an ideal catalyst should have a high onset potential and a small Tafel slope in order to achieve high current density with low over-potential. However, we find that the pyrolysis temperature shows contradictory effects on the Fe-NC catalysts, and consequently, a compromise results in the highest $E_{1/2}$ of Fe-NC-900. The high catalytic activity of Fe-NC-900 could also be understood by its high micropore surface area and electrochemical surface area (ECSA) (**Figure 6.11**) that host rich accessible Fe-N_x sites. Moreover, the stability of Fe-NC-900 was evaluated by continuous cyclic voltammetry (CV) scans between 0.6-1.0 V vs. RHE in O_2 saturated electrolyte.[48] The polarization curve of Fe-NC-900 after 5000 potential cycles well overlaps with the original one, with only a small shift of around 5 mV in $E_{1/2}$ (**Figure 6.12**), proving its excellent stability.

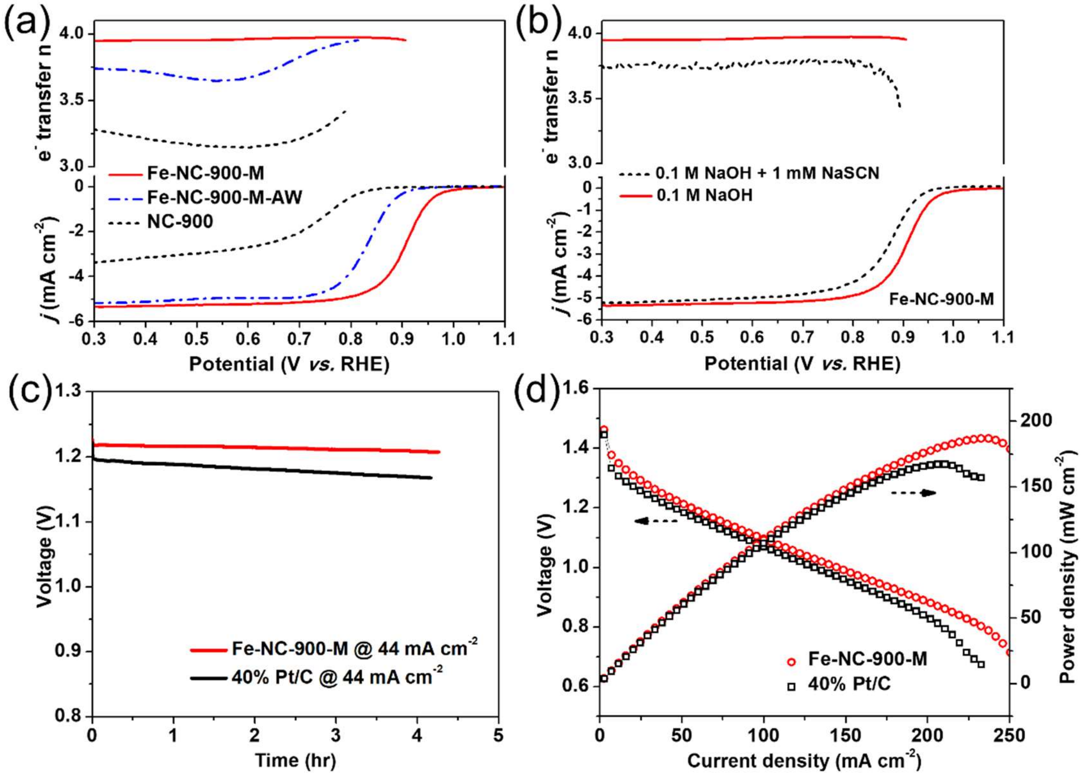

Figure 6.13 (a) Polarization curves and the corresponding electron transfer number of Fe-NC-900-M, Fe-NC-900-M-AW and NC-900 (loading: 0.25 mg cm^{-2}) in 0.1 M NaOH at 1600 rpm. (b) Polarization curves and the corresponding electron transfer number of Fe-NC-900-M (loading: 0.25 mg cm^{-2}) in 0.1 M NaOH with and without 1 mM NaSCN at 1600 rpm. (c) Discharge curves of the primary Zn-air batteries with Fe-NC-900-M and 40% Pt/C as cathode catalysts at 44 mA cm^{-2}. (d) Polarization curve and the corresponding power density plot of the Zn-air batteries with Fe-NC-900-M and 40% Pt/C as cathode catslysts.

Having optimized the pyrolysis temperature, we further investigated the possibility to improve the catalyst by increasing Fe content, which may increase the density of active sites. Specifically, the stirring time of ZIF-8 in iron carbonyl was extended from the original 4 h for Fe-NC-900 to 8 h for medium Fe loading (Fe-NC-900-M) and 12 h for high Fe loading (Fe-NC-900-H). As shown in **Figure 6.13a**, Fe-NC-900-M shows greatly improved catalytic performance in terms of a much higher half-wave potential of 0.91V, exceeding that of the benchmark Pt/C catalyst ($E_{1/2}$ = 0.90 V) and most of the NPMCs reported so far (**Table 5.1**). Whereas further increasing the Fe content significantly decreases the activity of Fe-NC-900-H (**Figure 6.14**). XRD and TEM results suggest that Fe-NC-900-M generally retains the nanostructure of Fe-NC-900 (**Figure 6.15**). However, excess loading of Fe produces abundant large Fe particles and catalyzes the growth of carbon nanotubes in Fe-NC-900-H, which might eliminate the Fe-N_x active sites residing in the pristine microporous carbon structure. In addition, the apparent catalytic performance can also be improved by increasing the catalyst loading on RDE. For example, tripling the loading of Fe-NC-900-M to 0.75 mg cm^{-2}, a value comparable to those of many reported NPMCs,[37, 51, 63] will dramatically increase the ORR limiting current (denoted as Fe-NC-900-M-HL in **Figure 6.16**).

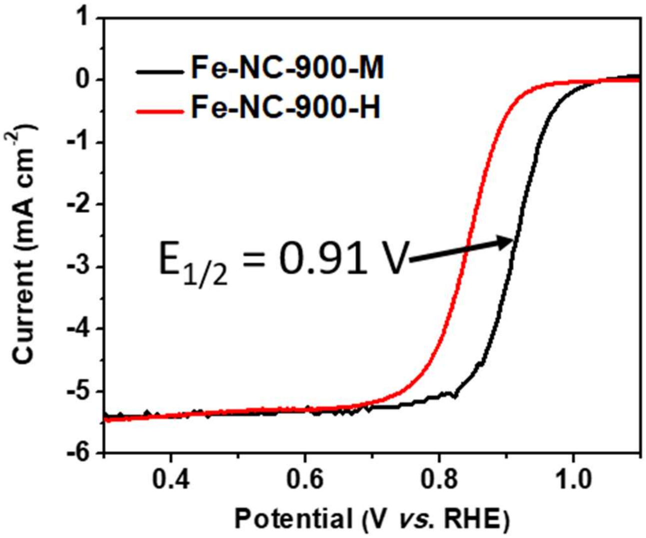

Figure 6.14. ORR polarization curves of Fe-NC-900-M and Fe-NC-900-H in 0.1 M NaOH at 1600 rpm.

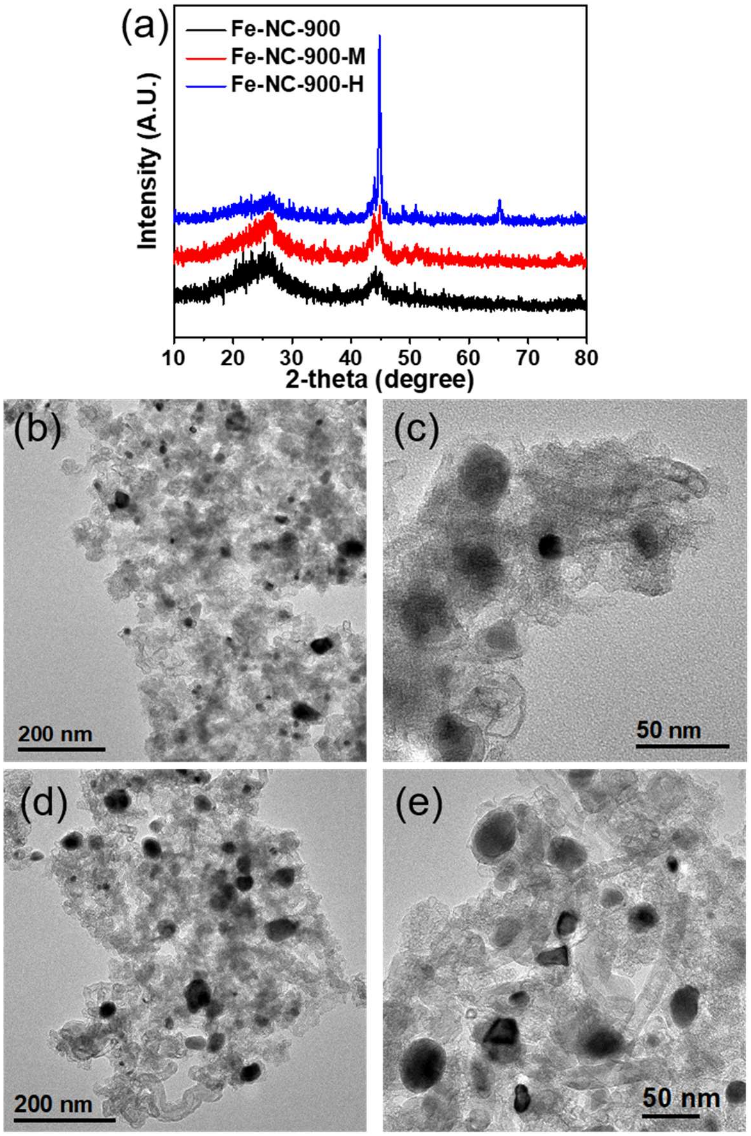

Figure 6.15. (a) XRD patterns of Fe-NC-900 catalysts with different Fe loading. TEM images of (b, c) Fe-NC-900-M and (d, e) Fe-NC-900-H.

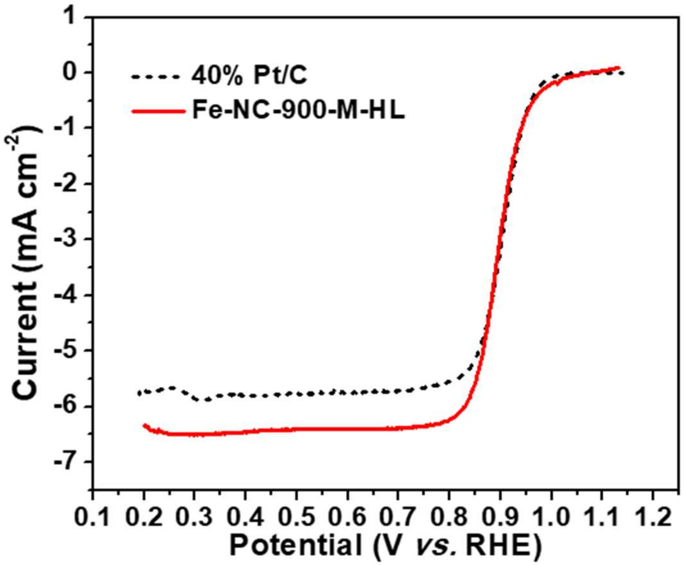

Figure 6.16. ORR polarization curves of Fe-NC-900-M-HL and Pt/C catalyst in 0.1 M NaOH at 1600 rpm.

Table 6.1. Comparison of various noble-metal free electrocatalysts for ORR in alkaline electrolyte.

Catalysts	Loading (mg cm^{-2})	Electrolyte	Onset Potential (V *vs.* RHE)	Half-wave Potential (V *vs.* RHE)	Reference
Fe-NC-900	0.25	0.1 M NaOH	0.97	0.88	This work
Fe-NC-900-M	0.25	0.1 M NaOH	1.02	0.91	This work
Co_3O_4/N-rmGO	0.17	0.1 M KOH	0.88	0.83	*Nat. Mater.* **2011**, *10*, 780
NPMC-1000	0.15	0.1 M KOH	0.94	0.85	*Nat. Nano.* **2015**, *10*, 444
Co@Co_3O_4@C-CM	0.1	0.1 M KOH	0.93	0.81	*Energy Environ. Sci.* **2015**, *8*, 568
(Fe, Mn)-N-C-3HT-2AL	0.8	0.1 M KOH	0.98	0.90	*Nat. Commun.* **2015**, *6*, 8618
FePhen@MOF-$ArNH_3$	0.6	0.1 M KOH	1.03	0.86	*Nat. Commun.* **2015**, *6*, 7343

N/Co-doped PCP//NRGO	~0.7	0.1 M KOH	0.97	0.86	*Adv. Funct. Mater.* **2015**, *25*, 872
[FeCo]O_4/NG	0.6	0.1 M KOH	0.98	0.866	*Angew. Chem. Int. Ed.* **2016**, *55*, 1340
CNT/PC	0.8	0.1 M KOH	NA	0.88	*J. Am. Chem. Soc.* **2016**, *138*, 15046
Co SAs/N-C(900)	0.408	0.1 M KOH	0.982	0.881	*Angew.Chem. Int.Ed.* **2016**, *55*, 10800
Fe@C-FeNC-2	0.7	0.1 M KOH	NA	0.899	*J. Am. Chem. Soc.* **2016**, *138*, 3570
{Co}[FeCo]O_4/NG	0.6	0.1 M KOH	0.98	0.866	*Angew. Chem. Int. Ed.* **2016**, *55*, 1340
N,P-HPC	0.8	0.1 M NaOH	0.924	0.853	*J. Mater. Chem. A.*, **2017**, *5*, 24329
Fe-ISAs/CN	0.408	0.1 M KOH	0.986	0.90	*Angew. Chem. Int. Ed.* **2017**, *56*, 6937
S,N-Fe/N/C-CNT	0.6	0.1 M KOH	NA	0.85	*Angew. Chem. Int. Ed.* **2017**, *56*, 610
1000-CNS	0.14	0.1 M KOH	0.99	0.85	*Energy Environ. Sci.* **2017**, *10*, 742
CF-NG-Co	0.28	0.1 M NaOH	0.97	0.88	*J. Mater. Chem. A.*, **2018**, *6*, 489
FeN_x-PNC	0.14	0.1 M KOH	0.997	0.86	*ACS Nano* **2018**, 12, 1949

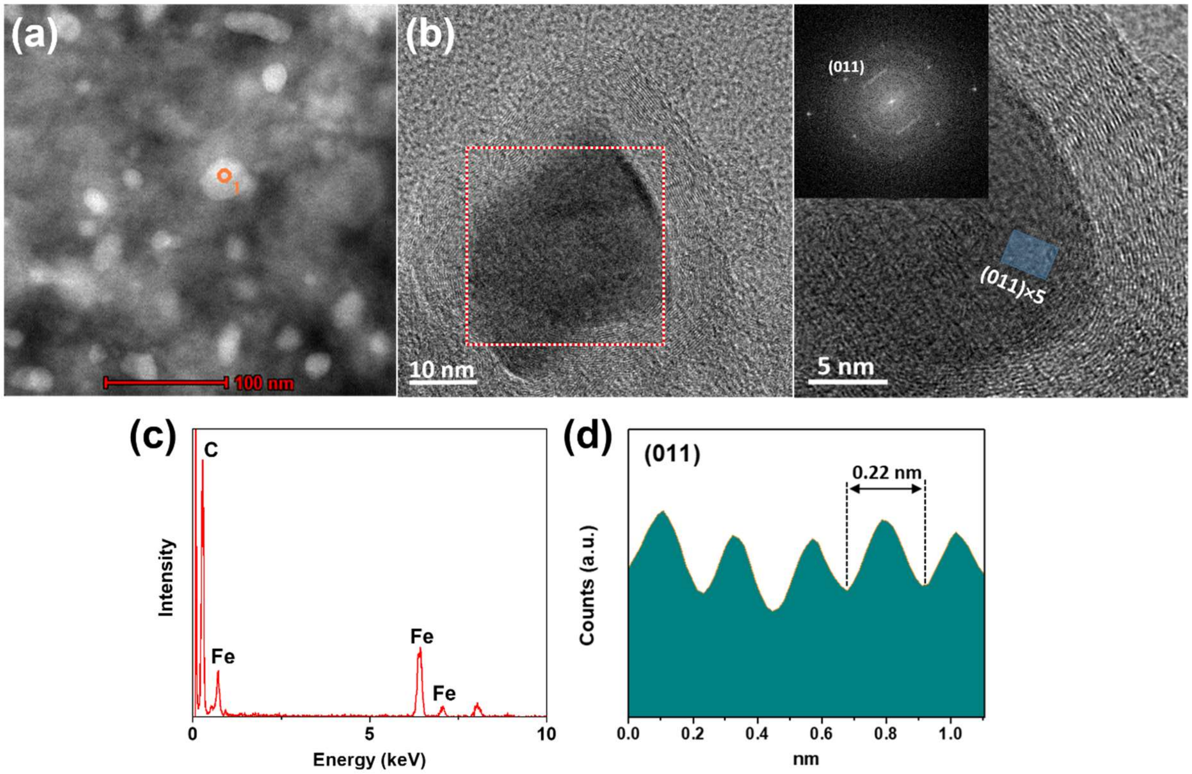

Figure 6.17. (a, b) HAADF-STEM image and HRTEM image of Fe-NC-900-M (the inset in b being the fast Fourier transform of the TEM image of a typical nanoparticle), (c) EDS point-shot spectrum of the point denoted in (a), (d) Surface plots of the sample in (b). As shown in **Figure 6.17a**, the Fe-NC-900-M sample contains uniformly distributed nanoparticles of under forty nanometers in diameter. The EDS spectrum of one typical nanoparticle reveals its composition to be primarily iron and carbon (**Figure 6.17c**). The HRTEM image and the corresponding fast Fourier transform of a typical nanoparticle further reveals its crystalline structure (**Figure 6.17b, d**). The continuous lattice distance of 0.22 nm should be attributed to the (011) planes of metallic iron (cubic) or (220) planes of Fe_3C. Which agrees well with the above EDS result and the XRD results in **Figure 6.15**.

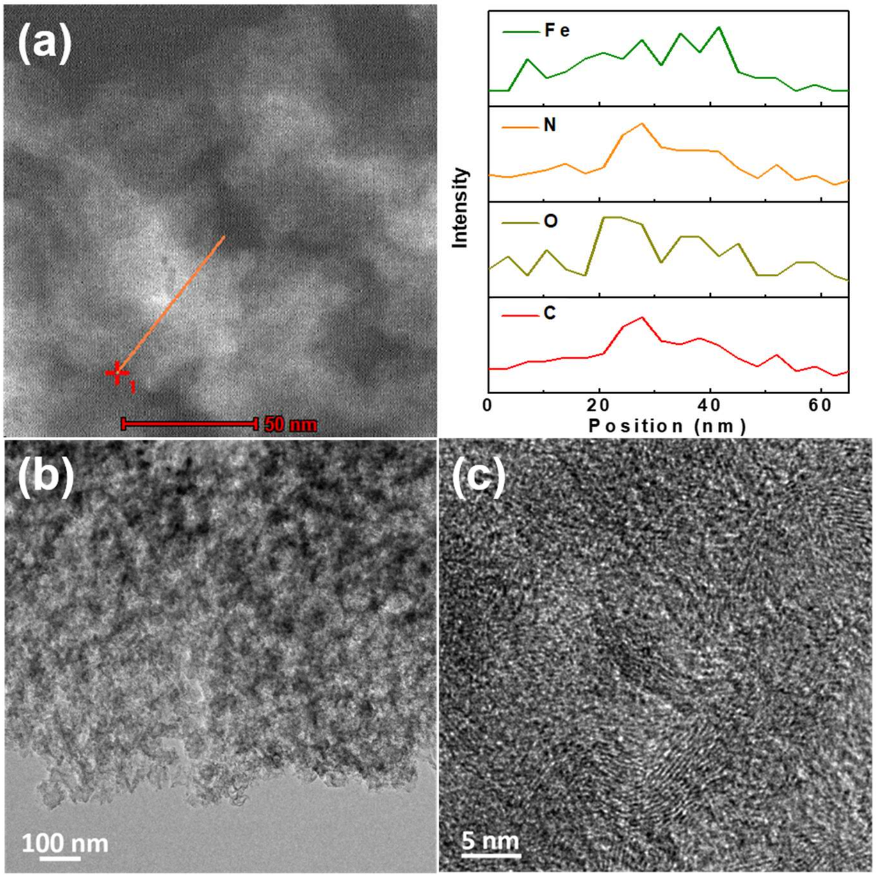

Figure 6.18. (a) HAADF-STEM image of Fe-NC-900-M-AW and the EDS linear scan spectrum corresponding to the line in the image, (b, c) TEM image of Fe-NC-900-M-AW. As shown in **Figure 6.18a**, the HAADF-STEM image of Fe-NC-900-M-AW reveals that the Fe/Fe_3C nanoparticles in Fe-NC-900-M has been thoroughly removed after acid washing. However the remaining uniformly distributed angstrom level bright dots on the carbon scaffold should correspond to the iron atom reserved in Fe-N_x moieties. The EDS linear scan reveals the existence of C, N, O and Fe in the sample, and their even distribution across the line, proving the uniform distribution of these elements in the catalyst. Normal TEM image of Fe-NC-900-M-AW (**Figure 6.18b**) confirms the absence of nanoparticle in the sample, and the HRTEM image in **Figure 6.18c** shows an empty graphitic shell where the Fe based nanoparticle has been removed by acid washing.

The preservation of Fe-N_x in Fe-NC-900-M-AW is further proved by its XPS Fe 2p spectrum (**Figure 6.19**), which shows the pronounced peak at around 710 eV, similar to that of Fe-NC-900 in **Figure 6.9**.

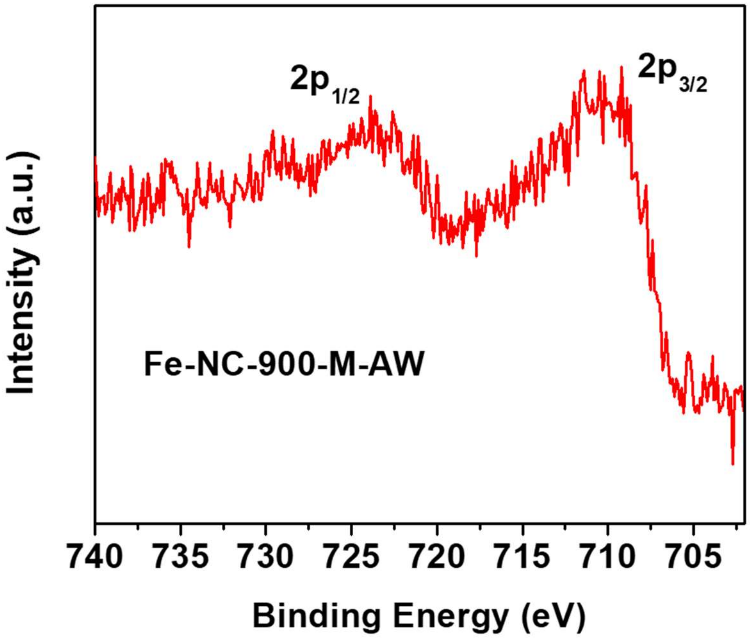

Figure 6.19. XPS Fe 2p spectrum of Fe-NC-900-M-AW.

To investigate the function of different components of Fe-NC catalysts in catalyzing ORR, Fe-NC-900-M was washed with 0.5 M H_2SO_4 to remove Fe/Fe_3C nanocrystallites while retaining the Fe-N_x moieties (**Figure 6.17-6.19**). As shown in **Figure 6.13a**, rotating ring-disk electrode (RRDE) measurements reveals that the electron transfer number of Fe-NC-900-M is greater than 3.9 in the whole potential range, indicating near-perfect selectivity of 4 e^- pathway. On the other hand, the nanoparticle-free Fe-NC-900-M-AW exhibited a much lower $E_{1/2}$ (0.83 V) and electron transfer number (~3.7), which is however, still much higher than those of the Fe-free NC-900. The above results concludes that Fe-N_x are the major active sites of Fe-NC-900-M, while the presence of fine Fe/Fe_3C particles could further improve the performance of the catalyst through synergistic effect.[56, 70, 173] We also tested the RRDE performance of Fe-NC-900-M with the presence of NaSCN in the electrolyte, where it is known that SCN^- ion can poison Fe-N_x sites in catalyzing ORR.[61] As shown in **Figure 6.20**, the $E_{1/2}$ of Fe-NC-900-M decreases dramatically by about 40 mV, and the electron transfer number drops to about 3.7 after adding 1 mM NaSCN. These results again confirms our previous conclusion.

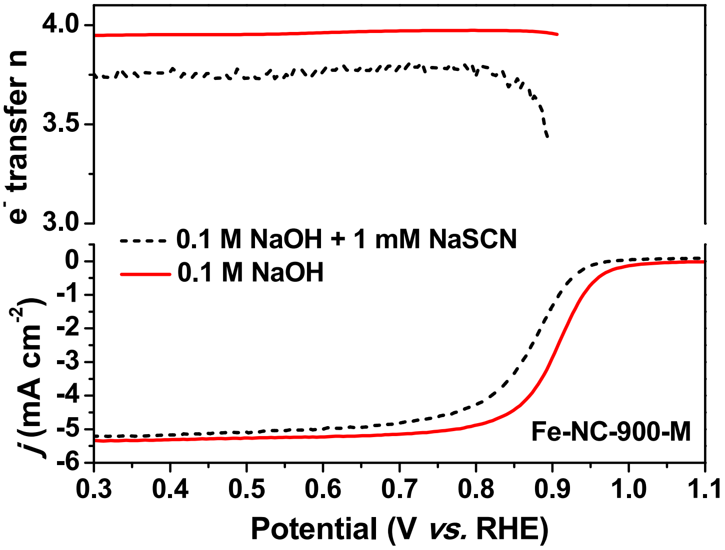

Figure 6.20. Polarization curves and the corresponding electron transfer number of Fe-NC-900-M (loading: 0.25 mg cm^{-2}) in 0.1 M NaOH with and without 1 mM NaSCN at 1600 rpm.

To further demonstrate the application potential of Fe-NC-900-M, we tested its performance in a homemade zinc-air battery. Specifically, Fe-NC-900-M, Zn foil and 6 M KOH are employed as air cathode, anode and electrolyte respectively. 40% Pt/C catalyst were also tested under the same condition for comparison. As shown in **Figure 6.13b-d**, the zinc-air battery constructed with Fe-NC-900-M as cathode catalyst exhibits an open circuit voltage of 1.5 V, a voltage plateau of 1.22 V at a current density of 44 mA cm^{-2}, and a peak power density of 271 mW cm^{-2}. Which exceeds those of 40% Pt/C catalyst (1.48 V, 1.19 V and 242 mW cm^{-2}), and most NPMCs reported so far (**Table 6.2**).[79, 129, 174, 187-190] Additionally, the present method can also be easily extended to synthesize M-NC catalysts with other transition metals, by using the corresponding metal carbonyls. Though preliminary results show inferior activity of other M-NC catalysts (**Figure 6.21**), incorporating multiple metal centers in the present Fe-NC catalysts might further improve its activity.[37]

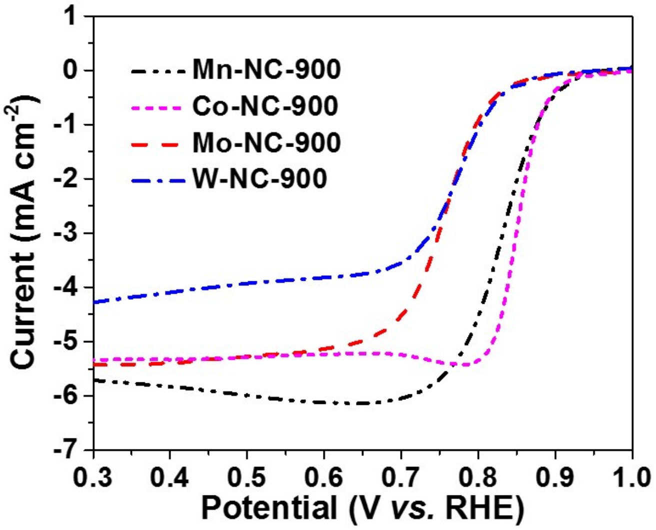

Figure 6.21. Polarization curves of M-NC catalysts with different transition metals in 0.1 M NaOH at 1600 rpm (loading: 0.5 mg cm^{-2}).

Table 6.2. Comparison of zinc-air battery utilizing Fe-NC-900-M with other noble-metal free electrocatalysts reported recently.

Catalysts	Loading (mg cm^{-2})	Open circuit Voltage (V)	Peak power (mW cm^{-2})	Reference
Fe-NC-900-M	0.73	1.5	271	This work
Co-N-CNT	1	1.365	101	*Adv. Funct. Mater.* **2018**, *28*, 1705048
CF-NG-Co	1	1.49	160	*J. Mater. Chem. A* **2018**, *6*, 489
1100-CNS-4	2	1.49	151	*Energy Environ. Sci.* **2017**, *10*, 742
S,N-Fe/N/C-CNT	1.25	1.35	102.7	*Angew. Chem. Int. Ed.* **2017**, *56*, 610
N-GCNT/FeCo	2	1.48	89.3	*Adv. Energy Mater.* **2017**, *7*, 1602420
N-HCNs	1	1.49	76	*Nanoscale.* **2017**, *9*, 13257
Fe/N/C@BMZIF	1	1.48	235	*ACS Appl. Mater. Interfaces* **2017**, *9*, 5213
PFe-Pc	2	1.6	192	*Dalton Trans.* **2017**, *46*, 1803
Fe,N-CNS	1	~1.375	221	*Adv. Sustainable Syst.* **2017**, *1,* 1700085
Co/Co$_x$S$_y$@SNCF-800	2	1.37	230	*ACS Appl. Mater. Interfaces* **2017**, *9,* 34269
Fe$_2$N@NC	1	1.48	82.3	*Catal. Sci. Technol.* **2017**, *7*, 5670
Co$_4$N/CNW/CC	1	1.4	174	*J. Am. Chem. Soc.* **2016**, *138*, 10226
Co$_3$O$_4$-NCNT/SS	NA	NA	160.7	*Adv. Mater.* **2016**, *28*, 6421
Fe/Fe$_2$O$_3$@Fe-N-C	2	1.47	220	*Nano Res.* **2016**, *9*, 2133
Fe@N-C-700	2.2	1.4	220	*Nano Energy* **2015**, *13*, 387
CoO/N-CNT	1	1.4	265	*Nat. Commun.* **2013**, *4*, 1805

6.4 Conclusion

In summary, we have developed a low-cost and easy-scalable method to synthesize Fe-NC catalysts based on the direct pyrolysis of iron carbonyl decorated ZIF-8. Increasing pyrolysis temperature is revealed to lower the onset potential as well as the Tafel slope of the catalyst, as a result of the altered chemical composition and porous structure. The optimized Fe-NC-900-M catalyst shows excellent electro-catalytic activity for ORR with a half-wave potential of 0.91 V, which is also attributed to the synergistic effect between Fe-N_x and Fe/Fe_3C nanocrystallites of the catalyst. Furthermore, the zinc-air battery constructed with Fe-NC-900-M as cathode catalyst exhibits high open-circuit voltage (1.5 V) and peak power density (271 mW cm^{-2}), which outperforms that of 40% Pt/C catalyst and most noble-metal free ORR catalysts reported so far. The Fe-NC are promising candidates to replace Pt-based catalysts, and would play an important role in the development of high-performance and low-cost metal-air batteries.

Chapter 7. Conclusion of Dissertation

Hydrogen fuel cells and metal-air batteries are promising EES devices as power source for future electric vehicle applications because of their high theoretical energy and power densities. The major technological issue of these technologies lies in developing non-precious metal catalysts to replace the expensive and scarce Pt-based catalyst for catalyzing the sluggish cathode oxygen reduction reaction. Pyrolyzed iron-nitrogen-carbon (Fe-N-C) catalysts is widely regarded as the most promising candidate for replacing platinum due to their high activity. However, the traditional method for preparing Fe-N-C catalysts involves the high temperature pyrolysis of the mixed iron, nitrogen and carbon precursors, which results in the complex and unpredictable chemical phases and catalysts structure of the product. The random nature of such synthetic method makes the identification of active site and rational design of the materials highly challenging.

To solve the problem, we designed a novel "post iron decoration" synthetic strategy towards efficient Fe-N-C catalysts that de-convolutes the growth of iron and nitrogen species, enables the rational design of the catalyst structure, and provides a series of effective model materials for active site probing. The best performing Fe/NMC catalysts exhibited a high half-wave potential of 0.862 V, which is close to that of the benchmark 40% Pt/C catalyst. The high activity is attributed to the $Fe-N_x$ species, and the surface oxidized Fe crystallites though not being the major active site, is revealed to reduce HO_2^-, the 2e ORR product, facilitating the 4e reduction of oxygen. Finally, such synthetic strategy is successfully extended to prepare other Me-N-C materials.

Based on the established understanding of active site formation, we further synthesized Fe-NC catalyst of improved performance by the pyrolysis of $Fe(CO)_5$/ZIF-8 complex. Thus prepared Fe-NC catalyst could host the uniformly distributed active sites by micro-pores and promote charge/mass transport by meso-/macro-pores, providing abundant easily accessible ORR active sites. In virtue of these advantageous features, the best performing Fe-NC catalyst exhibited a high half-wave potential of 0.91 V in rotating disk electrode experiment in 0.1 M NaOH. Furthermore, the zinc-air battery constructed with Fe-NC-900-M as cathode catalyst exhibits high open-circuit voltage (1.5 V) and peak power density (271 mW cm^{-2}), which outperforms those of 40% Pt/C catalyst (1.48 V, 1.19 V and 242 mW cm^{-2}), and most noble-metal free ORR catalysts reported so far. Finally, such synthetic method is economic and easily-scalable, and can easily incorporate other metals in the structure, offering possibility for further activity and durability improvement.

We hope the work of this dissertation could shed light on the understanding of Fe-N-C materials, and inspire the designing of Me-N-C materials with improved performance for various applications.

Reference

1. G., John B.; Park, K.-S., The Li-Ion Rechargeable Battery: A Perspective. Journal of the American Chemical Society 2013, 135 (4), 1167-1176.

2. H., Martin I.; Caldeira, K.; Jain, A. K.; Haites, E. F.; Harvey, L. D. D.; Potter, S. D.; Schlesinger, M. E.; Schneider, S. H.; Watts, R. G.; Wigley, T. M. L.; Wuebbles, D. J., Energy implications of future stabilization of atmospheric CO_2 content. Nature 1998, 395, 881.

3. M., Kazuhiko; Domen, K., Photocatalytic Water Splitting: Recent Progress and Future Challenges. The Journal of Physical Chemistry Letters 2010, 1 (18), 2655-2661.

4. T., Michael M.; Wolverton, C.; Isaacs, E. D., Electrical energy storage for transportation-approaching the limits of, and going beyond, lithium-ion batteries. Energy & Environmental Science 2012, 5 (7), 7854-7863.

5. T., Robert J.; Diffenbaugh, N. S.; Brooks, H. E.; Baldwin, M. E.; Robinson, E. D.; Pal, J. S., Changes in severe thunderstorm environment frequency during the 21st century caused by anthropogenically enhanced global radiative forcing. Proceedings of the National Academy of Sciences 2007, 104 (50), 19719-19723.

6. a. S. A., What is U.S. electricity generation by energy source? U.S. Energy Information Administration 2017.

7. A., M.; Tarascon, J. M., Building better batteries. Nature 2008, 451, 652.

8. A. T., Fuel cell/battery system. 2013.

9. K., A.; Jain, S.; Nema, R. K., A review on fuel cell technologies and power electronic interface. Renewable and Sustainable Energy Reviews 2009, 13 (9), 2430-2440.

10. V., John R.; Atanassov, P.; Dekel, D. R.; Herring, A. M.; Hickner, M. A.; Kohl, P. A.; Kucernak, A. R.; Mustain, W. E.; Nijmeijer, K.; Scott, K.; Xu, T.; Zhuang, L., Anion-exchange membranes in electrochemical energy systems. Energy & Environmental Science 2014, 7 (10), 3135-3191.

11. L., Yanguang; Dai, H., Recent advances in zinc-air batteries. Chemical Society Reviews 2014, 43 (15), 5257-5275.

12. W. K. H.; Da-Wei, W.; Dang-Sheng, S.; R., G. I., A Discussion on the Activity Origin in Metal-Free Nitrogen-Doped Carbons For Oxygen Reduction Reaction and their Mechanisms. ChemSusChem 2015, 8 (17), 2772-2788.

13. R., Nagappan; Mukerjee, S., Fundamental Mechanistic Understanding of Electrocatalysis of Oxygen Reduction on Pt and Non-Pt Surfaces: Acid versus Alkaline Media. Advances in Physical Chemistry 2012, 2012, 17.

14. B., B. B.; Ross, P. N.; Markovic, N. M., Oxygen electroreduction on Ag(111): The pH effect. Electrochimica Acta 2007, 52 (6), 2264-2271.

15. B., Allen J., Inner-Sphere Heterogeneous Electrode Reactions. Electrocatalysis and Photocatalysis: The Challenge. Journal of the American Chemical Society 2010, 132 (22), 7559-7567.

16. J. S. G., On the magnetic properties of some haemoglobin complexes. Proceedings of the Royal Society of London. Series A. Mathematical and Physical Sciences 1956, 235 (1200), 23-36.

17. Y., Ernest, Recent Advances in the Science of Electrocatalysis. Journal of The Electrochemical Society 1981, 128 (4), 160C-171C.

18. N., J. K.; Rossmeisl, J.; Logadottir, A.; Lindqvist, L.; Kitchin, J. R.; Bligaard, T.; Jónsson, H., Origin of the Overpotential for Oxygen Reduction at a Fuel-Cell Cathode. The Journal of Physical Chemistry B 2004, 108 (46), 17886-17892.

19. B., Thomas; Nørskov, J. K.; Dahl, S.; Matthiesen, J.; Christensen, C. H.; Sehested, J., The Brønsted–Evans–Polanyi relation and the volcano curve in heterogeneous catalysis. 2004; Vol. 224, p 206-217.

20. S. V.; Simon, M. B.; J., M. K. J.; N., R. P.; M., M. N.; Jan, R.; Jeff, G.; K., N. J., Changing the Activity of Electrocatalysts for Oxygen Reduction by Tuning the Surface Electronic Structure. Angewandte Chemie International Edition 2006, 45 (18), 2897-2901.

21. H., Xiaoqing; Zhao, Z.; Cao, L.; Chen, Y.; Zhu, E.; Lin, Z.; Li, M.; Yan, A.; Zettl, A.; Wang,

Y. M.; Duan, X.; Mueller, T.; Huang, Y., High-performance transition metal–doped Pt_3Ni octahedra for oxygen reduction reaction. Science 2015, 348 (6240), 1230-1234.

22. K., K., Particle Size Effects for Oxygen Reduction on Highly Dispersed Platinum in Acid Electrolytes. Journal of The Electrochemical Society 1990, 137 (3), 845-848.

23. J. R. K.; Nørskov, J. K.; Barteau, M. A.; Chen, J. G., Modification of the surface electronic and chemical properties of Pt(111) by subsurface 3d transition metals. The Journal of Chemical Physics 2004, 120 (21), 10240-10246.

24. X., Ye; Ruban, A. V.; Mavrikakis, M., Adsorption and Dissociation of O2 on Pt−Co and Pt−Fe Alloys. Journal of the American Chemical Society 2004, 126 (14), 4717-4725.

25. M., Nenad; Gasteiger, H.; Ross, P. N., Kinetics of Oxygen Reduction on Pt(hkl) Electrodes: Implications for the Crystallite Size Effect with Supported Pt Electrocatalysts. Journal of The Electrochemical Society 1997, 144 (5), 1591-1597.

26. T. R. J.; Zdeněk, S.; Martin, P., Transition Metal Oxides for the Oxygen Reduction Reaction: Influence of the Oxidation States of the Metal and its Position on the Periodic Table. ChemPhysChem 2015, 16 (16), 3527-3531.

27. W., Gang; Zelenay, P., Nanostructured Nonprecious Metal Catalysts for Oxygen Reduction Reaction. Accounts of Chemical Research 2013, 46 (8), 1878-1889.

28. J. D. O., Deconstructing SALt's saltwater lamp. 2015.

29. Easy notecards. 2010.

30. Z. J., PEM Fuel Cell Electrocatalysts and Catalyst Layers. 2008.

31. M. C., James P.; Devaraj, N. K.; Decréau, R. A.; Yang, Y.; Yan, Y.-L.; Ebina, W.; Eberspacher, T. A.; Chidsey, C. E. D., A Cytochrome c Oxidase Model Catalyzes Oxygen to Water Reduction Under Rate-Limiting Electron Flux. Science 2007, 315 (5818), 1565-1568.

32. ChemTube3D. University of Liverpool.

33. Z. J. H., Bedioui, Fethi, Dodelet, J.P., N4-Macrocyclic Metal Complexes. 2006.

34. G., S.; Tryk, D.; Bae, I.; Aldred, W.; Yeager, E., Heat-treated polyacrylonitrile-based catalysts for oxygen electroreduction. Journal of Applied Electrochemistry 1989, 19 (1), 19-27.

35. C., James P.; Denisevich, P.; Konai, Y.; Marrocco, M.; Koval, C.; Anson, F. C., Electrode catalysis of the four-electron reduction of oxygen to water by dicobalt face-to-face porphyrins. Journal of the American Chemical Society 1980, 102 (19), 6027-6036.

36. L., Michel; Proietti, E.; Jaouen, F.; Dodelet, J.-P., Iron-Based Catalysts with Improved Oxygen Reduction Activity in Polymer Electrolyte Fuel Cells. Science 2009, 324 (5923), 71-74.

37. W., Gang; More, K. L.; Johnston, C. M.; Zelenay, P., High-Performance Electrocatalysts for

Oxygen Reduction Derived from Polyaniline, Iron, and Cobalt. Science 2011, 332 (6028), 443-447.

38. M., Paul H.; Wang, E.; Millet, J.-M. M.; Ozkan, U. S., Characterization of the Iron Phase in CNx-Based Oxygen Reduction Reaction Catalysts. The Journal of Physical Chemistry C 2007, 111 (3), 1444-1450.

39. P., Eric; Jaouen, F.; Lefèvre, M.; Larouche, N.; Tian, J.; Herranz, J.; Dodelet, J.-P., Iron-based cathode catalyst with enhanced power density in polymer electrolyte membrane fuel cells. Nature Communications 2011, 2, 416.

40. M. J.; Wei, X.; Martin, M.; Wolfgang, S., On the Role of Metals in Nitrogen-Doped Carbon Electrocatalysts for Oxygen Reduction. Angewandte Chemie International Edition 2015, 54 (35), 10102-10120.

41. L., Wenmu; Wu, J.; Higgins, D. C.; Choi, J.-Y.; Chen, Z., Determination of Iron Active Sites in Pyrolyzed Iron-Based Catalysts for the Oxygen Reduction Reaction. ACS Cat. 2012, 2 (12), 2761-2768.

42. S., Mengxia; Wei, C.; Ai, K.; Lu, L., Transition metal–nitrogen–carbon nanostructured catalysts for the oxygen reduction reaction: From mechanistic insights to structural optimization. Nano Research 2017, 10 (5), 1449-1470.

43. J., Qingying; Ramaswamy, N.; Tylus, U.; Strickland, K.; Li, J.; Serov, A.; Artyushkova, K.;

Atanassov, P.; Anibal, J.; Gumeci, C.; Barton, S. C.; Sougrati, M.-T.; Jaouen, F.; Halevi, B.; Mukerjee, S., Spectroscopic insights into the nature of active sites in iron–nitrogen–carbon electrocatalysts for oxygen reduction in acid. Nano Energy 2016, 29, 65-82.

44. L., Jingkun; Ghoshal, S.; Liang, W.; Sougrati, M.-T.; Jaouen, F.; Halevi, B.; McKinney, S.; McCool, G.; Ma, C.; Yuan, X.; Ma, Z.-F.; Mukerjee, S.; Jia, Q., Structural and mechanistic basis for the high activity of Fe-N-C catalysts toward oxygen reduction. Energy & Environmental Science 2016, 9 (7), 2418-2432.

45. J., Qingying; Ramaswamy, N.; Hafiz, H.; Tylus, U.; Strickland, K.; Wu, G.; Barbiellini, B.; Bansil, A.; Holby, E. F.; Zelenay, P.; Mukerjee, S., Experimental Observation of Redox-Induced Fe–N Switching Behavior as a Determinant Role for Oxygen Reduction Activity. ACS Nano 2015, 9 (12), 12496-12505.

46. K., Ulrike I.; Lefèvre, M.; Larouche, N.; Schmeisser, D.; Dodelet, J.-P., Correlations between Mass Activity and Physicochemical Properties of Fe/N/C Catalysts for the ORR in PEM Fuel Cell via 57Fe Mössbauer Spectroscopy and Other Techniques. Journal of the American Chemical Society 2014, 136 (3), 978-985.

47. Y., Wenxiu; Liu, X.; Yue, X.; Jia, J.; Guo, S., Bamboo-like Carbon Nanotube/Fe3C Nanoparticle Hybrids and Their Highly Efficient Catalysis for Oxygen Reduction. Journal of the American Chemical Society 2015, 137 (4), 1436-1439.

48. H. Y.; Oluf, J. J.; Wei, Z.; N., C. L.; Wei, X.; J., B. N.; Qingfeng, L., Hollow Spheres of Iron Carbide Nanoparticles Encased in Graphitic Layers as Oxygen Reduction Catalysts. Angewandte Chemie International Edition 2014, 53 (14), 3675-3679.

49. S., Kara; Miner, E.; Jia, Q.; Tylus, U.; Ramaswamy, N.; Liang, W.; Sougrati, M.-T.; Jaouen, F.; Mukerjee, S., Highly active oxygen reduction non-platinum group metal electrocatalyst without direct metal–nitrogen coordination. Nature Communications 2015, 6, 7343.

50. D. D.; Liang, Y.; Xiaoqi, C.; Guoxiong, W.; Li, J.; Xiulian, P.; Jiao, D.; Gongquan, S.; Xinhe, B., Iron Encapsulated within Pod-like Carbon Nanotubes for Oxygen Reduction Reaction. Angewandte Chemie International Edition 2013, 52 (1), 371-375.

51. C., Hoon T.; Won, J. H.; Zelenay, P., Active and stable carbon nanotube/nanoparticle composite electrocatalyst for oxygen reduction. Nature Communications 2013, 4, 1922.

52. G., Donghui; Shibuya, R.; Akiba, C.; Saji, S.; Kondo, T.; Nakamura, J., Active sites of nitrogen-doped carbon materials for oxygen reduction reaction clarified using model catalysts. Science 2016, 351 (6271), 361-365.

53. K., Masaki; Niwa, H.; Saito, M.; Harada, Y.; Oshima, M.; Ofuchi, H.; Terakura, K.; Ikeda, T.; Koshigoe, Y.; Ozaki, J.-i.; Miyata, S., Indirect contribution of transition metal towards oxygen reduction reaction activity in iron phthalocyanine-based carbon catalysts for polymer electrolyte fuel cells. Electrochimica Acta 2012, 74, 254-259.

54. O., Hyung-Suk; Kim, H., The role of transition metals in non-precious nitrogen-modified carbon-based electrocatalysts for oxygen reduction reaction. Journal of Power Sources 2012, 212, 220-225.

55. L., Yanguang; Zhou, W.; Wang, H.; Xie, L.; Liang, Y.; Wei, F.; Idrobo, J.-C.; Pennycook, S. J.; Dai, H., An oxygen reduction electrocatalyst based on carbon nanotube–graphene complexes. Nature Nanotechnology 2012, 7, 394.

56. J., Wen-Jie; Gu, L.; Li, L.; Zhang, Y.; Zhang, X.; Zhang, L.-J.; Wang, J.-Q.; Hu, J.-S.; Wei, Z.; Wan, L.-J., Understanding the High Activity of Fe–N–C Electrocatalysts in Oxygen Reduction: Fe/Fe_3C Nanoparticles Boost the Activity of Fe–N_x. Journal of the American Chemical Society 2016, 138 (10), 3570-3578.

57. L. J.; Feng, Z. R.; Min, C. X.; Hong, T. Y.; Zhang, Q. S., Fe–N Decorated Hybrids of CNTs Grown on Hierarchically Porous Carbon for High-Performance Oxygen Reduction. Advanced Materials 2014, 26 (35), 6074-6079.

58. L. Z.; Fei, S.; Lin, G.; Gen, C.; Tongtong, S.; Jing, L.; Zaiyuan, L.; Xianyang, L.; Bin, W. H.; Yunfeng, L., Post Iron Decoration of Mesoporous Nitrogen-Doped Carbon Spheres for Efficient Electrochemical Oxygen Reduction. Advanced Energy Materials 2017, 7 (22), 1701154.

59. Z. M.; Chunzhen, Y.; Kwong-Yu, C., Structuring Porous Iron-Nitrogen-Doped Carbon in a Core/Shell Geometry for the Oxygen Reduction Reaction. Advanced Energy Materials 2014, 4

(18), 1400840.

60. S. A.; Kateryna, A.; Plamen, A., Fe-N-C Oxygen Reduction Fuel Cell Catalyst Derived from Carbendazim: Synthesis, Structure, and Reactivity. Advanced Energy Materials 2014, 4 (10), 1301735.

61. W., Qiang; Zhou, Z.-Y.; Lai, Y.-J.; You, Y.; Liu, J.-G.; Wu, X.-L.; Terefe, E.; Chen, C.; Song, L.; Rauf, M.; Tian, N.; Sun, S.-G., Phenylenediamine-Based FeNx/C Catalyst with High Activity for Oxygen Reduction in Acid Medium and Its Active-Site Probing. Journal of the American Chemical Society 2014, 136 (31), 10882-10885.

62. K., Ulrike I.; Herranz, J.; Larouche, N.; Arruda, T. M.; Lefevre, M.; Jaouen, F.; Bogdanoff, P.; Fiechter, S.; Abs-Wurmbach, I.; Mukerjee, S.; Dodelet, J.-P., Structure of the catalytic sites in Fe/N/C-catalysts for O2-reduction in PEM fuel cells. Physical Chemistry Chemical Physics 2012, 14 (33), 11673-11688.

63. Z., Andrea; Goellner, V.; Armel, V.; Sougrati, M.-T.; Mineva, T.; Stievano, L.; Fonda, E.; Jaouen, F., Identification of catalytic sites for oxygen reduction in iron- and nitrogen-doped graphene materials. Nat Mater 2015, 14 (9), 937-942.

64. S., Mengxia; Ruan, C.; Chen, Y.; Jiang, C.; Ai, K.; Lu, L., Covalent Entrapment of Cobalt–Iron Sulfides in N-Doped Mesoporous Carbon: Extraordinary Bifunctional Electrocatalysts for Oxygen Reduction and Evolution Reactions. ACS Applied Materials & Interfaces 2015, 7 (2),

1207-1218.

65. M. S.; A., G. G.; V., C. A.; Di-Jia, L., Cobalt Imidazolate Framework as Precursor for Oxygen Reduction Reaction Electrocatalysts. Chemistry – A European Journal 2011, 17 (7), 2063-2067.

66. S., Jiang-Lan; Karan, N. K.; Balasubramanian, M.; Li, S.-Y.; Liu, D.-J., Fe/N/C Composite in Li–O_2 Battery: Studies of Catalytic Structure and Activity toward Oxygen Evolution Reaction. Journal of the American Chemical Society 2012, 134 (40), 16654-16661.

67. Z. Y.; Bingsen, Z.; Xin, L.; Da-Wei, W.; Sheng, S. D., Unravelling the Structure of Electrocatalytically Active Fe–N Complexes in Carbon for the Oxygen Reduction Reaction. Angewandte Chemie International Edition 2014, 53 (40), 10673-10677.

68. C.-V., Federico; Martinez, J. I.; Rossmeisl, J., Density functional studies of functionalized graphitic materials with late transition metals for oxygen reduction reactions. Physical Chemistry Chemical Physics 2011, 13 (34), 15639-15643.

69. R., Nagappan; Tylus, U.; Jia, Q.; Mukerjee, S., Activity Descriptor Identification for Oxygen Reduction on Nonprecious Electrocatalysts: Linking Surface Science to Coordination Chemistry. Journal of the American Chemical Society 2013, 135 (41), 15443-15449.

70. S., Young Jin; Seo, D.-J.; Woo, J.; Lim, J. T.; Cheon, J. Y.; Yang, S. Y.; Lee, J. M.; Kang, D.; Shin, T. J.; Shin, H. S.; Jeong, H. Y.; Kim, C. S.; Kim, M. G.; Kim, T.-Y.; Joo, S. H., A General Approach to Preferential Formation of Active Fe–Nx Sites in Fe–N/C Electrocatalysts for

Efficient Oxygen Reduction Reaction. Journal of the American Chemical Society 2016, 138 (45), 15046-15056.

71. C. Y.; Shufang, J.; Yanggang, W.; Juncai, D.; Wenxing, C.; Zhi, L.; Rongan, S.; Lirong, Z.; Zhongbin, Z.; Dingsheng, W.; Yadong, L., Isolated Single Iron Atoms Anchored on N-Doped Porous Carbon as an Efficient Electrocatalyst for the Oxygen Reduction Reaction. Angewandte Chemie International Edition 2017, 56 (24), 6937-6941.

72. F., Xiujun; Peng, Z.; Ye, R.; Zhou, H.; Guo, X., M3C (M: Fe, Co, Ni) Nanocrystals Encased in Graphene Nanoribbons: An Active and Stable Bifunctional Electrocatalyst for Oxygen Reduction and Hydrogen Evolution Reactions. ACS Nano 2015, 9 (7), 7407-7418.

73. M. J.; Wei, X.; Ilya, S.; Anqi, Z.; Zhenyu, S.; Stefanie, G.; Philipp, W.; Martin, M.; Wolfgang, S., Mn_xO_y/NC and Co_xO_y/NC Nanoparticles Embedded in a Nitrogen-Doped Carbon Matrix for High-Performance Bifunctional Oxygen Electrodes. Angewandte Chemie International Edition 2014, 53 (32), 8508-8512.

74. L. L.; Xianfeng, Y.; Na, M.; Haitao, L.; Yanzhi, X.; Chengmeng, C.; Dongjiang, Y.; Xiangdong, Y., Scalable and Cost-Effective Synthesis of Highly Efficient Fe2N-Based Oxygen Reduction Catalyst Derived from Seaweed Biomass. Small 2016, 12 (10), 1295-1301.

75. W., Lei; Yin, J.; Zhao, L.; Tian, C.; Yu, P.; Wang, J.; Fu, H., Ion-exchanged route synthesis of Fe_2N-N-doped graphitic nanocarbons composite as advanced oxygen reduction electrocatalyst.

Chemical Communications 2013, 49 (29), 3022-3024.

76. Z., Yun; Jiang, W.-J.; Guo, L.; Zhang, X.; Hu, J.-S.; Wei, Z.; Wan, L.-J., Confining Iron Carbide Nanocrystals inside CNx@CNT toward an Efficient Electrocatalyst for Oxygen Reduction Reaction. ACS Applied Materials & Interfaces 2015, 7 (21), 11508-11515.

77. R.-M., Julio A.; Terrones, M.; Terrones, H.; Kroto, H. W.; Sun, L.; Banhart, F., In situ nucleation of carbon nanotubes by the injection of carbon atoms into metal particles. Nature Nanotechnology 2007, 2, 307.

78. D., Jiao; Yu, L.; Deng, D.; Chen, X.; Yang, F.; Bao, X., Highly active reduction of oxygen on a FeCo alloy catalyst encapsulated in pod-like carbon nanotubes with fewer walls. Journal of Materials Chemistry A 2013, 1 (47), 14868-14873.

79. Z., Yipeng; Zhang, H.; Zhang, X.; Liu, R.; Liu, S.; Wang, G.; Zhang, Y.; Zhao, H., Fe/Fe_2O_3 nanoparticles anchored on Fe-N-doped carbon nanosheets as bifunctional oxygen electrocatalysts for rechargeable zinc-air batteries. Nano Research 2016, 9 (7), 2123-2137.

80. L., Katie H.; Kim, H., Nitrogen-doped carbon catalysts derived from ionic liquids in the presence of transition metals for the oxygen reduction reaction. Applied Catalysis B: Environmental 2014, 158-159, 355-360.

81. N., Yao; Li, L.; Wei, Z., Recent advancements in Pt and Pt-free catalysts for oxygen reduction reaction. Chemical Society Reviews 2015, 44 (8), 2168-2201.

82. L., Gang; Li, X.; Ganesan, P.; Popov, B. N., Studies of oxygen reduction reaction active sites and stability of nitrogen-modified carbon composite catalysts for PEM fuel cells. Electrochimica Acta 2010, 55 (8), 2853-2858.

83. M., Paul H.; Wang, E.; Millet, J.-M. M.; Ozkan, U. S., Characterization of the Iron Phase in CNx-Based Oxygen Reduction Reaction Catalysts. The Journal of Physical Chemistry C 2007, 111 (3), 1444-1450.

84. M., Stephen; Stevenson, K. J., Direct Preparation of Carbon Nanofiber Electrodes via Pyrolysis of Iron(II) Phthalocyanine: Electrocatalytic Aspects for Oxygen Reduction. The Journal of Physical Chemistry B 2004, 108 (31), 11375-11383.

85. M., Stephen; Stevenson, K. J., Influence of Nitrogen Doping on Oxygen Reduction Electrocatalysis at Carbon Nanofiber Electrodes. The Journal of Physical Chemistry B 2005, 109 (10), 4707-4716.

86. M., Paul H.; Zhang, L.; Ozkan, U. S., The role of nanostructure in nitrogen-containing carbon catalysts for the oxygen reduction reaction. Journal of Catalysis 2006, 239 (1), 83-96.

87. G., Kuanping; Du, F.; Xia, Z.; Durstock, M.; Dai, L., Nitrogen-Doped Carbon Nanotube Arrays with High Electrocatalytic Activity for Oxygen Reduction. Science 2009, 323 (5915), 760-764.

88. S., Wissam A., Oxygen Reduction Electrocatalysis Using N-Doped Graphene Quantum-Dots.

The Journal of Physical Chemistry Letters 2013, 4 (23), 4160-4165.

89. D., Liming; Xue, Y.; Qu, L.; Choi, H.-J.; Baek, J.-B., Metal-Free Catalysts for Oxygen Reduction Reaction. Chemical Reviews 2015, 115 (11), 4823-4892.

90. L., Linfei; Potts, J. R.; Zhan, D.; Wang, L.; Poh, C. K.; Tang, C.; Gong, H.; Shen, Z.; Lin, J.; Ruoff, R. S., Exploration of the active center structure of nitrogen-doped graphene-based catalysts for oxygen reduction reaction. Energy & Environmental Science 2012, 5 (7), 7936-7942.

91. H. W.; Chunhuan, J.; Jiabo, W.; Lehui, L., High-Rate Oxygen Electroreduction over Graphitic-N Species Exposed on 3D Hierarchically Porous Nitrogen-Doped Carbons. Angewandte Chemie International Edition 2014, 53 (36), 9503-9507.

92. W. L.; Adriano, A.; Martin, P., "Metal-Free" Catalytic Oxygen Reduction Reaction on Heteroatom-Doped Graphene is Caused by Trace Metal Impurities. Angewandte Chemie International Edition 2013, 52 (51), 13818-13821.

93. J., Frederic; Proietti, E.; Lefevre, M.; Chenitz, R.; Dodelet, J.-P.; Wu, G.; Chung, H. T.; Johnston, C. M.; Zelenay, P., Recent advances in non-precious metal catalysis for oxygen-reduction reaction in polymer electrolyte fuel cells. Energy & Environmental Science 2011, 4 (1), 114-130.

94. L., Hai-Wei; Wei, W.; Wu, Z.-S.; Feng, X.; Müllen, K., Mesoporous Metal–Nitrogen-Doped

Carbon Electrocatalysts for Highly Efficient Oxygen Reduction Reaction. Journal of the American Chemical Society 2013, 135 (43), 16002-16005.

95. H., Ismail; Bourgeteau, T.; Cornut, R.; Morozan, A.; Filoramo, A.; Leroy, J.; Derycke, V.; Jousselme, B.; Campidelli, S., Carbon Nanotube-Templated Synthesis of Covalent Porphyrin Network for Oxygen Reduction Reaction. Journal of the American Chemical Society 2014, 136 (17), 6348-6354.

96. J., Yuanyuan; Lu, Y.; Lv, X.; Han, D.; Zhang, Q.; Niu, L.; Chen, W., Enhanced Catalytic Performance of Pt-Free Iron Phthalocyanine by Graphene Support for Efficient Oxygen Reduction Reaction. ACS Cat. 2013, 3 (6), 1263-1271.

97. T. H.; Huajie, Y.; Jiangyan, W.; Nailiang, Y.; Dan, W.; Zhiyong, T., Molecular Architecture of Cobalt Porphyrin Multilayers on Reduced Graphene Oxide Sheets for High-Performance Oxygen Reduction Reaction. Angewandte Chemie International Edition 2013, 52 (21), 5585-5589.

98. C., Ruiguo; Thapa, R.; Kim, H.; Xu, X.; Gyu Kim, M.; Li, Q.; Park, N.; Liu, M.; Cho, J., Promotion of oxygen reduction by a bio-inspired tethered iron phthalocyanine carbon nanotube-based catalyst. Nature Communications 2013, 4, 2076.

99. W. P. J.; Guo-Qiang, Y.; Yoshinori, N.; Jin-Gang, L., Covalent Grafting of Carbon Nanotubes with a Biomimetic Heme Model Compound To Enhance Oxygen Reduction Reactions.

Angewandte Chemie International Edition 2014, 53 (26), 6659-6663.

100. C., Jae Yeong; Kim, T.; Choi, Y.; Jeong, H. Y.; Kim, M. G.; Sa, Y. J.; Kim, J.; Lee, Z.; Yang, T.-H.; Kwon, K.; Terasaki, O.; Park, G.-G.; Adzic, R. R.; Joo, S. H., Ordered mesoporous porphyrinic carbons with very high electrocatalytic activity for the oxygen reduction reaction. Scientific Reports 2013, 3, 2715.

101. L. Q.; Xianhui, B.; Aiguo, K.; Chengyu, M.; Fei, B.; Pingyun, F., Heterometal-Embedded Organic Conjugate Frameworks from Alternating Monomeric Iron and Cobalt Metalloporphyrins and Their Application in Design of Porous Carbon Catalysts. Advanced Materials 2015, 27 (22), 3431-3436.

102. L. N.; Atif, M.; Monica, K.; T., M. D.; Zeev, G.; Lior, E., Metallocorroles as Nonprecious-Metal Catalysts for Oxygen Reduction. Angewandte Chemie International Edition 2015, 54 (47), 14080-14084.

103. G. S.; Doti, S.; Christian, P.; Michael, H.; Fabrice, T.; Alan, L. G., Electrocatalytic O2 Reduction at a Bio-inspired Mononuclear Copper Phenolato Complex Immobilized on a Carbon Nanotube Electrode. Angewandte Chemie International Edition 2016, 55 (7), 2517-2520.

104. C., Zhongwei; Higgins, D.; Yu, A.; Zhang, L.; Zhang, J., A review on non-precious metal electrocatalysts for PEM fuel cells. Energy & Environmental Science 2011, 4 (9), 3167-3192.

105. W. Z. S.; Long, C.; Junzhi, L.; Khaled, P.; Haiwei, L.; Jie, S.; Hermann, S.; Robert, G.;

Xinliang, F.; Klaus, M., High-Performance Electrocatalysts for Oxygen Reduction Derived from Cobalt Porphyrin-Based Conjugated Mesoporous Polymers. Advanced Materials 2014, 26 (9), 1450-1455.

106. C. J. Y.; Kyoungho, K.; Jin, S. Y.; Hye, S. S.; Yugyeong, H.; Jinwoo, W.; Sung-Dae, Y.; Young, J. H.; Youngsik, K.; Hoon, J. S., Graphitic Nanoshell/Mesoporous Carbon Nanohybrids as Highly Efficient and Stable Bifunctional Oxygen Electrocatalysts for Rechargeable Aqueous Na–Air Batteries. Advanced Energy Materials 2016, 6 (7), 1501794.

107. X. Z.; Yuhua, X.; Dapeng, C.; Ling, H.; Jian-Feng, C.; Liming, D., Highly Efficient Electrocatalysts for Oxygen Reduction Based on 2D Covalent Organic Polymers Complexed with Non-precious Metals. Angewandte Chemie International Edition 2014, 53 (9), 2433-2437.

108. C., Ja-Yeon; Hsu, R. S.; Chen, Z., Highly Active Porous Carbon-Supported Nonprecious Metal−N Electrocatalyst for Oxygen Reduction Reaction in PEM Fuel Cells. The Journal of Physical Chemistry C 2010, 114 (17), 8048-8053.

109. L. J. S.; Su, P. G.; Tai, K. S.; Meilin, L.; Jaephil, C., A Highly Efficient Electrocatalyst for the Oxygen Reduction Reaction: N-Doped Ketjenblack Incorporated into Fe/Fe_3C-Functionalized Melamine Foam. Angewandte Chemie 2013, 125 (3), 1060-1064.

110. W. Z.; Suqin, C.; Fei, Z.; Xinliang, F.; Shumao, C.; Shun, M.; Shenglian, L.; Zhen, H.; Junhong, C., Nitrogen-Enriched Core-Shell Structured Fe/Fe_3C-C Nanorods as Advanced

Electrocatalysts for Oxygen Reduction Reaction. Advanced Materials 2012, 24 (11), 1399-1404.

111. W. Z.; Suqin, C.; Yang, H.; Junhong, C., Facile One-Pot, One-Step Synthesis of a Carbon Nanoarchitecture for an Advanced Multifunctonal Electrocatalyst. Angewandte Chemie International Edition 2014, 53 (25), 6496-6500.

112. A. K.; Yanlan, L.; Changping, R.; Lehui, L.; Gaoqing, L., Sp_2 C-Dominant N-Doped Carbon Sub-micrometer Spheres with a Tunable Size: A Versatile Platform for Highly Efficient Oxygen-Reduction Catalysts. Advanced Materials 2013, 25 (7), 998-1003.

113. B., Rajesh; Zelenay, P., A class of non-precious metal composite catalysts for fuel cells. Nature 2006, 443, 63.

114. L., Xiaolin; Wang, H.; Robinson, J. T.; Sanchez, H.; Diankov, G.; Dai, H., Simultaneous Nitrogen Doping and Reduction of Graphene Oxide. Journal of the American Chemical Society 2009, 131 (43), 15939-15944.

115. H., Wenhui; Wang, Y.; Jiang, C.; Lu, L., Structural effects of a carbon matrix in non-precious metal O_2-reduction electrocatalysts. Chemical Society Reviews 2016, 45 (9), 2396-2409.

116. L., Hai-Wei; Zhuang, X.; Brüller, S.; Feng, X.; Müllen, K., Hierarchically porous carbons with optimized nitrogen doping as highly active electrocatalysts for oxygen reduction. Nature Communications 2014, 5, 4973.

117. I., Takashi; Boero, M.; Huang, S.-F.; Terakura, K.; Oshima, M.; Ozaki, J.-i., Carbon Alloy Catalysts: Active Sites for Oxygen Reduction Reaction. The Journal of Physical Chemistry C 2008, 112 (38), 14706-14709.

118. L. R.; Dongqing, W.; Xinliang, F.; Klaus, M., Nitrogen-Doped Ordered Mesoporous Graphitic Arrays with High Electrocatalytic Activity for Oxygen Reduction. Angewandte Chemie International Edition 2010, 49 (14), 2565-2569.

119. S., Reyimjan A.; Anderson, A. B.; Subramanian, N. P.; Kumaraguru, S. P.; Popov, B. N., O_2 Reduction on Graphite and Nitrogen-Doped Graphite: Experiment and Theory. The Journal of Physical Chemistry B 2006, 110 (4), 1787-1793.

120. M., Hui; Larouche, N.; Lefèvre, M.; Jaouen, F.; Stansfield, B.; Dodelet, J.-P., Iron porphyrin-based cathode catalysts for polymer electrolyte membrane fuel cells: Effect of NH3 and Ar mixtures as pyrolysis gases on catalytic activity and stability. Electrochimica Acta 2010, 55 (22), 6450-6461.

121. Z., Gaixia; Chenitz, R.; Lefèvre, M.; Sun, S.; Dodelet, J.-P., Is iron involved in the lack of stability of Fe/N/C electrocatalysts used to reduce oxygen at the cathode of PEM fuel cells? Nano Energy 2016, 29, 111-125.

122. Z., Shenlong; Yin, H.; Du, L.; He, L.; Zhao, K.; Chang, L.; Yin, G.; Zhao, H.; Liu, S.; Tang, Z., Carbonized Nanoscale Metal–Organic Frameworks as High Performance Electrocatalyst for

Oxygen Reduction Reaction. ACS Nano 2014, 8 (12), 12660-12668.

123. Z., Dan; Shui, J.-L.; Chen, C.; Chen, X.; Reprogle, B. M.; Wang, D.; Liu, D.-J., Iron imidazolate framework as precursor for electrocatalysts in polymer electrolyte membrane fuel cells. Chemical Science 2012, 3 (11), 3200-3205.

124. H. Y.; Zhenhai, W.; Shumao, C.; Suqin, C.; Shun, M.; Junhong, C., An Advanced Nitrogen-Doped Graphene/Cobalt-Embedded Porous Carbon Polyhedron Hybrid for Efficient Catalysis of Oxygen Reduction and Water Splitting. Advanced Functional Materials 2015, 25 (6), 872-882.

125. H. Y.; Taizhong, H.; Zhenhai, W.; Shun, M.; Shumao, C.; Junhong, C., Metal−Organic Framework-Derived Nitrogen-Doped Core-Shell-Structured Porous Fe/Fe_3C@C Nanoboxes Supported on Graphene Sheets for Efficient Oxygen Reduction Reactions. Advanced Energy Materials 2014, 4 (11), 1400337.

126. Z. M.; Yiling, L.; Feipeng, Z.; Kaiqi, N.; Na, H.; Xinxia, W.; Wenjing, H.; Xuening, S.; Jun, Z.; Yanguang, L., Metallic Cobalt Nanoparticles Encapsulated in Nitrogen-Enriched Graphene Shells: Its Bifunctional Electrocatalysis and Application in Zinc–Air Batteries. Advanced Functional Materials 2016, 26 (24), 4397-4404.

127. N., Wenhan; Li, L.; Liu, X.; Wang, N.; Liu, J.; Zhou, W.; Tang, Z.; Chen, S., Mesoporous N-Doped Carbons Prepared with Thermally Removable Nanoparticle Templates: An Efficient

Electrocatalyst for Oxygen Reduction Reaction. Journal of the American Chemical Society 2015, 137 (16), 5555-5562.

128. C. S.; Jiyu, B.; Yu, Z.; Lijun, Y.; Chen, Z.; Yanwen, M.; Qiang, W.; Xizhang, W.; Zheng, H., Nitrogen-Doped Carbon Nanocages as Efficient Metal-Free Electrocatalysts for Oxygen Reduction Reaction. Advanced Materials 2012, 24 (41), 5593-5597.

129. L., Hai-Wei; Wu, Z.-Y.; Chen, L.-F.; Li, C.; Yu, S.-H., Bacterial cellulose derived nitrogen-doped carbon nanofiber aerogel: An efficient metal-free oxygen reduction electrocatalyst for zinc-air battery. Nano Energy 2015, 11, 366-376.

130. M., Na; Jia, Y.; Yang, X.; She, X.; Zhang, L.; Peng, Z.; Yao, X.; Yang, D., Seaweed biomass derived (Ni,Co)/CNT nanoaerogels: efficient bifunctional electrocatalysts for oxygen evolution and reduction reactions. Journal of Materials Chemistry A 2016, 4 (17), 6376-6384.

131. C. X.; Shubin, Y.; Xingxu, Y.; Jiugou, L.; Shuang, S.; M., A. P.; Zhengjun, Z., Pyridinic-Nitrogen-Dominated Graphene Aerogels with Fe–N–C Coordination for Highly Efficient Oxygen Reduction Reaction. Advanced Functional Materials 2016, 26 (31), 5708-5717.

132. Y., Gang; Choi, W.; Pu, X.; Yu, C., Scalable synthesis of bi-functional high-performance carbon nanotube sponge catalysts and electrodes with optimum C-N-Fe coordination for oxygen reduction reaction. Energy & Environmental Science 2015, 8 (6), 1799-1807.

133. F., Ju; Liang, Y.; Wang, H.; Li, Y.; Zhang, B.; Zhou, J.; Wang, J.; Regier, T.; Dai, H.,

Engineering manganese oxide/nanocarbon hybrid materials for oxygen reduction electrocatalysis. Nano Research 2012, 5 (10), 718-725.

134. L., Yongye; Li, Y.; Wang, H.; Zhou, J.; Wang, J.; Regier, T.; Dai, H., Co3O4 nanocrystals on graphene as a synergistic catalyst for oxygen reduction reaction. Nature Materials 2011, 10, 780.

135. S., Jin; Gasteiger, H. A.; Yabuuchi, N.; Nakanishi, H.; Goodenough, J. B.; Shao-Horn, Y., Design principles for oxygen-reduction activity on perovskite oxide catalysts for fuel cells and metal–air batteries. Nature Chemistry 2011, 3, 546.

136. K., Jin Yong; Oh, T.-K.; Shin, Y.; Bonnett, J.; Weil, K. S., A novel non-platinum group electrocatalyst for PEM fuel cell application. International Journal of Hydrogen Energy 2011, 36 (7), 4557-4564.

137. Z., Lipeng; Xia, Z., Mechanisms of Oxygen Reduction Reaction on Nitrogen-Doped Graphene for Fuel Cells. The Journal of Physical Chemistry C 2011, 115 (22), 11170-11176.

138. A., Jun-ichi, Reduced HOMO−LUMO Gap as an Index of Kinetic Stability for Polycyclic Aromatic Hydrocarbons. The Journal of Physical Chemistry A 1999, 103 (37), 7487-7495.

139. C., Zhu; Higgins, D.; Tao, H.; Hsu, R. S.; Chen, Z., Highly Active Nitrogen-Doped Carbon Nanotubes for Oxygen Reduction Reaction in Fuel Cell Applications. The Journal of Physical Chemistry C 2009, 113 (49), 21008-21013.

140. W. S.; Eswaramoorthi, I.; Ajit, R.; Yuhua, X.; Dingshan, Y.; Liming, D., Vertically Aligned BCN Nanotubes as Efficient Metal-Free Electrocatalysts for the Oxygen Reduction Reaction: A Synergetic Effect by Co-Doping with Boron and Nitrogen. Angewandte Chemie International Edition 2011, 50 (49), 11756-11760.

141. W. S.; Lipeng, Z.; Zhenhai, X.; Ajit, R.; Wook, C. D.; Jong-Beom, B.; Liming, D., BCN Graphene as Efficient Metal-Free Electrocatalyst for the Oxygen Reduction Reaction. Angewandte Chemie International Edition 2012, 51 (17), 4209-4212.

142. J., Raymond, A New Fuel Cell Cathode Catalyst. Nature 1964, 201, 1212.

143. Z., Jintao; Zhao, Z.; Xia, Z.; Dai, L., A metal-free bifunctional electrocatalyst for oxygen reduction and oxygen evolution reactions. Nature Nanotechnology 2015, 10, 444.

144. D., Mark K., Electrocatalyst approaches and challenges for automotive fuel cells. Nature 2012, 486, 43.

145. D., Youzhen; Li, J., Tungsten nitride nanocrystals on nitrogen-doped carbon black as efficient electrocatalysts for oxygen reduction reactions. Chemical Communications 2015, 51 (3), 572-575.

146. J., Yan; Zheng, Y.; Jaroniec, M.; Qiao, S. Z., Origin of the Electrocatalytic Oxygen Reduction Activity of Graphene-Based Catalysts: A Roadmap to Achieve the Best Performance. Journal of the American Chemical Society 2014, 136 (11), 4394-4403.

147. K., Bae Jung; Lee, D. U.; Wu, J.; Higgins, D.; Yu, A.; Chen, Z., Iron- and Nitrogen-Functionalized Graphene Nanosheet and Nanoshell Composites as a Highly Active Electrocatalyst for Oxygen Reduction Reaction. The Journal of Physical Chemistry C 2013, 117 (50), 26501-26508.

148. W. Z. Y.; Xing-Xing, X.; Bi-Cheng, H.; Hai-Wei, L.; Yue, L.; Li-Feng, C.; Shu-Hong, Y., Iron Carbide Nanoparticles Encapsulated in Mesoporous Fe-N-Doped Carbon Nanofibers for Efficient Electrocatalysis. Angewandte Chemie International Edition 2015, 54 (28), 8179-8183.

149. C. M. G.; Dennis, S.; F., L. S.; M., S. T.; Mircea, D., Cu3(hexaiminotriphenylene)2: An Electrically Conductive 2D Metal–Organic Framework for Chemiresistive Sensing. Angewandte Chemie International Edition 2015, 54 (14), 4349-4352.

150. K., Ulrike I.; Herrmann-Geppert, I.; Behrends, J.; Lips, K.; Fiechter, S.; Bogdanoff, P., On an Easy Way To Prepare Metal–Nitrogen Doped Carbon with Exclusive Presence of MeN4-type Sites Active for the ORR. Journal of the American Chemical Society 2016, 138 (2), 635-640.

151. Z., Wei; Lai, W.; Cao, R., Energy-Related Small Molecule Activation Reactions: Oxygen Reduction and Hydrogen and Oxygen Evolution Reactions Catalyzed by Porphyrin- and Corrole-Based Systems. Chemical Reviews 2017, 117 (4), 3717-3797.

152. H., Juan; Jaouen, F.; Lefèvre, M.; Kramm, U. I.; Proietti, E.; Dodelet, J.-P.; Bogdanoff, P.;

Fiechter, S.; Abs-Wurmbach, I.; Bertrand, P.; Arruda, T. M.; Mukerjee, S., Unveiling N-Protonation and Anion-Binding Effects on Fe/N/C Catalysts for O_2 Reduction in Proton-Exchange-Membrane Fuel Cells. The Journal of Physical Chemistry C 2011, 115 (32), 16087-16097.

153. K., Ulrike I.; Herrmann-Geppert, I.; Bogdanoff, P.; Fiechter, S., Effect of an Ammonia Treatment on Structure, Composition, and Oxygen Reduction Reaction Activity of Fe–N–C Catalysts. The Journal of Physical Chemistry C 2011, 115 (47), 23417-23427.

154. S., Fei; Wu, H.; Liu, X.; Liu, F.; Zhou, H.; Gao, J.; Lu, Y., Nitrogen-rich carbon spheres made by a continuous spraying process for high-performance supercapacitors. Nano Research 2016, 9 (11), 3209-3221.

155. J., Xiangling; Hu, Q.; Hampsey, J. E.; Qiu, X.; Gao, L.; He, J.; Lu, Y., Synthesis and Characterization of Functionalized Mesoporous Silica by Aerosol-Assisted Self-Assembly. Chemistry of Materials 2006, 18 (9), 2265-2274.

156. Y., Hideto; Takeda, S.; Uchiyama, T.; Kohno, H.; Homma, Y., Atomic-Scale In-situ Observation of Carbon Nanotube Growth from Solid State Iron Carbide Nanoparticles. Nano Letters 2008, 8 (7), 2082-2086.

157. K., Ulrike; Herrmann, I.; Bogdanoff, P.; Barkschat, C.; Fiechter, S.; Iwata, N.; Takahashi, H.; Nishikori, H., Evaluation and Analysis of PEM-FC Performance using Non-Platinum

Cathode Catalysts based on Pyrolysed Fe- and Co-Porphyrins - Influence of a Secondary Heat-treatment. ECS Transactions 2008, 13 (17), 125-141.

158. K., Heejin; Lee, K.; Woo, S. I.; Jung, Y., On the mechanism of enhanced oxygen reduction reaction in nitrogen-doped graphene nanoribbons. Physical Chemistry Chemical Physics 2011, 13 (39), 17505-17510.

159. Z., Yong; Watanabe, K.; Hashimoto, K., Self-Supporting Oxygen Reduction Electrocatalysts Made from a Nitrogen-Rich Network Polymer. Journal of the American Chemical Society 2012, 134 (48), 19528-19531.

160. P., U. A.; Schmidt, T.; Gasteiger, H. A.; Behm, R. J., Oxygen reduction on a high-surface area Pt/Vulcan carbon catalyst: A thin-film rotating ring-disk electrode study. 2001; Vol. 495, p 134-145.

161. K., Anusorn; Kuwabata, S.; Girishkumar, G.; Kamat, P., Single-Wall Carbon Nanotubes Supported Platinum Nanoparticles with Improved Electrocatalytic Activity for Oxygen Reduction Reaction. Langmuir 2006, 22 (5), 2392-2396.

162. L., Wei-Peng; Su, C.-H.; Tsao, L.-C.; Chang, C.-T.; Hsu, Y.-P.; Yeh, C.-S., Controllable CO Release Following Near-Infrared Light-Induced Cleavage of Iron Carbonyl Derivatized Prussian Blue Nanoparticles for CO-Assisted Synergistic Treatment. ACS Nano 2016, 10 (12), 11027-11036.

163. H., Shaozheng; Jin, R.; Lu, G.; Liu, D.; Gui, J., The properties and photocatalytic performance comparison of Fe3+-doped g-C3N4 and Fe2O3/g-C3N4 composite catalysts. RSC Advances 2014, 4 (47), 24863-24869.

164. M., Yanjiao; Wang, H.; Key, J.; Linkov, V.; Ji, S.; Mao, X.; Wang, Q.; Wang, R., Ultrafine iron oxide nanoparticles supported on N-doped carbon black as an oxygen reduction reaction catalyst. International Journal of Hydrogen Energy 2014, 39 (27), 14777-14782.

165. W., Haitao; Wang, W.; Xu, Y. Y.; Dong, S.; Xiao, J.; Wang, F.; Liu, H.; Xia, B. Y., Hollow Nitrogen-Doped Carbon Spheres with Fe3O4 Nanoparticles Encapsulated as a Highly Active Oxygen-Reduction Catalyst. ACS Applied Materials & Interfaces 2017, 9 (12), 10610-10617.

166. C., Fangyi; Chen, J., Metal-air batteries: from oxygen reduction electrochemistry to cathode catalysts. Chemical Society Reviews 2012, 41 (6), 2172-2192.

167. C. R.; Jang-Soo, L.; Meilin, L.; Jaephil, C., Recent Progress in Non-Precious Catalysts for Metal-Air Batteries. Advanced Energy Materials 2012, 2 (7), 816-829.

168. S., Minhua; Chang, Q.; Dodelet, J.-P.; Chenitz, R., Recent Advances in Electrocatalysts for Oxygen Reduction Reaction. Chemical Reviews 2016, 116 (6), 3594-3657.

169. Z., Chengzhou; Li, H.; Fu, S.; Du, D.; Lin, Y., Highly efficient nonprecious metal catalysts towards oxygen reduction reaction based on three-dimensional porous carbon nanostructures. Chemical Society Reviews 2016, 45 (3), 517-531.

170. M. T. Y.; Jingrun, R.; Sheng, D.; Mietek, J.; Zhang, Q. S., Phosphorus-Doped Graphitic Carbon Nitrides Grown In Situ on Carbon-Fiber Paper: Flexible and Reversible Oxygen Electrodes. Angewandte Chemie International Edition 2015, 54 (15), 4646-4650.

171. Z., Yu; Yang, L.; Chen, S.; Wang, X.; Ma, Y.; Wu, Q.; Jiang, Y.; Qian, W.; Hu, Z., Can Boron and Nitrogen Co-doping Improve Oxygen Reduction Reaction Activity of Carbon Nanotubes? Journal of the American Chemical Society 2013, 135 (4), 1201-1204.

172. X., Bao Yu; Yan, Y.; Li, N.; Wu, H. B.; Lou, X. W.; Wang, X., A metal–organic framework-derived bifunctional oxygen electrocatalyst. Nature Energy 2016, 1, 15006.

173. L., Ling; Zhu, Q.; Xu, A.-W., Noble-Metal-Free Fe–N/C Catalyst for Highly Efficient Oxygen Reduction Reaction under Both Alkaline and Acidic Conditions. Journal of the American Chemical Society 2014, 136 (31), 11027-11033.

174. P. J.; Yang, X. Y.; Huan, Y.; Zehua, D.; Hongfang, L.; Yu, X. B., Advanced Architectures and Relatives of Air Electrodes in Zn–Air Batteries. Advanced Science 2018, 5 (4), 1700691.

175. W., Gang; Johnston, C. M.; Mack, N. H.; Artyushkova, K.; Ferrandon, M.; Nelson, M.; Lezama-Pacheco, J. S.; Conradson, S. D.; More, K. L.; Myers, D. J.; Zelenay, P., Synthesis-structure-performance correlation for polyaniline-Me-C non-precious metal cathode catalysts for oxygen reduction in fuel cells. Journal of Materials Chemistry 2011, 21 (30), 11392-11405.

176. L. Z.; Guanglan, L.; Luhua, J.; Jinlei, L.; Gongquan, S.; Chungu, X.; Fuwei, L., Ionic

Liquids as Precursors for Efficient Mesoporous Iron-Nitrogen-Doped Oxygen Reduction Electrocatalysts. Angewandte Chemie 2015, 127 (5), 1514-1518.

177. S., Jian-Ke; Xu, Q., Functional materials derived from open framework templates/precursors: synthesis and applications. Energy & Environmental Science 2014, 7 (7), 2071-2100.

178. Z., Lei; Wu, H. B.; Lou, X. W., Metal–Organic-Frameworks-Derived General Formation of Hollow Structures with High Complexity. Journal of the American Chemical Society 2013, 135 (29), 10664-10672.

179. X., Xiaodong; Cao, R.; Jeong, S.; Cho, J., Spindle-like Mesoporous α-Fe2O3 Anode Material Prepared from MOF Template for High-Rate Lithium Batteries. Nano Letters 2012, 12 (9), 4988-4991.

180. H., Han; Han, L.; Yu, M.; Wang, Z.; Lou, X. W., Metal-organic-framework-engaged formation of Co nanoparticle-embedded carbon@Co9S8 double-shelled nanocages for efficient oxygen reduction. Energy & Environmental Science 2016, 9 (1), 107-111.

181. C. W.; L., T. N.; Cuiling, L.; Masataka, I.; Norihiro, S.; Shinsuke, I.; Katsuhiko, A.; Yusuke, Y., Synthesis of Nanoporous Carbon–Cobalt-Oxide Hybrid Electrocatalysts by Thermal Conversion of Metal–Organic Frameworks. Chemistry – A European Journal 2014, 20 (15), 4217-4221.

182. S. L.; Huijun, Y.; Xing, H.; Tong, B.; Run, S.; Yufei, Z.; N., W. G. I.; Li-Zhu, W.; Chen-Ho, T.; Tierui, Z., Well-Dispersed ZIF-Derived Co,N-Co-doped Carbon Nanoframes through Mesoporous-Silica-Protected Calcination as Efficient Oxygen Reduction Electrocatalysts. Advanced Materials 2016, 28 (8), 1668-1674.

183. T. J.; Adina, M.; Tahar, S. M.; Michel, L.; Régis, C.; Jean-Pol, D.; Deborah, J.; Frédéric, J., Optimized Synthesis of Fe/N/C Cathode Catalysts for PEM Fuel Cells: A Matter of Iron–Ligand Coordination Strength. Angewandte Chemie International Edition 2013, 52 (27), 6867-6870.

184. L., Teng; Zhao, P.; Hua, X.; Luo, W.; Chen, S.; Cheng, G., An Fe-N-C hybrid electrocatalyst derived from a bimetal-organic framework for efficient oxygen reduction. Journal of Materials Chemistry A 2016, 4 (29), 11357-11364.

185. W., Xiaojuan; Zhang, H.; Lin, H.; Gupta, S.; Wang, C.; Tao, Z.; Fu, H.; Wang, T.; Zheng, J.; Wu, G.; Li, X., Directly converting Fe-doped metal–organic frameworks into highly active and stable Fe-N-C catalysts for oxygen reduction in acid. Nano Energy 2016, 25, 110-119.

186. C., Janosch; Nayuk, R.; Springer, S.; Feldhoff, A.; Huber, K.; Wiebcke, M., Controlling Zeolitic Imidazolate Framework Nano- and Microcrystal Formation: Insight into Crystal Growth by Time-Resolved In Situ Static Light Scattering. Chemistry of Materials 2011, 23 (8), 2130-2141.

187. Y. Z. K.; Ling, L.; An-Wu, X., 2D Nanoporous Fe−N/C Nanosheets as Highly Efficient

Non-Platinum Electrocatalysts for Oxygen Reduction Reaction in Zn-Air Battery. Small 2016, 12 (41), 5710-5719.

188. W. M.; Sisi, L.; Na, X.; Tao, Q.; Chenglin, Y., Active Fe-Nx Sites in Carbon Nanosheets as Oxygen Reduction Electrocatalyst for Flexible All-Solid-State Zinc–Air Batteries. Advanced Sustainable Systems 2017, 1 (10), 1700085.

189. A., Ganesan; Abbas, S. C.; Lv, J.; Ding, K.; Liu, Q.; Babu, D. D.; Huang, Y.; Xie, J.; Wu, M.; Wang, Y., Highly exposed Fe-N4 active sites in porous poly-iron-phthalocyanine based oxygen reduction electrocatalyst with ultrahigh performance for air cathode. Dalton Transactions 2017, 46 (6), 1803-1810.

190. Z., Jiawei; Zhou, H.; Zhang, C.; Zhang, J.; Mu, S., Dual active nitrogen doped hierarchical porous hollow carbon nanospheres as an oxygen reduction electrocatalyst for zinc-air batteries. Nanoscale 2017, 9 (35), 13257-13263.